Analogue event horizons in dielectric medium

Vyome Singh

A thesis submitted for the degree of PhD
at the
University of St Andrews

2021

Candidate's declaration

I, Vyome Singh, do hereby certify that this thesis, submitted for the degree of PhD, which is approximately 22,000 words in length, has been written by me, and that it is the record of work carried out by me, or principally by myself in collaboration with others as acknowledged, and that it has not been submitted in any previous application for any degree. I confirm that any appendices included in my thesis contain only material permitted by the 'Assessment of Postgraduate Research Students' policy.

I was admitted as a research student at the University of St Andrews in September 2015.

I received funding from an organisation or institution and have acknowledged the funder(s) in the full text of my thesis.

 13/05/2021

Date   Signature of candidate

Supervisor's declaration

I hereby certify that the candidate has fulfilled the conditions of the Resolution and Regulations appropriate for the degree of PhD in the University of St Andrews and that the candidate is qualified to submit this thesis in application for that degree. I confirm that any appendices included in the thesis contain only material permitted by the 'Assessment of Postgraduate Research Students' policy.

Date   Signature of supervisor

Permission for publication

In submitting this thesis to the University of St Andrews we understand that we are giving permission for it to be made available for use in accordance with the regulations of the University Library for the time being in force, subject to any copyright vested in the work not being affected thereby. We also understand, unless exempt by an award of an embargo as requested below, that the title and the abstract will be published, and that a copy of the work may be made and supplied to any bona fide library or research worker, that this thesis will be electronically accessible for personal or research use and that the library has the right to migrate this thesis into new electronic forms as required to ensure continued access to the thesis.

I, Vyome Singh, confirm that my thesis does not contain any third-party material that requires copyright clearance.

The following is an agreed request by candidate and supervisor regarding the publication of this thesis:

Printed copy

No embargo on print copy.

Electronic copy

No embargo on electronic copy.

13/05/2021

Date   Signature of candidate

Date   Signature of supervisor

Underpinning Research Data or Digital Outputs

Candidate's declaration

I, Vyome Singh, understand that by declaring that I have original research data or digital outputs, I should make every effort in meeting the University's and research funders' requirements on the deposit and sharing of research data or research digital outputs.

Date   Signature of candidate

Permission for publication of underpinning research data or digital outputs

We understand that for any original research data or digital outputs which are deposited, we are giving permission for them to be made available for use in accordance with the requirements of the University and research funders, for the time being in force.

We also understand that the title and the description will be published, and that the underpinning research data or digital outputs will be electronically accessible for use in accordance with the license specified at the point of deposit, unless exempt by award of an embargo as requested below.

The following is an agreed request by candidate and supervisor regarding the publication of underpinning research data or digital outputs:

No embargo on underpinning research data or digital outputs.

Date   Signature of candidate

Date   Signature of supervisor

Acknowledgments

Abstract

In this thesis I numerically study an optical pulse travelling in a dielectric medium as an analogue event horizon. A novel numerical method is developed to study the scattering properties of this optical system. Numerical solutions of scattering problems often exhibit instabilities. The staircase approximation, in addition, can cause slow convergence. We present a differential equation for the scattering matrix which solves both of these problems. The new algorithm inherits the numerical stability of the S matrix algorithm and converges faster for a smoothly varying potential than the S matrix algorithm with the staircase approximation. We apply our equation to solve a 1D stationary scattering of plane waves from a non-periodic smoothly varying pulse/scatterer travelling with a constant velocity in a lossless medium. The properties of stability and the convergence of the Riccati matrix equation are demonstrated. Furthermore, we include a relative velocity between the scatterer and the wave medium to generalise the algorithm further where the number of right and left going modes are not equal. The algorithm is applicable for stationary scattering process from arbitrarily shaped smooth scatterers, periodic or non-periodic, even when the scatterer is varying at the scale of wavelengths. This method is used to present numerical results for a sub-femtoseconds optical pulse travelling in bulk silica. We calculate the analogue hawking radiation from the analogue system. The temperature of the hawking radiation is studied systematically with many different profiles of pulses. We find out steepness, intensity and duration of the pulse are most important in producing analogue hawking radiation in these systems. A better numerical and theoretical understanding will make the experiments better suited to detect hawking radiation.

Contents

Chapter 1

Introduction

Black holes have captured people's attention for nearly a century. They are one of the most mysterious objects in the universe, interesting to study from the point of scientific curiosity. The three major branches of physics - general relativity, thermodynamics and quantum mechanics - all become important in the study of black holes. Lack of understanding of black holes also shows the gaps in our knowledge in physics. A complete theory of quantum gravity is still eluding scientists and theorists. Though people are still studying more accessible and testable features of black-holes. Another approach is to study analogous systems to black holes to learn more about the real system in question. This thesis will focus on an optical analogue system that mimics the kinematics of an event horizon of a black hole.

Thesis Layout

The aim of the thesis is to show the reader an in-depth theoretical and numerical study of optical analogue systems in a dielectric medium. These systems are analogous to the event horizon of a black hole and the aim is to learn as much as possible about the analogous systems to draw parallels to the real one. At the same time, the purpose is to have good numerical simulations of the analogue system so that experiments can be done more efficiently and the results can be analysed and compared. We would also like to shed light on a new algorithm to efficiently calculate scattering matrices. Using the algorithm, we have calculated Hawking radiation from various optical pulse setups, which has not been done in such an intensive way before.

The layout for the thesis is as follows: We first introduce in a formal way the concept of a black hole in general relativity. Then we focus on the phenomenon of Hawking radiation. We introduce all the tools we would require to derive Hawking radiation. We follow this with an intensive literature review of the field of analogue systems to study Hawking radiation.

In the second chapter, the theory of our specific system is studied in detail. We study the propagation of electromagnetic fields in bulk silica by using the Hopfield model. We also introduce the concept of a scattering matrix. In the third chapter we study various algorithms to numerically calculate the scattering matrix and the numerical precision problem each algorithm presents. Here we introduce our novel algorithm to bypass these problems to calculate the scattering matrix efficiently. In the fourth chapter we discuss the results and explain several features of the Hawking spectrum in our analogue optical system. This is followed by a brief conclusion summarising all the key findings of the thesis.

Black Holes

The term 'black holes' was coined by John Wheeler, but the idea was first proposed in 1783 by John Mitchell. He wanted to propose a way to find the mass of a star by measuring the 'shift' in emitted light caused by the gravitational pull. He thought of the existence of 'invisible stars', entities so massive that the escape velocity is higher than the speed of light. Mitchell's insight was soon supported using Newton's theory of gravitation by Laplace in 1796 in his book, Exposition du Système du Monde. Though the idea of gravitational force affecting light was new and unexplored, the dynamics of this force on light was not known. Einstein in 1915 invented the general theory of relativity [1] and it opened a whole new regime of physics by linking gravity to the curvature of space-time. In Einstein's picture space and time were not dormant in the background, like in Newtonian mechanics, but played an active role where matter and energy could bend and curve space and time. General relativity does not require force dynamics, as in Newton theory of gravity, but predicts the path of an object by finding the geodesic, extremum paths, on space-time. Soon after in 1916, Karl Schwarzschild, found a particular solution of general relativity [2]. This solution was the key to realising that general relativity allows a region of space to exist from which nothing can escape, not even light. In 1939, Oppenheimer published the first detailed treatment of gravitational collapse with general relativity [3] and it set the platform to work further on the possibility of formation of black holes.

The Schwarzschild solution to Einstein's general relativity is written as [4]

$$(ds)^2 = -(1 - \frac{R_s}{r})c^2 dt_s^2 + \frac{dr^2}{(1 - \frac{R_s}{r})} + r^2 d\Omega^2. \tag{1.1}$$

t_s is the time of a stationary observer at infinity, a bookkeeper's time. $d\Omega^2 = d\Theta^2 + \sin(\Theta)^2 d\Phi^2$ is the angular line element in spherical coordinates. ds is the space-time interval, $ds = 0$ describes the light cone, $(ds)^2 < 0$ describes space-like separated events and $(ds)^2 > 0$ time-like events. For an object falling radially, we can put $d\Omega^2 = 0$ and make the metric simple. R_s is the Schwarzschild radius defined as $R_s = \frac{2GM}{c^2}$. In

Newtonian theory, the Schwarzschild radius is where the escape velocity becomes the speed of light, c. This means that nothing can exit the sphere interior to the Schwarzschild radius. The surface of sphere of radius R_s is called the event horizon. Let us point out the few crucial features of this flat space-time metric. First of all; we see that if $r \to \infty$ the ratio $\frac{R_s}{r} \to 0$ and the metric approaches flat space metric, as expected, $ds^2 = -c^2 dt_s^2 + dr^2$. Second thing to note here is that the metric (1.1) contains two singularities, one when $r = 0$ and another when $r = R_s$. The former is a physical singularity where space-time collapses to a singular point. The relevant physics of quantum gravity applicable here is unknown and beyond the scope of this article. The singularity at $r = R_s$ is of interest to us. To understand this singularity better, let an infinitely distant observer, bookkeeper, observe a light ray falling radially on the event horizon. Thus set $ds = 0$ and $d\Omega = 0$ for a radial light trajectory and we can arrange (1.1) to get

$$\frac{dr}{dt_s} = \pm c \left(1 - \frac{R_s}{r} \right). \tag{1.2}$$

Here we see that as $r \to R_s$ the velocity, as perceived by the bookkeeper, goes to zero. As the light approaches the event horizon from flat space it slows to a standstill! Though it looks like a singularity, it is indeed not a physical one. If we transform the coordinates, then we can avoid the singularity at $r = R_s$. This is what was done by Painleve [5] and Gullstrand [6], independently. The transformation required could be viewed as introducing a new time, τ, such that the temporal slices $\tau = constant$ defines a flat space. τ is defined as

$$\tau = t_s + a(r), \tag{1.3}$$

where $a(r)$ is defined such that the coefficient of dr^2 is one. For that to be true $a(r)$ has to fulfill

$$\frac{da(r)}{dr} = \frac{1}{1 - \frac{R_s}{r}} \sqrt{\frac{R_s}{r}}. \tag{1.4}$$

One could say it differently and name τ as proper time. Both the statements are equivalent. After the transformation, the metric looks like

$$ds^2 = -c^2 d\tau^2 + (dr + c\sqrt{\frac{R_s}{r}} d\tau)^2 + r^2 d\Omega^2. \tag{1.5}$$

This metric provides an insightful and different picture while preserving the physics. It looks like flat space in which space itself is flowing radially towards the event horizon [7]. The speed of space flowing is $c\sqrt{\frac{R_s}{r}}$. We see that as we move away from the horizon, space is stationary, as expected, but as $r \to R_s$ the $speed \to c$. To find the velocity of light on a radial trajectory in this frame we set, like previously, $ds = 0$ and $d\Omega^2 = 0$.

This leads to

$$\frac{dr}{d\tau} = \pm(c \mp c\sqrt{\frac{R_s}{r}}), \qquad (1.6)$$

unlike the velocity in (1.2), where it was hard to grasp light coming to stand still, the above equation provides a more 'natural' picture. As this describes a flat metric light travelling away from or towards the horizon will move with velocity c but as space itself is flowing, the effective velocity will be $\pm$c $\mp$ the flow speed of space itself. Light cannot escape the horizon as the two velocities totally cancel each other. Light just outside the horizon directed away from the black hole may escape. First slowly and then gathering speed as it gets away from the horizon.

Now we can explain the name, black holes. The collapsed star is dense enough that the escape velocity exceeds the speed of light. Light cannot get away from it. Hence, the word 'black'. Anything that fal;s through the horizon cannot escape it. It is because of this lack of information that no one can study the inside of the black hole. Hence, the word 'hole'.

1.1   Hawking Radiation

In 1974, Stephen Hawking predicted that black holes radiate and evaporate away [8]. The source of this radiation is the quantum vacuum scattering off the event horizon. This was a non-intuitive result as black holes are defined such that nothing can escape them. The original derivation of Hawking radiation stands on unphysical assumptions. One of them is that the waves have smaller wavelengths than the Planck scale near the horizon. If you trace an escaping mode back to the horizon, the blue shift accumulated by the wave becomes huge! So big that that the wavelength of the waves becomes smaller than Planck's length. This is called the trans-Planckian problem and the derivation relies on such huge blue shifts. We shall see that one can derive the essentials of Hawking radiation without this premise [9, 10].

The conditions generating Hawking radiation were thought to be a result of extreme gravity and entropy of the black hole but in recent times it has been shown that Hawking-like radiation is possible even without an actual horizon or/and an existence of a black hole. We shall talk about the conditions for generating Hawking-like radiation in more detail later.

In order to understand the origin of Hawking radiation better we have to approach the topic from a quantum field theory perspective. In quantum theory Hawking radiation results from the scattering of quantum vacuum mode in curved space-time.

1.1.1 Quantum field theory

Quantum field theory (QFT) is one of the most successful theories in physics and yet it is the most non-intuitive one. In quantum mechanics we quantize non-relativistic particles to understand their behaviour in the quantum regime. Describing relativistic particles seems to be a bit more tricky, for several reasons. First, when we try to write down the Schrodinger equation in a relativistic invariant form, i.e Klein-Gordon equation or the Dirac equation, we encounter negative-energy states. The number of particles is not conserved in relativistic quantum mechanics. One can understand this by invoking the uncertainty principle $\Delta E \Delta t = \hbar$, according to this relation particles for a very short time can 'pop' into existence and disappear, temporarily violating the law of conservation of energy. We need a multi-particle theory in relativistic quantum mechanics to preserve causality. If we study the amplitude propagation of a free particle we find that for a single particle the amplitude is small but finite outside the light cone. This seems to violate causality but quantum field theory solves this problem in a unique way, propagation of a particle in space-like interval is countered by the propagation of it's antiparticle in the opposite direction. When the two amplitudes are added we see that they cancel each other exactly outside the light cone preserving causality. These are some of the reasons as to why quantizing fields gives a more coherent picture rather than quantizing particles as in non-relativistic quantum mechanics.

1.1.2 From Classical to Quantum

In classical mechanics we have two ways to reach the equation of motion for a particle. The first method is the Newtonian method, forces acting on the particles are taken into account to calculate the path taken by the particle. The second method is called the action principle, here a mathematical object called the action, S, takes into consideration all the paths possible by the particle and the particle takes the path which extremises the action. The path of extreme action is the same path as calculated by Newtonian mechanics. The principle of least action framework is so powerful that it is valid in the quantum mechanical regime as well. In quantum mechanics there is a probability amplitude associated to every path, so there is a finite probability amplitude for the particle to take a path that is not the extremum path. Action is calculated as follows

$$S = \int L dt. \tag{1.7}$$

Here L is the Lagrangian of the system. It is a measure of how quickly the state of a system changes at a given time. It depends both on the fields and on how they change with respect to the coordinates. The

Lagrangian in turn is written as a spatial integral of the Lagrangian density.

$$L = \int \mathcal{L}(\phi, \partial_u \phi) d^3 x. \tag{1.8}$$

To minimise the action, the Lagrangian density needs to fulfil the Euler-Lagrange equation

$$\partial_u \left(\frac{\partial \mathcal{L}}{\partial (\partial_u \phi)} \right) - \frac{\partial \mathcal{L}}{\partial \phi} = 0. \tag{1.9}$$

Here u is the time coordinate of the systems. In classical mechanics solving the Euler-Lagrange equation results in Newton's equation of motion. It will be easier to see this with an example. We take consider the motion of a non-relativistic particle of mass m in three dimensional space. The Lagrangian density is determined by the position and speed of the particle, L=Kinetic Energy - Potential Energy

$$\mathcal{L} = \frac{1}{2} m(\dot{x})^2 - V(x). \tag{1.10}$$

$\dot{x}$ is the derivative of the particle's position with respect to time, i.e velocity, and $V(x)$ is the potential in which the particle is moving. If we have a series of particles attached to each other with a spring then solving the Euler-Lagrange equation for the ith particle gives us

$$m \frac{d^2 x^i}{dt^2} = - \frac{\partial V(x)}{\partial x^i}, \tag{1.11}$$

or in more familiar terms as $F = ma$. This example lets us study the simple harmonic motion of a particle of mass m attached to a spring of force constant k. The energy of that system is the sum of kinetic energy of the particle,$\frac{1}{2} m(\dot{x}^2)$, and the potential energy of the spring, $\frac{1}{2} k x^2$. Here x is the position of the particle and $\dot{x}$ is differentiation with respect to time. Now if we have N particles each coupled to its neighbour by a spring, we can write the total energy of the system as

$$H = \sum_{i=1}^{N} \frac{1}{2} m(\dot{x}_i)^2 + \frac{1}{2} k(x_i - x_{i+1})^2. \tag{1.12}$$

Here H is the Hamiltonian of the system. $x_i - x_{i+1}$ is the distance between the two adjacent masses. In the continuum limit, where this distance goes to zero, the mass, m, is replaced by linear mass density, μ, the spring constant is replaced by Young's modulus, Y, and the Lagrangian of the system is

$$L = \int dx \frac{1}{2} \left[\mu(\dot{\phi}(x))^2 - Y \left(\frac{\partial \phi(x)}{\partial x} \right)^2 \right]. \tag{1.13}$$

Here we have replaced the position with a field $\phi(x,t)$ giving the displacement of the string from its equilibrium position x at time t. Solving the Euler-Lagrange equation gives us the wave equation,

$$\frac{\partial^2 \phi}{\partial x^2} - \frac{1}{v^2}\frac{\partial^2 \phi}{\partial t^2} = 0. \tag{1.14}$$

v is velocity of the wave expressed as $v = \sqrt{\frac{Y}{\mu}}$. Here we have gone from an equation of motion for a particle to equation of motion for a field. We can generalise this further by first invoking special relativity, i.e imposing the mass-shell condition , which gives the energy as

$$E = \pm\sqrt{p^2c^2 + m^2c^4}. \tag{1.15}$$

Here p is the momentum of the particle, m can be considered as a parameter of the field. Here we see that energy can be negative as well. We start by deriving an equation of motion for relativistic fields. For a free relativistic scalar field we write the Lagrangian density as

$$\mathcal{L} = \frac{1}{2}\hbar^2\Big(\frac{\partial \phi}{\partial t}\Big)^2 - \frac{1}{2}\hbar^2c^2\Big(\frac{\partial \phi}{\partial x}\Big)^2 - \frac{1}{2}m^2\phi^2. \tag{1.16}$$

Solving the Euler-Lagrange equation gives us equation (1.17). We can derive the equation another way, in non-relativistic quantum mechanics we make the position and momentum of the particle operators. According to the Schrodinger equation we have $\hat{p} \to -i\hbar\frac{\partial}{\partial x}$ and energy operator as , $\hat{E} \to i\hbar\frac{\partial}{\partial t}$. Replacing it in equation (1.15) we get

$$0 = \left[\frac{1}{c^2}\frac{\partial^2}{\partial t^2} - \frac{\partial^2}{\partial x^2} + \frac{m^2c^2}{\hbar^2}\right]\phi(x,t) \tag{1.17}$$

We can think of m as a parameter of the field. This equation is the well-known Klein-Gordon equation. We can think of this as relativistic form for the Schrodinger equation. The solutions are harmonic waves $u_k \sim e^{[i(kx-\omega t)]}$. Substituting this into (1.17) gives the dispersion relation

$$\omega = c\sqrt{k^2 - \frac{m^2c^2}{\hbar^2}}. \tag{1.18}$$

Here we see that in the limit of $m \to 0$ we get the dispersion relation of light in vacuum, $\omega = \pm ck$. In our attempt to understand the negative frequency and negative energy, we now quantize the fields. We interpret the classical fields as the expectation value of the operator of quantum field $\hat{\phi}(x,t)$. We introduce canonical momentum as

$$\Pi(x,t) = \frac{\partial \mathcal{L}}{\partial \dot{\phi}(x,t)}. \tag{1.19}$$

Canonical momentum, Π, is a measure of how quickly the Lagrangian density changes with respect to the gradient of the field. The transition from classical fields to quantum filed theory occurs when we impose the commutation relations between the field and its conjugate momenta:

$$[\phi(x,t), \Pi(y,t)] = i\hbar\delta(x-y). \tag{1.20}$$

We define a scalar product that quantifies the overlap between solutions in the solution space,

$$(\phi_1(x), \phi_2(x)) = -i \int \phi_1(x) \overleftrightarrow{\partial}_t \phi_2(x) dx. \tag{1.21}$$

The limit of the above integral is through the space-like surface of simultaneity at t. The symbol $\overleftrightarrow{\partial_t}$ is defined as

$$\phi_1 \overleftrightarrow{\partial}_t \phi_2 = \phi_1 \partial \phi_2 - (\partial\phi_1)\phi_2. \tag{1.22}$$

Now we have all the tools to construct the solution space. We start by Fourier transforming fields and conjugate momenta in k space.

$$\phi(x) = \int \frac{dk}{\sqrt{2\pi}} \frac{1}{\sqrt{2\omega_k}} \left[\hat{a}(k)\exp(-ikx) + \hat{a}^\dagger(k)\exp(ikx)\right], \tag{1.23}$$

$$\Pi(x) = \int \frac{dk}{\sqrt{2\pi}} (-i)\sqrt{\frac{\omega_k}{2}} \left[\hat{a}(k)\exp(-ikx) - \hat{a}^\dagger(k)\exp(ikx)\right]. \tag{1.24}$$

$\hat{a}(k)$ and $\hat{a}^\dagger(k)$ are operator-valued Fourier coefficients. The frequency, ω_k, fulfills the dispersion relation (1.18). The commutation relation between the field and the conjugate momentum (1.20) leads to the commutation relation of $\hat{a}(k)$ and $\hat{a}^\dagger(k)$ operators

$$[\hat{a}(k), \hat{a}^\dagger(k')] = \delta(k-k'). \tag{1.25}$$

We write the Hamiltonian with respect to $\hat{a}(k)$ operators

$$H = \int \mathcal{H} dx. \tag{1.26}$$

Here $\mathcal{H}$ is the Hamiltonian density and is expressed as

$$\mathcal{H} = \frac{1}{2}(\dot{\phi}\Pi) - \mathcal{L}. \tag{1.27}$$

Using the Fourier coefficients to express the Hamiltonian density we get

$$\mathcal{H} = \omega_k \left(\hat{a}^\dagger(k)\hat{a}(k) + \frac{1}{2} \right). \tag{1.28}$$

We find the eigenstates of the Hamiltonian, i.e states which have a defined energy. The vacuum state or the lowest energy, is when the Hamiltonian is the minimum for that given state. Lowest energy state is defined as

$$\hat{a}(k)\left|0\right\rangle = 0. \tag{1.29}$$

$\hat{a}(k)$ and $\hat{a}^\dagger(k)$ are known as annihilation and creation operators. It is because the way they act on the energy eigenstates. Creation operator when acted upon a vacuum state results in a one-particle fock space

$$\hat{a}^\dagger(k)\left|0\right\rangle = \left|1_k\right\rangle \tag{1.30}$$

It also allows us to write multi-particle states such as

$$\hat{a}^\dagger(k_1)a^\dagger(k_2)...\hat{a}^\dagger(k_n)\left|0\right\rangle = \left|1_{k_1}, 1_{k_2}, ..., 1_{k_n}\right\rangle. \tag{1.31}$$

The norm of a solution is the scalar product with itself. The norm of these multi-particle states is positive. It is expressed in 'bra-ket' notation as

$$\left\langle k|k'\right\rangle = +\delta(k - k'). \tag{1.32}$$

The norm is positive because we have the appropriate sign in the commutation relation (1.25). If the sign of the commutation had been reversed then we would have negative norm states and negative probabilities that would violate unitarity. To preserve unitarity the negative norm states are required to be balanced by the positive norm states such that the total norm of the system is either positive or zero. This balance is also known as conservation of norm and we shall visit this later.

We have successfully discretized the fields and have defined energy eigenstates, creation and annihilation operators. We have carried out our theoretical formulation in flat space-time. In flat space-time the choice of bases to decompose our fields is unique and in turn the definition of creation and annihilation operators are unique as well. This means that there is a unique vacuum state. In curved space-time the story changes a bit. In flat space-time the operator, $\frac{\partial}{\partial t}$, eigenfunctions are defined to have positive frequency with respect to time, t. In curved space-time there is no killing vector to define a positive frequency with respect to time, t. There is no unique coordinate to decompose the fields into. There are many different complete bases in

which we can decompose our fields. For ease of physical understanding we decide to decompose the fields into two asymptotic regions, i.e the in basis and the out basis:

$$\phi(x) = \int dk \Big(a_{in}(k) \exp(-ikx) + a_{in}^\dagger(k) \exp(ikx) \Big), \tag{1.33}$$

$$\phi(x) = \int dk' \Big(a_{out}(k') \exp(-ik'x) + a_{out}^\dagger(k') \exp(ik'x) \Big). \tag{1.34}$$

For now treat the in and out bases as just two different complete orthogonal bases in which we can decompose our fields. We shall talk about the in and out bases in detail later. The two bases construct their own Fock spaces and have their own vacuum states

$$a_{in}(k) \,|0_{in}\rangle = 0 = a_{out}(k') \,|0_{out}\rangle \tag{1.35}$$

These two bases are related to each other by a linear transformation, namely Bogolubov transformation.

$$a_{in} = \alpha a_{out} + \beta^* a_{out}^\dagger \tag{1.36}$$

$$a_{in}^\dagger = \beta a_{out} + \alpha^* a_{out}^\dagger \tag{1.37}$$

Here α and β are Bogolubov coefficients and they full fill the following relations

$$|\alpha|^2 - |\beta|^2 = 1 \tag{1.38}$$

The condition (1.38) makes sure that the transformation between the bases (1.36) is unitary. Rewriting $a_{in} \,|0_{in}\rangle$ in out bases we write $\alpha a_{out} \,|0_{in}\rangle + \beta^* a_{out}^\dagger \,|0_{in}\rangle = 0$. This means that the vacuum state for in basis is not the same as the vacuum state for the out basis, i.e

$$a_{out} \,|0_{in}\rangle \neq 0 \tag{1.39}$$

In other words a vacuum state in one basis, i.e a state with no particles, can be teeming with particles in another basis. A more physical way to view this is as a scattering process where the vacuum state scatters off the curved space-time into particles. In the case when the vacuum is scattering off an event horizon these scattered fields are called the Hawking radiation.

1.1.3 Hawking Temperature

We have finally laid the theoretical foundation to understand Hawking radiation. The particle creation at the event horizon is a quantum phenomena. The vacuum state is in a constant flux where particles and anti-particles are being created and annihilating. As discussed in the previous section the event horizon causes asymmetry in space-time. Outside the event horizon fields can travel either towards or away from the event horizon but inside the event horizon fields can travel only away from the event horizon, i.e towards the singularity. The kinematics of the system is such that that positive norm modes outside the event horizon can escape away from the horizon and the negative norm mode falls in the black hole. The escaped positive norm modes are the particles escaping the event horizon and negative norm mode falling in the black hole have negative energy which reduces the energy of the black hole and eventually causes the black hole to evaporate away. Hawking radiation is also viewed as a black body radiation and the temperature of this radiation is given as

$$k_B T = \frac{\hbar c^3}{8\pi G M}. \tag{1.40}$$

k_B is the Boltzmann constant, $\hbar$ is the Planck's constant G is the Gravitational constant. This is a spectacular result, incorporating three fields of physics, thermodynamics, gravity and quantum mechanics. An interesting thing to note is that the only defining feature for a Schwarzschild black hole is its mass. The temperature depends only on mass. Larger the mass, the smaller the temperature of the radiation. For a black hole having the mass of our Sun the temperature of it will be mere $9.04 \times 10^{-8} K$. An astronomical black hole is millions of times more massive than the Sun and its temperature is orders of magnitude lower than the background temperature. This restricts an ability to measure Hawking radiation directly from a black hole.

1.1.4 Analogue event horizons

In this section I will give a brief history of experiments and strides made in the analogue event horizon field. It will include the early theory, Bose Einstein Condensates (BEC) based analog experiments, water/fluid based classical experiments and optical analogue experiments.

In 1981 Unruh published the paper that laid the foundation of the field of analogue gravity [11]. In this paper he shows that sonic waves travelling in a flowing fluid and waves travelling in curved space are kinematically and mathematically similar. He predicts that these sonic horizons in supersonic flowing fluids will also emit thermal radiation, i.e analogue Hawking radiation. Unruh followed this by another paper published in 1995 [12] to show that Hawking radiation is a low-frequency and low-energy phenomenon and thus changing the high-frequency dispersion relation does not change the evaporation process. This

result gave more confidence that analogue Hawking radiation could be observed in the lab. Understanding Hawking radiation as a kinematic process allowed us to decouple it from the black-hole dynamics [13] and gave us a glimpse of how to produce it in other physical systems. Jacobson and Volovik in 1998 [13, 14] made one of the first suggestions, to create analogue event horizons in superfluid Helium, though there were many technical challenges in creating an analogue event horizon in condensed matter. More ingenious and practical suggestions were proposed, like the one in [15, 16] where they proposed a system in a ring trap to make an analogue black hole and studied other stable systems in Bose-Einstein condensates. Theoretical and numerical study showed that the Hawking radiation from a sonic analogue event horizon will nevertheless be weak, around $70nK$, but measurable [17]. As progress in technology was made more suggestions on the detection of such weak radiation were proposed [18]. As Hawking radiation is produced in pairs, these pairs of particles are quantum- correlated with each other. As both the inside and outside regions of the analogue event horizon are experimentally accessible, one can measure the correlation of the particles and use it as a signature to isolate the Hawking radiation from other sources of radiation and noise [19]. More in-depth numerical studies were published for the Hawking radiation from a flowing condensate [20, 21]. They used a microscopic description of the system to numerically calculate the radiation flux and the correlation of the radiation and used the gravitational analogy to understand the results. This made clear that the numerical calculation did not rely on trans-Planckian assumptions. Jeff Steinhauer in 2014 claimed that he has finally observed self-amplifying Hawking radiation in his BEC [22]. However, there were discussions in the field where the experimental results could be reproduced numerically without invoking quantum fluctuations of the matter field [23]. This made the claim a bit controversial though it was still a great stride towards realising an event-horizon experimentally in BEC. Steinhauer followed this paper by his famous paper in 2016 [24] which measures the correlation of high-energy pairs produced instantaneously across the analogue event horizon. Though impressive the paper also attracted criticism [25] on its claim and kept the debate alive whether Hawking radiation has been measured or not. The criticism was based on the statistical treatment of the experimental results and also that the entangled phonons were produced with a frequency higher than the cutoff frequency.

Apart from Bose-Einstein condensates, water-wave experiments were proposed as well [26]. Water waves are easily manipulated by changing water depth and have the advantage that it does not require expensive instruments or materials. Even though water is not a quantum fluid it gives us an opportunity to have insight in the classical instabilities caused by the event horizon. The first water tank experiment was achieved in 2008 [27]. Here the group observed the scattering of incoming waves onto an analogue horizon to negative waves. The experiment consisted of a water tank where a pump was used to make the water flow in a

specific direction, wave generator was used to produce water waves propagating against the flow of the water (medium) and a ramp was placed inside the tank to change the water flow speed, thus creating an analogue event horizon. The experiment observed the scattering of incoming positive waves to their negative counterparts from the ramp. However, the scattering was best observed when the flow was not actually in the horizon regime. This was because in the horizon regime the flow was too high and it caused turbulence and other disturbances making it difficult to observe the scattered waves. This paper was followed by another in-depth systematic analysis of water waves being scattered from an analogue white hole horizon [28]. Here the authors measured the amplitude of the scattered negative frequency waves and studied its behaviour while they varied the incoming frequency and amplitude. The amplitude variation showed that the negative frequency waves scaled linearly thus ruling out other nonlinear process. The frequency variation showed that the norm of negative frequency varied in a way that supported the thermal spectrum hypothesis as expected from an horizon. Furthering the experimental study Rousseaux studied the correlation of noise across an analogue event horizon [29]. All these experiments really opened a new door and gave us insights as to how, even without quantum behaviour, there are many classical features about the event horizon that one can understand in classical analogue experiments.

Making systems in optics to act as a analogue event horizon was more lucrative as photons are easier to manipulate and their quantum properties are easily exploited compared to condensed matter. Leonhardt made the first steps towards this realisation by drawing parallels between light propagating in gravitational fields and light propagating in moving dielectric media [30,31]. He showed that kinematically light experiences the same kind of metric when it is travelling in a gravitation field or in a moving dielectric. The first suggestion of such an optical system was extremely low group velocity of light in a moving medium [32–34]. The idea was that a moving medium drags light with it [35,36]. So if the medium moved like a vortex it would drag light with it and if light approaches close enough to the vortex core it will fall inside the vortex and would not be able to escape. Fulfilling this idea in a lab encountered many technological difficulties. Any media moving close to the speed of light would be hard to achieve. Leonhardt came up with another theoretical suggestion, here instead of a moving medium, the idea involved an Electromagnetically-Induced Transparency(EIT). A control beam will shine on the medium to make it transparent for a probe beam and then the intensity of the the control beam will be spatially varied. This will in theory create a region in the medium where the probe beam will slow down considerably creating a light catastrophe. Leonhardt predicted that this quantum catastrophe will make the quantum vacuum state to emit photons in either direction just like that in the case of an event horizon. Though other people argued that a quantum catastrophe of light will not produce a thermal spectrum like that of a Hawking radiation. So though an ingenious idea, it was never realised

in a lab. Nevertheless the idea of manipulating the medium's local properties with a strong beam of light was in the right direction. More people started studying and proposing optical systems which can produce an analogue event horizon [37, 38]. However, the proposals involved a physically moving dielectric medium and this was a problem experimentally, i.e how to move a medium at speeds comparable to the speed of light? In 2008 a new idea was proposed which solved this problem and was the first experimental success in demonstrating an analogue event horizon [39]. Here the idea was that an ultrashort intense pulse through the Kerr effect will locally change the refractive index of a highly nonlinear optical fiber as it propagates through it. As a probe light tries to catch up to the pulse, the probe light will experience the enhanced refractive index and will thus slow down and effectively be scattered by the back of the pulse and never able to overtake the pulse. This is an analogue white hole horizon. Similarly, the front of the pulse acts as an analogue black hole horizon. The paper also observed the classical scattering of light from the back of the pulse and measured the blue shift the probe light acquired from the event horizon.

This paper led to an upsurge in the field of optical analogue systems. It was followed by a couple of theoretical papers studying the flux and the regime of Hawking radiation in dispersive media [40] and from a travelling refractive index front [41]. Another experiment soon followed that used ultrashort laser pulse filaments in a bulk dispersive medium [42]. The intense laser pulse has a Kerr effect that changes the refractive index of the medium locally. They sent a pulse into a 3 cm slab of bulk silica. They focused the beam and varied the energy of the pulse so that they achieved the filamentation near the end of the medium. They observed that the spectrum of the input beam was split into two extra peaks, one blue-shifted and the other red-shifted. The paper claimed that this was due to the scattering from the front and then end of the intense pulse. They said that this was similar to effect observed in the 2008 paper [39]. Another experiment soon extended this work to claim to observe Hawking radiation from the above setup [43]. Though criticism and disputes over the interpretation of the results soon followed [44, 45]. The horizon in the experiments was a phase horizon, i.e. , the phase velocity of light outside the pulse is slightly greater than that of the light inside the pulse and the point at which the two phase velocities are equal is called a 'phase' horizon. There was no group velocity horizon, i.e the pulse group velocity was always greater than the probe. This difference showed that the metric of the said experiment did not resemble that of an analogue event horizon. Another puzzling observation was that the 'Hawking' photons were produced perpendicular to the direction of travel of the pulse because in theoretical models all the modes of emission were suppressed which were not longitudinal to the direction of the pulse. The observed radiation did not depend on the polarisation of light which was again contradictory to the theoretical model and the metric of the system. In summary, the claim was refuted that the source of the radiation was due to an analogue event horizon.

The discussions and debates gave people in the field a more concrete definition of analogue event horizons and allowed people to design more robust experiments. It also showed that more work was needed in order to understand the physics behind optical analogue event horizons. This gave the motivation to theoretically study optical systems in detail. A series of theoretical papers was published to theoretically derive the Hawking radiation in optical analogue experiments. The effort was to understand the effect dispersion plays in spontaneous emissions, which modes are responsible in the production of Hawking radiation, how the mixing of these modes happen and what roles do negative norm modes play in this arrangement. We shall discuss all this in the following chapter. We shall talk about different ways to approach the problem, for example whether to study the Hawking effect from the pulse propagation equation or to solve the Lagrangian for the medium where the pulse is seen as a disturbance in space in a co-moving frame.

Meanwhile, experiments were improving. In 2012, better control over the parameters of the pulse in an optical fibre translated into the observation of efficient frequency red-shifting and blue-shifting from a pulse [46]. The results of the experiment gave a more detailed understanding of the scattering phenomena observed in [39]. Simultaneously, the observation of negative frequency modes was made [47]. They did the experiment both in bulk silica and in an optical fibre and found similar results. In bulk silica a 60 fs pulse centered at 800 nm carrier wavelength was propagated where they varied the power of the input pulse. They observed a peak at 341 nm alongside a peak at 620 nm wavelength. The latter peak is the well known resonant frequency [48]. The former peak was called the negative resonant radiation. Resonant radiation happens when a soliton sheds light to a different mode with a different wavelength through a phase matched process in the presence of higher-order dispersion. However, it can also phase match with the negative branch of the dispersion relation and emit light by coupling to a negative frequency mode. The former peak at 341 nm was the experimental observation of this coupling with the negative mode. This work was further extended by studying this effect more in detail with regards to pulse compression [49]. Here the authors systematically studied the effect of chirp of the pulse and the generation of the negative resonant radiation (NRR) for a given length of the fiber. They noticed that the NRR spectrum is the strongest when the compression is happening near the end of the fiber and they found that significant NRR production happens during the compression of the pulse. These were important experimental results which laid down the path to future experiments to observe Hawking radiation from such systems.

Recently, in early 2019, another experimental milestone was achieved in optical analogue systems. Here the authors claimed to observe the stimulated Hawking radiation [50]. The experiment consisted of a pump pulse of 8 fs, centered at 800 nm wavelength coupled to a 7 mm optical fibre. The probe, i.e stimulation, was another pulse of much lower energy , $\approx 1\%$ of the pump pulse, and length of 50 fs with varied wavelength.

The authors first observed the NRR for just the pump pulse. Here they got a clear peak in the UV region. Then they observed the spectrum with both the probe and the pulse. Here they saw a much broader spectrum and after subtracting the pump NRR spectrum they numerically found a residual shifted peak. This shifted smaller peak was interpreted as the stimulated Hawking radiation. To further support their hypothesis, they showed that when the wavelength of the probe was varied the stimulated Hawking radiation also shifted as expected and the power of the stimulated Hawking radiation also varied linearly with the probe power. This was a promising result. It further demonstrated the promise of optical analogues and also opened doors to better more systematic study of simulated Hawking radiation. It also did leave many questions unanswered. How much impact did the non-linearity of the system have on the results? Would pulses with different lengths give better results? Does the dynamics and evolution of short pulses in optical fibers have a dramatic impact on the spectrum? What is the best setup to optimise the Hawking radiation production? How sensitive do our instruments need to be to observe non simulated Hawking radiation?

In the following chapters I attempt to answer some of the questions raised in the introductory chapter. At the same time I attempt to go deeply into the theoretical and numerical calculations for such optical systems discussed above.

Chapter 2

Electromagnetic waves in dielectric medium

Electromagnetic waves are governed by the Maxwell equations. The Maxwell equations are simplified into a wave equation which dictates the behaviour of electromagnetic waves. The Maxwell equations are written below in differential form .

$$\boldsymbol{\nabla} \cdot \mathbf{E} = \frac{\rho}{\epsilon_0}, \tag{2.1}$$

$$\boldsymbol{\nabla} \cdot \mathbf{B} = 0, \tag{2.2}$$

$$\boldsymbol{\nabla} \times \mathbf{E} = -\frac{\partial \mathbf{B}}{\partial t}, \tag{2.3}$$

$$\boldsymbol{\nabla} \times \mathbf{B} = \mu_0 \mathbf{J} + c^{-2} \frac{\partial \mathbf{E}}{\partial t}. \tag{2.4}$$

Here $\mathbf{E}$ and $\mathbf{B}$ are electric and magnetic field respectively. ρ is the charge density, Coulombs/m^3. $\mathbf{J}$ is the current density, Amperes/m^2. μ_0 and ϵ_0 are magnetic permeability and electric permittivity of vacuum, respectively. c is the speed of light and can also be expressed as $c = \frac{1}{\sqrt{\mu_0 \epsilon_0}}$. These four equations govern the electric and magnetic fields in empty space with some charge or current present. To simplify our analysis lets set $\rho = 0$ and $\mathbf{J} = 0$. We attempt to decouple electric and magnetic fields. First we take the curl of equation (2.3) and using vector identity write

$$\boldsymbol{\nabla} \times \boldsymbol{\nabla} \times \mathbf{E} = \nabla(\boldsymbol{\nabla} \cdot \mathbf{E}) - \nabla^2 \mathbf{E} = -\boldsymbol{\nabla} \times \frac{\partial \mathbf{B}}{\partial t}. \tag{2.5}$$

Applying equation (2.1) to equation (2.5) we find

$$\nabla^2 \mathbf{E} = \mathbf{\nabla} \times \frac{\partial \mathbf{B}}{\partial t} \tag{2.6}$$

We take the time derivative of equation (2.4) to find

$$\mathbf{\nabla} \times \frac{\partial \mathbf{B}}{\partial t} = c^{-2} \frac{\partial^2 \mathbf{E}}{\partial t^2} \tag{2.7}$$

We combine equations (2.6) and (2.7) to find

$$\nabla^2 \mathbf{E} - \frac{1}{c^2} \frac{\partial^2 \mathbf{E}}{\partial t^2} = 0 \tag{2.8}$$

Similarly for magnetic field we find

$$\nabla^2 \mathbf{B} - \frac{1}{c^2} \frac{\partial^2 \mathbf{B}}{\partial t^2} = 0 \tag{2.9}$$

These two equations are familiar. They are the wave equation for waves travelling at a speed of $c = \frac{1}{\sqrt{\mu_0 \epsilon_0}}$. This means that even with no current or charges present there are solutions for electric and magnetic field which are non zero. We can further simplify our equation by treating electric and magnetic fields as scalar fields and making the problem one dimensional in space. Doing so, we can rewrite the electric field equation as

$$\frac{\partial^2 E}{\partial x^2} - \frac{1}{c^2} \frac{\partial^2 E}{\partial t^2} = 0. \tag{2.10}$$

One of the common solutions to (2.10) is $E(x) = E_0 \exp(i(kx - \omega t))$ where E_0 is the amplitude of the wave, k is the wave number and ω is the angular frequency. Inserting the solution into the equation (2.10) we find the following relation which the wave number and angular frequency need to satisfy

$$\omega^2 = c^2 k^2. \tag{2.11}$$

Equation (2.11) is called the dispersion relation for vacuum. How do electric fields behave in a dielectric medium?

2.1 Electric fields in dielectric medium

Dielectric means an insulator, i.e flow of current is restricted. The material does not conduct electricity and the molecules do not have free electrons. Although it is electrically inert, the molecule itself can be

polarised in the presence of external electric field. With no external electric field, an atom can be seen as a hollow sphere whose surface is uniformly negatively charged and an equal but positive charge that lies in the centre of the sphere. In the presence of an external electric field the neutral molecules acquire a dipole moment. The medium is said to be polarised. The polarisation field will be directly proportional to the applied electric field.

If the external electric field is a sinusoidal wave then the electrons in the atom/molecule oscillates with the electric field. The electric field acts as a driving force for the harmonic oscillations for the electrons. These vibrating electrons have their own electric fields called the polarization fields. The incident electromagnetic field and polarization field are coupled together in a dielectric medium and cannot be viewed or studied independently. We shall use the Hopfield model [51] description to study the coupling between the two fields.

2.1.1 Hopfield model

The frequency of the incident electromagnetic wave dictates the amplitude and the frequency of the harmonic motion of the electron in the medium. The molecule properties in the medium and the way they are structured to make a crystal lattice also determines the resonant frequencies and elasticity of the electron's harmonic motion. We shall assume that the dielectric medium is homogeneous, isotropic, source-free, non-conducting, lossless and linear. Homogeneous means that there is a translation symmetry. Isotropic means that there is a rotational symmetry. Source-free and non-conducting mean that there are no free charges and no free flowing current in the material. Lossless and linear mean that the dielectric constant, permittivity and permeability are constant and real with no imaginary component.

We consider a scalar electromagnetic field travelling in a one dimensional medium. Here we take into consideration three resonances of the material. We do this to obtain just enough theoretical detail to construct the dispersion diagram for fused silica. The Lagrangian density of the system is written as

$$\mathcal{L} = \frac{(\partial_T A)^2}{8\pi c^2} - \frac{(\partial_X A)^2}{8\pi} + \sum_{i=1}^{3} \left(\frac{(\partial_T P_i)^2}{2\beta_i \Omega_i^2} - \frac{P_i^2}{2\beta_i} + \frac{1}{c} A \partial_T P_i \right). \tag{2.12}$$

A is the electric potential field, and is related to the electric field as $E = -\frac{\partial A}{\partial X}$. T and X are time and space in the lab frame, i.e. the frame where the medium is at rest. β_i^{-1} are the elastic constants and Ω_i are the resonant frequencies of the medium. $(\beta_i \Omega_i^2)^{-1}$ is the inertia of the medium. P_i are the polarisation fields in the medium generated by the harmonic motion of the electrons. Solving the Euler-Lagrange equation gives the Maxwell's equation alongside the constitutive equation. This assumes that equation (2.12) is the correct

Lagrangian density for the system.

2.1.2 Lorentz Transformation

Our aim is to study the scattering of waves from an arbitrarily shaped moving scatterer in a lossless medium. The scatterer is moving with a constant velocity, v, and we neglect the back action onto the scatterer, e.g. it is not changing in shape, speed or amplitude as it travels in the medium. The scattering is best described in a frame that moves with the scatterer. To do so we apply a Lorentz boost to the lab frame coordinates as follows

$$t = \gamma(T - \frac{v}{c^2}X), \qquad\qquad x = \gamma(X - vT), \qquad\qquad (2.13)$$

where $\gamma = \frac{1}{\sqrt{1-\frac{v^2}{c^2}}}$. t and x are coordinates of the co-moving frame and, T and X are coordinates of the lab frame.

2.1.3 Lagrangian to Hamiltonian

The Lagrangian density in the new coordinates is

$$\mathcal{L} = \frac{\dot{A}^2}{8\pi c^2} - \frac{A'^2}{8\pi} + \sum_{i=1}^{3}\left[\frac{\gamma^2}{2\beta_i\Omega_i^2}(\dot{P}_i - vP_i')^2 - \frac{P_i^2}{2\beta_i} + \frac{\gamma}{c}A(\dot{P}_i - vP_i')\right]. \qquad (2.14)$$

Here dot and prime denote the derivatives with respect to t and x respectively. As discussed in the previous chapter, we introduce canonical momenta as follows

$$\Pi_A = \frac{\partial\mathcal{L}}{\partial\partial_t A} = \frac{\partial\mathcal{L}}{\partial\dot{A}}, \qquad\qquad \Pi_{P_i} = \frac{\partial\mathcal{L}}{\partial\partial_t P_i} = \frac{\partial\mathcal{L}}{\partial\dot{P}_i}. \qquad (2.15)$$

Using equation (2.14) we derive the canonical momenta as

$$\Pi_A = \frac{\dot{A}}{4\pi c^2}, \qquad\qquad \Pi_{P_i} = \frac{\gamma^2}{\beta_i\Omega_i^2}(\dot{P}_i - vP_i') + \frac{\gamma}{c}A. \qquad (2.16)$$

We use the fields and the canonical momenta to express the Hamiltonian density as

$$\mathcal{H} = \frac{1}{2}\left[\dot{A}\Pi_A + \Pi_A\dot{A} + \sum_{i=1}^{3}(\dot{P}_i\Pi_{P_i} + \Pi_{P_i}\dot{P}_i)\right] - \mathcal{L}. \qquad (2.17)$$

25

By substituting the term for, $\mathcal{L}$ and canonical momenta in equation (2.17) we get

$$\mathcal{H} = 2\pi c^2 \Pi_A^2 + \frac{A'^2}{8\pi} + \sum_{i=1}^{3}\left[\frac{\beta_i \Omega_i^2}{2\gamma^2}(\Pi_{P_i} - \frac{\gamma}{c}A)^2 + \frac{P_i^2}{2\beta_i} + v\Pi_{P_i}P_i'\right]. \tag{2.18}$$

2.1.4   Hamiltonian to motion of Equation

To find the equations of motion for the fields we solve the Hamiltonian equations

$$\dot{A}/\dot{P} = \frac{\partial \mathcal{H}}{\partial \Pi_{A/P}}, \qquad\qquad \dot{\Pi}_{A/P} = -\frac{\partial \mathcal{H}}{\partial A/P} + \frac{\partial \mathcal{H}}{\partial \partial_t A/P}. \tag{2.19}$$

Substituting the Hamiltonian density and conjugate momenta in the equations (2.19) we find the set of coupled equations.

$$\dot{A} = 4\pi c^2 \Pi_A, \tag{2.20}$$

$$\dot{P}_i = \frac{\beta_i \Omega_i^2}{\gamma^2}(\Pi_{P_i} - \frac{\gamma}{c}A) + vP_i', \tag{2.21}$$

$$\dot{\Pi}_A = -\frac{A''}{4\pi} + \sum_{i=1}^{3}\frac{\beta_i \Omega_i^2}{\gamma c}(\Pi_{P_i} - \frac{\gamma}{c}A), \tag{2.22}$$

$$\dot{\Pi}_{P_i} = -\frac{P_i}{\beta_i} + v\Pi_{P_i}'. \tag{2.23}$$

With three polarization fields we have 8 coupled equations and we can express them as an eigen-equation.

$$\begin{pmatrix} \dot{A} \\ \dot{P}_1 \\ \dot{P}_2 \\ \dot{P}_3 \\ \dot{\Pi}_A \\ \dot{\Pi}_{P_1} \\ \dot{\Pi}_{P_2} \\ \dot{\Pi}_{P_3} \end{pmatrix} = \mathcal{M} \begin{pmatrix} A \\ P_1 \\ P_2 \\ P_3 \\ \Pi_A \\ \Pi_{P_1} \\ \Pi_{P_2} \\ \Pi_{P_3} \end{pmatrix}. \tag{2.24}$$

Here $\mathcal{M}$ is expressed as

$$
\mathcal{M} = \begin{pmatrix}
0 & 0 & 0 & 0 & 4\pi c^2 & 0 & 0 & 0 \\
-\frac{\beta_1\Omega_1^2}{\gamma c} & ikv & 0 & 0 & 0 & \frac{\beta_1\Omega_1^2}{\gamma^2} & 0 & 0 \\
-\frac{\beta_2\Omega_2^2}{\gamma c} & 0 & ikv & 0 & 0 & 0 & \frac{\beta_2\Omega_2^2}{\gamma^2} & 0 \\
-\frac{\beta_3\Omega_3^2}{\gamma c} & 0 & 0 & ikv & 0 & 0 & 0 & \frac{\beta_3\Omega_3^2}{\gamma^2} \\
\frac{k^2}{4\pi} - \sum_{i=1}^{3}\frac{\beta_i\Omega_i^2}{c^2} & 0 & 0 & 0 & 0 & \frac{\beta_1\Omega_1^2}{\gamma c} & \frac{\beta_2\Omega_2^2}{\gamma c} & \frac{\beta_3\Omega_3^2}{\gamma c} \\
0 & \frac{-1}{\beta_1} & 0 & 0 & 0 & ikv & 0 & 0 \\
0 & 0 & \frac{-1}{\beta_2} & 0 & 0 & 0 & ikv & 0 \\
0 & 0 & 0 & \frac{-1}{\beta_3} & 0 & 0 & 0 & ikv
\end{pmatrix}
\tag{2.25}
$$

Here we have all the equations governing the polarization and potential fields in the dielectric medium. In case of three polarisation fields we have 4 coupled second order partial differential equations or 8 first order partial differential equations. Solving these equations with the appropriate boundary conditions will give us the scattering matrix for the system. The solution is an 8 dimensional vector that fulfills the matrix equation (2.24).

$$
V_\omega^\alpha = \bar{V}_\omega^\alpha \exp(ik_\alpha x - i\omega t)
\tag{2.26}
$$

Here V is the solution , $\bar{V}$ is an 8-component vector amplitude of the solution, k is the wavenumber, α is the mode. For a single frequency ω we can have several modes. Equation (2.24) has non-vanishing solutions only when

$$
\det[\mathcal{M} + i\omega I_8] = 0.
\tag{2.27}
$$

is fulfilled. Solving this gives us the dispersion relation as

$$
c^2 k_\alpha^2 = \omega^2 + \sum_{i=1}^{3}\left[\frac{4\pi\beta_i\gamma^2(\omega + vk_\alpha)^2}{1 - \frac{\gamma^2(\omega+vk_\alpha)^2}{\Omega_i^2}}\right].
\tag{2.28}
$$

Here we see that in our case for three polarisation fields we have 8 modes of k for every ω. Note that ω and k are frequency and wavenumber in the moving frame. As time and space is Lorentz boosted, wavenumber and frequency are boosted as well according to

$$
\Omega = \gamma(\omega + vk), \qquad\qquad K = \gamma\big(k + \frac{v\omega}{c^2}\big).
\tag{2.29}
$$

Here Ω and K are frequency and wavenumber in the lab frame. We rewrite the dispersion relation in the

Lab frame as

$$c^2 K^2 = \Omega^2 \tag{2.30}$$

This is the well known Sellmeir's dispersion relation. The eigen-solutions for the equation (2.24) are written as

$$
\bar{V}_\omega^\alpha = C_\omega^\alpha
\begin{pmatrix}
c \\
\dfrac{i\beta_1 \Omega}{1 - \frac{\Omega^2}{\Omega_1^2}} \\
\dfrac{i\beta_2 \Omega}{1 - \frac{\Omega^2}{\Omega_2^2}} \\
\dfrac{i\beta_3 \Omega}{1 - \frac{\Omega^2}{\Omega_3^2}} \\
\dfrac{-i\omega}{4\pi c} \\
\dfrac{\gamma}{1 - \frac{\Omega^2}{\Omega_1^2}} \\
\dfrac{\gamma}{1 - \frac{\Omega^2}{\Omega_2^2}} \\
\dfrac{\gamma}{1 - \frac{\Omega^2}{\Omega_3^2}}
\end{pmatrix}.
\tag{2.31}
$$

Putting this vector back in equation (2.24) we can check that this fulfills the equation. Here C_ω^α is a normalization constant. The way to calculate the normalization constant is described in the next section when we quantize the fields.

2.1.5   Quantizing the Fields

Until now everything has been classical. We have solved the Hamiltonian equations to find the equations of motion for the fields. To quantize the fields we need to impose the commutation relation and define a scalar product between the fields. The scalar product for the solutions are defined as

$$\langle V_1 | V_2 \rangle = \frac{i}{\hbar} \int dx V_1^\dagger(x,t) \eta V_2(x,t). \tag{2.32}$$

$V^\dagger$ is a complex conjugate of V. η is an 8×8 matrix defined as

$$
\eta =
\begin{pmatrix}
0 & I_4 \\
-I_4 & 0
\end{pmatrix}.
\tag{2.33}
$$

28

The commutation relations between the fields and their canonical momenta are

$$[A(x), \Pi_A(x')] = i\hbar\delta(x - x'), \tag{2.34}$$

$$[P_i(x), \Pi_j(x')] = i\hbar\delta_{ij}\delta(x - x'). \tag{2.35}$$

The electromagnetic field and the polarisation fields commute, as do the canonical momenta but each field with its canonical momentum partner do not commute. This is similar to the commutation relation described in equation (1.20). The scalar product itself is preserved with respect to time [52].

$$\partial_t \langle V_1 | V_2 \rangle = \frac{i}{\hbar} \int dx [\partial_t(V_1^\dagger)\eta V_2 + V_1^\dagger \eta \partial_t(V_2)] \tag{2.36}$$

$$= \frac{i}{\hbar} \int dx [V_1^\dagger \mathcal{M}^\dagger \eta V_2 + V_1^\dagger \eta \mathcal{M} V_2] \tag{2.37}$$

$$= \frac{i}{\hbar} \int dx V_1^\dagger [\mathcal{M}^\dagger \eta + \eta \mathcal{M}] V_2. \tag{2.38}$$

The equation (2.37) uses the equation (2.24) to write $\partial_t V = \mathcal{M}V$. We calculate $\eta\mathcal{M}$ as

$$\eta\mathcal{M} = \begin{pmatrix} \frac{k^2}{4\pi} - \sum_{i=1}^{3}\frac{\beta_i\Omega_i^2}{c^2} & 0 & 0 & 0 & 0 & \frac{\beta_1\Omega_1^2}{\gamma c} & \frac{\beta_2\Omega_2^2}{\gamma c} & \frac{\beta_3\Omega_3^2}{\gamma c} \\ 0 & \frac{-1}{\beta_1} & 0 & 0 & 0 & ikv & 0 & 0 \\ 0 & 0 & \frac{-1}{\beta_2} & 0 & 0 & 0 & ikv & 0 \\ 0 & 0 & 0 & \frac{-1}{\beta_3} & 0 & 0 & 0 & ikv \\ 0 & 0 & 0 & 0 & -4\pi c^2 & 0 & 0 & 0 \\ \frac{\beta_1\Omega_1^2}{\gamma c} & -ikv & 0 & 0 & 0 & -\frac{\beta_1\Omega_1^2}{\gamma^2} & 0 & 0 \\ \frac{\beta_2\Omega_2^2}{\gamma c} & 0 & -ikv & 0 & 0 & 0 & -\frac{\beta_2\Omega_2^2}{\gamma^2} & 0 \\ \frac{\beta_3\Omega_3^2}{\gamma c} & 0 & 0 & -ikv & 0 & 0 & 0 & -\frac{\beta_3\Omega_3^2}{\gamma^2} \end{pmatrix}. \tag{2.39}$$

Calculating $\mathcal{M}^\dagger\eta$ we see that $\eta\mathcal{M} = -\mathcal{M}^\dagger\eta$. Hence, equation (2.38) vanishes and the scalar product and is thus conserved with respect to time.

2.1.6 Normalising the Fields

The normalisation and orthogonality condition for the solutions is

$$\left|\langle V_{\omega_1}^{\alpha_1} | V_{\omega_2}^{\alpha_2}\rangle\right| = \delta(\omega_2 - \omega_1)\delta_{\alpha_2\alpha_1}. \tag{2.40}$$

We shall calculate the L.H.S of equation and impose it to the R.H.S to find the normalisation condition.

29

We write the scalar product explicitly

$$\langle V_{\omega_1}^{\alpha_1}|V_{\omega_2}^{\alpha_2}\rangle =\frac{i}{\hbar}\int dx\exp(-i(\omega_2-\omega_1)t+i(k_{\alpha_2}-k_{\alpha_1})x)\ \bar{V}_{\omega_1}^{\alpha_1\dagger}\eta\bar{V}_{\omega_2}^{\alpha_2} \tag{2.41}$$

$$=\frac{i}{\hbar}\left[2\pi\delta(k_{\alpha_2}-k_{\alpha_1})\exp(-i(\omega_2-\omega_1)t)\bar{V}_{\omega_1}^{\alpha_1\dagger}\eta\bar{V}_{\omega_2}^{\alpha_2}\right]. \tag{2.42}$$

The integral in equation (2.41) is from $-\infty$ to ∞ and we use the integral solution $\int dx\exp(ikx)=2\pi\delta(k)$ to write equation (2.42). This means that solutions with different wave-numbers, k, are orthogonal. Solutions with different frequencies and yet the same wavenumber are also orthogonal as these are eigen-solutions to an Hermitian matrix $\mathcal{M}$. This simplifies equation (2.42) to

$$\langle V_{\omega_1}^{\alpha_1}|V_{\omega_2}^{\alpha_2}\rangle =\frac{i}{\hbar}\left[2\pi\delta(k_{\alpha_2}-k_{\alpha_1})\delta(\omega_1\omega_2)\bar{V}_{\omega_1}^{\alpha_1\dagger}\eta\bar{V}_{\omega_2}^{\alpha_2}\right]. \tag{2.43}$$

Evaluating the term $\bar{V}_{\omega_1}^{\alpha_1\dagger}\eta\bar{V}_{\omega_2}^{\alpha_2}$ gives

$$i\bar{V}_{\omega_1}^{\alpha_1\dagger}\eta\bar{V}_{\omega_2}^{\alpha_2}=\frac{|C_\omega^\alpha|^2}{2\pi}\left[\omega+\sum_{i=1}^{3}\frac{4\pi\beta_i\gamma\Omega}{(1-\frac{\Omega^2}{\Omega_i^2})^2}\right]. \tag{2.44}$$

Differentiating the equation (2.30) we obtain (2.45), and in (2.46) the group velocity in the lab frame $V_g=\frac{d\Omega}{dK}$ and then (2.47) writes (2.44) in terms of group velocity.

$$2c^2K=2\Omega\frac{d\Omega}{dK}\left[1+\sum_{i=1}^{3}\frac{4\pi\beta_i}{\left(1-\frac{\Omega^2}{\Omega_i^2}\right)^2}\right], \tag{2.45}$$

$$V_g=\frac{d\Omega}{dK}=\frac{c^2K}{\Omega}\left[1+\sum_{i=1}^{3}\frac{4\pi\beta_i}{(1-\frac{\Omega^2}{\Omega_i^2})^2}\right], \tag{2.46}$$

$$\sum_{i=1}^{3}\left[\frac{4\pi\beta_i}{(1-\frac{\Omega^2}{\Omega_i^2})^2}\right]=\frac{c^2K}{\Omega V_g}-. \tag{2.47}$$

We use equation (2.47) to substitute in (2.44) to get

$$i\bar{V}_{\omega_1}^{\alpha_1\dagger}\eta\bar{V}_{\omega_2}^{\alpha_2}=\frac{|C_\omega^\alpha|^2}{2\pi}\left[\gamma(\Omega-vK)+\frac{\gamma c^2K}{V_g}-\gamma\Omega\right] \tag{2.48}$$

$$=\frac{|C_\omega^\alpha|^2\gamma c^2K}{2\pi V_g}\left[1-\frac{vV_g}{c^2}\right]. \tag{2.49}$$

Inserting equation (2.49) into equation (2.43) and noting

$$\delta(k_{\alpha_2}-k_{\alpha_3})\delta_{\omega_1\omega_2}=\left|\frac{d\omega}{dk}\right|_{k=k_{\alpha_2}}\delta(\omega_2-\omega_1)\delta_{\alpha_2\alpha_1}. \tag{2.50}$$

We rewrite equation (2.43) as

$$\left\langle V_{\omega_1}^{\alpha_1} \big| V_{\omega_2}^{\alpha_2} \right\rangle = \delta(\omega_2 - \omega_1)\delta_{\alpha_1\alpha_2} \frac{|C_\omega^\alpha|^2 \gamma c^2 K}{\hbar} \frac{|v_g|}{V_g}\left[1 - \frac{vV_g}{c^2}\right]. \tag{2.51}$$

We simply the expression further before imposing the normalisation condition (2.1.6) by eliminating the group velocity in the moving frame, v_g, by using the relativistic composition of velocities

$$v_g = \frac{V_g - v}{1 - \frac{vV_g}{c^2}}. \tag{2.52}$$

This simplifies the expression to

$$\left\langle V_{\omega_1}^{\alpha_1} \big| V_{\omega_2}^{\alpha_2} \right\rangle = \delta(\omega_2 - \omega_1)\delta_{\alpha_1\alpha_2} \frac{|C_\omega^\alpha|^2 \gamma c^2 K}{\hbar}\left[1 - \frac{v}{V_g}\right]. \tag{2.53}$$

Imposing the normalisation condition give the equation (2.1.6) the normalisation factor

$$|C_\omega^\alpha|^2 = \left| \frac{\gamma c^2 K}{\hbar}\left(1 - \frac{v}{V_g}\right) \right|^{-1}. \tag{2.54}$$

Substituting equation (2.46) back into equation (2.54) we eliminate group velocity to get an expression in terms of Lab frame wavenumber and frequency

$$|C_\omega^\alpha|^2 = \hbar \left| c^2\gamma(K - \frac{v}{c^2}\Omega) - v\sum_{i=1}^{3} \frac{4\pi\beta_i\gamma\Omega}{\left(1 - \frac{\Omega^2}{\Omega_i^2}\right)^2} \right|^{-1} \tag{2.55}$$

$$= \hbar \left| c^2 k_\alpha - v\sum_{i=1}^{3} \frac{4\pi\beta_i\gamma\Omega}{\left(1 - \frac{\Omega^2}{\Omega_i^2}\right)^2} \right|^{-1}. \tag{2.56}$$

We have successfully calculated the normalisation constant for the solutions. Before we move on to the find solutions and solve scattering problems we will note a few things.

2.1.7 Alternative solution space

One of the first things to note is that we defined the canonical momentum for the fields with the traditional convention, i.e. , in equation (2.15) we differentiate the fields with respect to time. This means that when we write the solution vector $V_\omega^{k\alpha}$ these are eigen-solutions for a given wavenumber. Hence when we calculate the scalar product we get the Dirac delta function for wave-numbers and Korenecker delta function for frequencies. Though our normalisation condition is discretizing in wavenumber and not in frequency, i.e

the frequency is continuous and wave-numbers are discretized. This is why we have to use the relation in equation (2.50) express our scalar product in the desired format. This discrepancy arises because in literature fields are decomposed on basis of wave-number basis. In our system, as moving frequency is conserved, we want to decompose the fields in a frequency basis. With this motivation one can take a more conventional route to define the canonical momentum and define a new solution space.

We can define new canonical momenta as follows

$$\Pi_A = \frac{\partial \mathcal{L}}{\partial \partial_x A} = \frac{\partial \mathcal{L}}{\partial A'}, \qquad\qquad \Pi_{P_i} = \frac{\partial \mathcal{L}}{\partial \partial_x P_i} = \frac{\partial \mathcal{L}}{\partial P_i'}. \qquad (2.57)$$

Here we have replaced time with space. These canonical momenta are expressed as

$$\Pi_A = -\frac{A'}{4\pi}, \qquad\qquad \Pi_{P_i} = -\frac{v\gamma^2}{\beta_i \Omega_i^2}(\dot{P}_i - vP_i') - \frac{v\gamma}{c}A. \qquad (2.58)$$

in contrast to (2.16). Following the same recipe to write down the Hamiltonian density, and solving the Hamilton equations to discover the equation of motion, we find

$$A' = -4\pi\Pi_A, \qquad (2.59)$$

$$P_i' = \frac{\beta_i \Omega_i^2}{v^2 \gamma^2}(\Pi_{P_i} + \frac{\gamma v}{c}A) + \frac{\dot{P}_i}{v}, \qquad (2.60)$$

$$\Pi_A' = -\frac{\ddot{A}}{4\pi c^2} - \sum_{i=1}^{3}\frac{\beta_i \Omega_i^2}{vc\gamma}(\Pi_{P_i} + \frac{\gamma v}{c}A), \qquad (2.61)$$

$$\Pi_{P_i}' = -\frac{P_i}{\beta_i} + \frac{1}{v}\partial_t \Pi_{P_i}. \qquad (2.62)$$

We can write a matrix equation similar to equation (2.24)

$$\begin{pmatrix} A \\ P_1 \\ P_2 \\ P_3 \\ \Pi_A \\ \Pi_{P_1} \\ \Pi_{P_2} \\ \Pi_{P_3} \end{pmatrix}' = \mathcal{M}_\omega \begin{pmatrix} A \\ P_1 \\ P_2 \\ P_3 \\ \Pi_A \\ \Pi_{P_1} \\ \Pi_{P_2} \\ \Pi_{P_3}. \end{pmatrix} \qquad (2.63)$$

32

Here $\mathcal{M}_\omega$ is expressed as

$$\mathcal{M}_\omega = \begin{pmatrix} 0 & 0 & 0 & 0 & -4\pi & 0 & 0 & 0 \\ \frac{\beta_1\Omega_1^2}{\gamma vc} & \frac{-i\omega}{v} & 0 & 0 & 0 & \frac{\beta_1\Omega_1^2}{v^2\gamma^2} & 0 & 0 \\ \frac{\beta_2\Omega_2^2}{\gamma vc} & 0 & \frac{-i\omega}{v} & 0 & 0 & 0 & \frac{\beta_2\Omega_2^2}{v^2\gamma^2} & 0 \\ \frac{\beta_3\Omega_3^2}{\gamma vc} & 0 & 0 & \frac{-i\omega}{v} & 0 & 0 & 0 & \frac{\beta_3\Omega_3^2}{v^2\gamma^2} \\ \frac{\omega^2}{4\pi c^2} - \sum_{i=1}^{3}\frac{\beta_i\Omega_i^2}{c^2} & 0 & 0 & 0 & 0 & -\frac{\beta_1\Omega_1^2}{vc\gamma} & -\frac{\beta_2\Omega_2^2}{vc\gamma} & -\frac{\beta_3\Omega_3^2}{vc\gamma} \\ 0 & -\frac{1}{\beta_1} & 0 & 0 & 0 & \frac{-i\omega}{v} & 0 & 0 \\ 0 & 0 & -\frac{1}{\beta_2} & 0 & 0 & 0 & \frac{-i\omega}{v} & 0 \\ 0 & 0 & 0 & -\frac{1}{\beta_3} & 0 & 0 & 0 & \frac{-i\omega}{v} \end{pmatrix} . \tag{2.64}$$

The eigen-solutions are, $V_\omega^\alpha = \bar{V}_\omega^\alpha \exp(ik^\alpha x - i\omega t)$, where $\bar{V}_\omega^\alpha$ is expressed as

$$\bar{V}_\omega^\alpha = C_\omega^\alpha \begin{pmatrix} c \\ \frac{i\beta_1\Omega}{1-\frac{\Omega^2}{\Omega_1^2}} \\ \frac{i\beta_2\Omega}{1-\frac{\Omega^2}{\Omega_2^2}} \\ \frac{i\beta_3\Omega}{1-\frac{\Omega^2}{\Omega_3^2}} \\ \frac{-ik^\alpha c}{4\pi} \\ \frac{-v\gamma}{1-\frac{\omega^2}{\Omega_1^2}} \\ \frac{-v\gamma}{1-\frac{\omega^2}{\Omega_2^2}} \\ \frac{-v\gamma}{1-\frac{\omega^2}{\Omega_1^3}} \end{pmatrix} . \tag{2.65}$$

The scalar product and the commutation relation with the new definition of canonical momentum also changes as follows

$$[A(t), \Pi_A(t')] = i\hbar\delta(t - t'), \tag{2.66}$$

$$\langle V_1|V_2\rangle = \frac{i}{\hbar}\int dt V_1^\dagger(x,t)\eta V_2(x,t). \tag{2.67}$$

Here space and time are interchanged compared to equation (2.32). The scalar product is conserved with respect to space, i.e.

$$\frac{d\langle V_1|V_2\rangle}{dx} = \frac{i}{\hbar}\int dt \left(\frac{dV_1^\dagger}{dx}\eta V_2 + V_1^\dagger\eta\frac{dV_2}{dx}\right) \tag{2.68}$$

$$= \frac{i}{\hbar}\int dt \, V_1^\dagger\left(\mathcal{M}_\omega^\dagger\eta + \eta\mathcal{M}_\omega\right)V_2. \tag{2.69}$$

We calculate and see that $\mathcal{M}_\omega^\dagger\eta = -\eta\mathcal{M}_\omega$. This shows that the scalar product is conserved with respect to space, i.e. the conservation of norm. Any scattering process involving the eigen-solutions conserves the norm. By definition the norm is conserved with respect to time because it integrates over time. The normalisation coefficient calculation is more straightforward. We calculate the scalar product as in equation (2.41),(2.42) we get

$$\langle V_{\omega_1}^{\alpha_1}|V_{\omega_2}^{\alpha_2}\rangle = \frac{i}{\hbar}[2\pi\delta(\omega_1 - \omega_2)\exp(i(k_{\alpha_2} - k_{\alpha_1})x)\,\bar{V}_{\omega_1}^{\alpha_1\,\dagger}\eta\bar{V}_{\omega_2}^{\alpha_2}]. \tag{2.70}$$

With the alternative definition of the V we calculate $V^\dagger\eta V$ as

$$2\pi i V_\omega^{\alpha\dagger}\eta V_\omega^\alpha = \frac{|C_\omega^\alpha|}{\hbar}\left[c^2 k_\alpha - \sum_{i=1}^3 \frac{4\pi\gamma v\beta_i\Omega}{(1-\frac{\Omega^2}{\Omega_i^2})^2}\right]. \tag{2.71}$$

Imposing the normalisation condition (2.1.6) we get the normalisation coefficient as (2.56). This is a much simpler and more natural derivation.

2.1.8   Positive and negative norm modes

Another thing to note is that the scalar product is not positive definite. If you look at equation (2.51) we can see that sign of the norm depends on $\frac{K}{V_g}\left(1 - \frac{vV_g}{c^2}\right)$. Both velocity, v, of the moving frame and group velocity, V_g, are less than the speed of light. Hence $1 - \frac{vV_g}{c^2}$ is always positive. Even for the case when $v = 0$ the norm will depend on $\frac{K}{V_g}$. The sign is positive if K and V_g are both positive, which means lab frequency, Ω, is also positive, or if K and V_g are both negative keeping Ω positive. Hence the sign of the norm equals the sign of lab frequency, Ω. So modes with positive lab frequency have positive norm and modes with negative lab frequency have negative norm.

2.1.9 Annihilation and Creation Operators

Following the discussion we write the the solutions decomposed in frequency space as

$$\hat{V} = \int d\omega \sum_{\alpha} \left(V_\omega^\alpha \hat{a}_\omega^\alpha + V_\omega^{\alpha*} \hat{a}_\omega^{\alpha\dagger} \right) \tag{2.72}$$

V is the sum of all solutions of all frequencies and all corresponding wavenumber modes. For a given frequency, ω, we have

$$\hat{V}_\omega = \sum_{\alpha} \left(V_\omega^\alpha \hat{a}_\omega^\alpha + V_\omega^{\alpha*} \hat{a}_\omega^{\alpha\dagger} \right) \tag{2.73}$$

We sum over all the modes for a given frequency. In our case solving the dispersion relation (2.30) will give us 8 modes for every frequency. Here $\hat{a}$ is defined as

$$\hat{a}_\omega^\alpha = \langle V_\omega^\alpha | V \rangle . \tag{2.74}$$

These are annihilation and creation operators for the fields. The commutation relation which govern these operators are

$$[\hat{a}_\omega^\beta, \hat{a}_{\omega'}^{\beta'\dagger}] = \delta(\omega - \omega')\delta_{\beta\beta'} \tag{2.75}$$

The properties of these operators are already discussed in the previous chapter. These operators define a vacuum state and populate possible states as shown. We shall revisit these operators in the future when we will study the scattering in our system.

2.2 Dispersion Diagram

The dispersion equation (2.30) has eight branches as shown in figure 2.1. As we have seen, positive lab-frame frequency are positive norm mode solutions and solutions with negative lab frame frequency have negative norm. We have a symmetric dispersion diagram with respect to both frequency, Ω, and wavenumber, K. On the same diagram we see the Lorentz boosted moving frame frequency, ω and moving-frame wavenumber, k. To find solutions for a given lab frequency, Ω, draw a horizontal line at that frequency and wherever the horizontal line intersects the dispersion curve is a possible solution.

In a simple setup, for example where there is a perfect mirror at rest, an electromagnetic wave is scattered where the lab frequency is conserved and the sign of the wavenumber changes, i.e. we can draw a line parallel to the x axis for a constant frequency and the two places at which the constant frequency line crosses the dispersion branches corresponds to the solutions allowed.
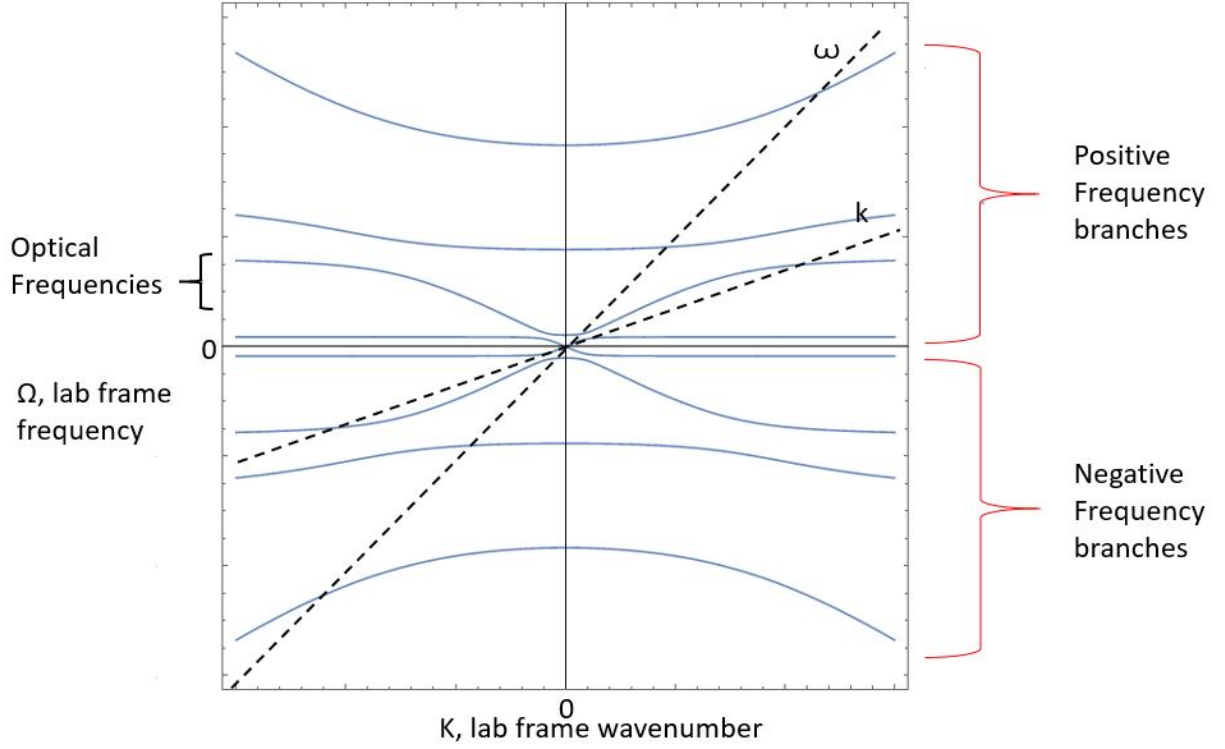
Figure 2.1: Dispersion diagram in the lab frame. Here we have drawn all eight branches. Horizontal axis is the lab frame wavenumber and the vertical axis is the lab frame frequency. The four branches in the top half of the quadrant have positive lab frame frequency and the four branches in the bottom half have negative frequency.

Now imagine the mirror moves, so that the light reflected from the mirror is Doppler shifted. The direction of the shift, blue or red will depend on the direction of the movement of the mirror. The lab frequency is not conserved in this scattering, but the moving-frame frequency is conserved. The moving-frame frequency is found by the Lorentz boost by equation (2.29). The moving frame frequency is now a slanted line in the dispersion diagram with a slope of $-v\gamma$. With any finite slope this constant frequency line intersects at most 8 times or 6 or 4. So for a given velocity, a constant frequency in the moving frame has 8 solutions, either all real or a combination of real and complex solutions. Complex solutions always come in pairs. This ensures solutions in the negative frequency branches. However, these solutions might be very far in the resonance having very small group velocity and will be absorbed as soon as they are generated. As the absorption coefficients are high in the resonance frequencies. If the mirror is moving with speeds comparable to speed of light, we excite solutions which are both negative and far from the resonances to not suffer significant absorption. This allows to observe the scattering of an incoming positive lab frequency to a negative lab frequency.

2.3 A step as a scatterer

It is hard to make an actual mirror travelling at speeds comparable to speed off light. However, we know that light can scatter off dielectric media. A monochromatic light wave is scattered by a strong pulse. Here the role of the mirror is played by a pulse. However, it is not a perfect mirror and some components of the scattered light will transmit across the pulse and some will be reflected back. To make the analysis simpler, we initially model the scatterer in 1D as a step pulse. Figure 2.2 shows a schematic.
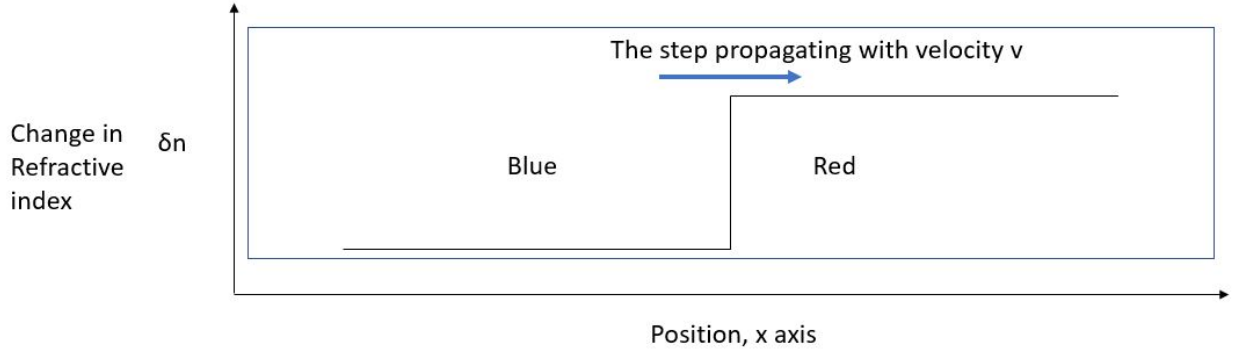
Figure 2.2: A step of some height δn is propagating towards the positive x direction. The two regions, left of the step is marked as blue and the right of the step is marked as red. This is because the two regions have slightly different dispersion relations.

The vertical axis in Figure 2.2 is the increase in refractive index due to the intensity of light. The dependence of refractive index of the medium on the intensity of light is called the Kerr effect. For all purposes in the moving frame the step is treated like a different medium with slightly different resonant frequency and elasticity. The resonant frequency and elasticity depends on the intensity according to

$$\beta_{i,R} = (1 + \epsilon)\beta_{i,L} \tag{2.76}$$

$$\Omega_{i,R} = (1 + \epsilon)^{-\frac{1}{2}}\Omega_{i,L}. \tag{2.77}$$

Here ϵ is a unit-less measure of the intensity and is related to the rise in non-linearity by

$$\delta n = n_R - n_B \approx \frac{n_B^2 - 1}{2n_B}\epsilon. \tag{2.78}$$

Note $\beta\Omega_i^2$ is the inertia of the media and is a constant that does not depend on intensity. In the blue region $\epsilon = 0$ in the dispersion relation. The dispersion changes at the boundary in the red region as a result of the change in resonant frequency and elasticity. Figure 2.3 shows an exaggerated difference between the dispersion curves of the two regions, blue and red. This change in dispersion curves makes the constant
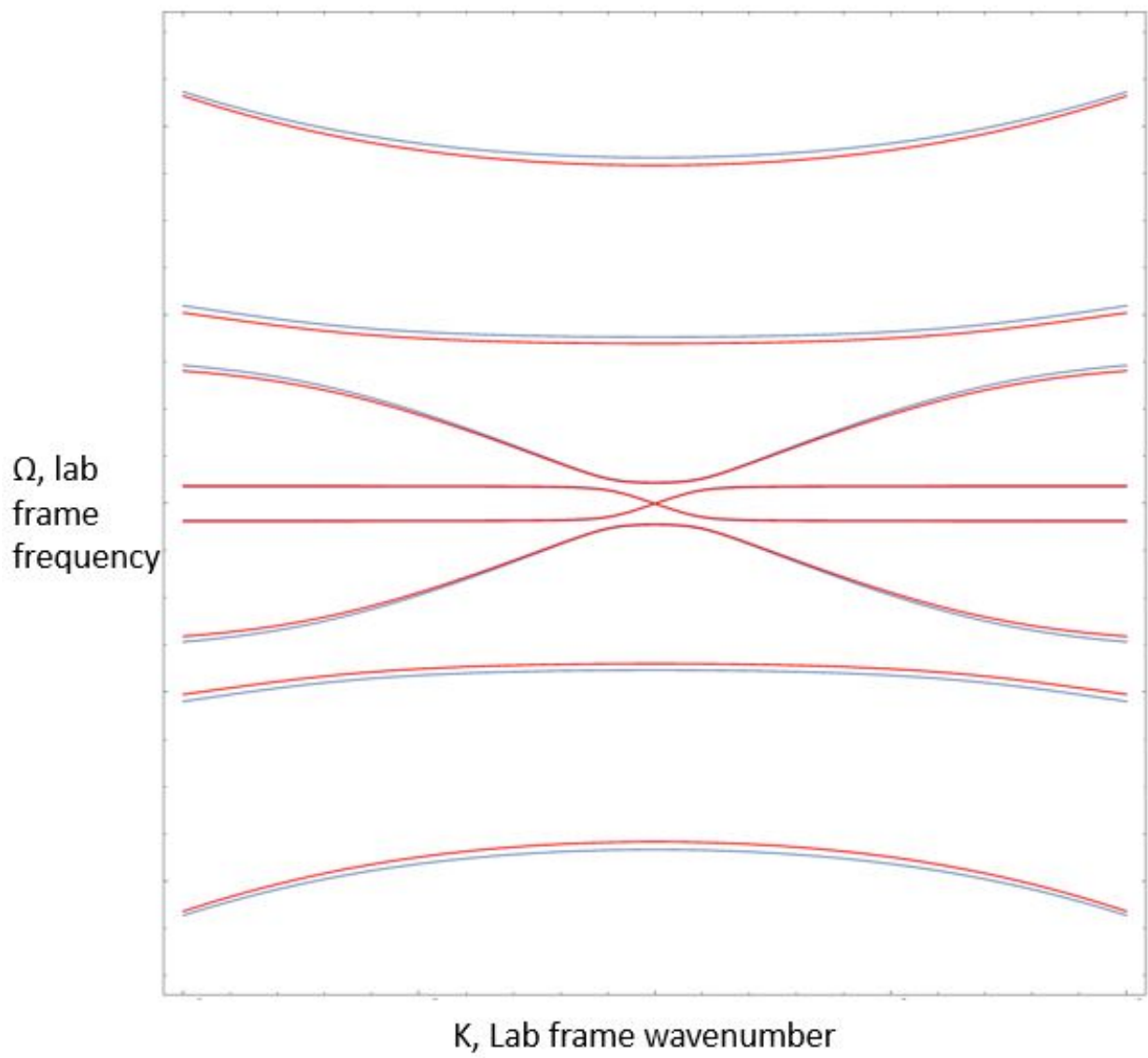
37

Figure 2.3: Two dispersion curves for the red and blue region as labelled in Figure 2.2. The curves are not to scale and are over-exaggerated for visual representation.

frequency line cross the dispersion curves at different places, displacing the modes. This means that an incident mode moving towards the step will be reflected and transmitted with different wave-numbers and frequencies. In order to encapsulate all the information about scattering we will employ a scattering matrix.

2.4   Scattering Matrix

Scattering matrices have been used in many fields of physics, from solid state to optics to quantum mechanics. Scattering matrices are useful in describing scattering problems and encapsulate all the information about the incoming and outgoing modes. Depending on the problem, different things play the role of the scatterer. For example, in a solid state problem a crystal lattice, in an optical problem a refractive index profile or in quantum mechanics the scattering potential. We study a toy setup in which we allow two modes to exist in the red and blue region in Figure 2.2. Using this toy setup we shall establish the generalised definition of the scattering matrix.

2.4.1   Mode Formalism

We label the two modes A and B. The red and blue regions have their own A and B modes, A_R, A_B, B_R and B_B , respectively. All the A modes have a group velocity towards the right in the moving frame and all the B modes are moving towards the left. This is shown in Figure 2.4.

Here we see that the blue modes, A_B and B_B exist only in the blue region and similarly in the red modes exist only in the red region. These modes are local and do not extend over all space. We define the A_B mode as

$$
A_B(x,t) = \begin{cases} \bar{A}_B \ e^{i(k_B^A x - \omega t)} & \text{if } x \in (-\infty, 0], \\ 0 & \text{otherwise.} \end{cases}
\tag{2.79}
$$

Here $\bar{A}_B$ is a scalar normalisation constant. k_B^A is the wavenumber of A mode in the blue region. As the moving frequency is conserved, we will drop the $e^{i\omega t}$ term. We construct a matrix of local modes in the blue region by combining the modes and their spatial derivatives.

$$
M_B = \begin{pmatrix} A_B & B_B \\ ik_B^A A_B & ik_B^A B_B \end{pmatrix},
\tag{2.80}
$$

The spatial derivatives are included as it is helpful in expressing the matching conditions at the interface of the step. Here the matrix M_B has all the information we need for the modes in the blue region. Similarly we construct M_R to put all the information of the red modes in layer red in a matrix.
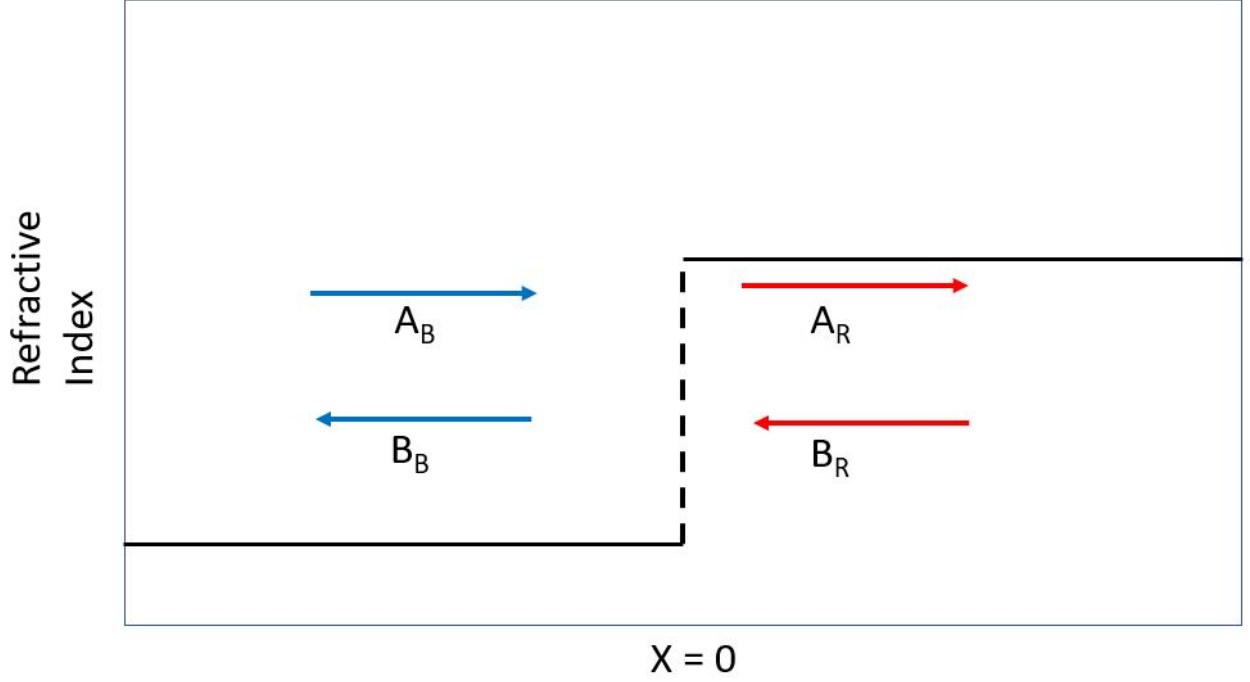
Figure 2.4: The step is at $x = 0$. The two regions of space are red region, inside the step, and blue region, outside the step. Both regions have their two modes, A and B, as shown in the diagram. The y axis is the jump in the refractive index.

2.4.2 Global Modes

Physically speaking we can have two scenarios for scattering. We can have an incoming A_B mode which then gets reflected to B_B and transmitted to A_R mode. The global solution of this scenario is written as

$$A_B^{in} = A_B + R_{AB}B_B + T_{AA}A_R. \tag{2.81}$$

R_{AB} is the reflection coefficient for the mode being reflected from A mode to B mode. T_{AA} is the transmission coefficient between the A modes. Here we have written a global solution for A_B. It is called a global solution because it is defined for all space. The mode A_B as shown in Figure 2.4 is travelling towards the step. So this global mode is called an incoming mode for A_B mode. Hence, the superscript of 'in' in the above notation. Similarly we define a second incoming global mode. This will be the B_R^{in} mode and is expressed as

$$B_R^{in} = B_R + R_{BA}A_R + T_{BB}B_B, \tag{2.82}$$

A_B^{in} and B_R^{in} are the incoming global modes. We can represent them in matrix form as

$$\zeta^{in} = M_B \sigma_B^{in} + M_R \sigma_R^{in}. \tag{2.83}$$

Here the σ's are matrices that contain the coefficients of the modes in the layer. Here they are defined as follows :

$$\sigma_B^{in} = \begin{pmatrix} 1 & 0 \\ R_{AB} & T_{BB} \end{pmatrix}, \tag{2.84}$$

$$\sigma_R^{in} = \begin{pmatrix} T_{AA} & R_{BA} \\ 0 & 1 \end{pmatrix}. \tag{2.85}$$

2.4.3 Matching Conditions

The global solutions have to be continuous and differentiable everywhere and also at the interface of the step, $x = 0$.

$$\zeta(x)|_{x=0_-} = \zeta(x)|_{x=0_+}. \tag{2.86}$$

We rewrite the matching condition (3.5) in terms of mode matrices M_B and M_R as follows:

$$M_B(x)|_{x=0_-} \, \sigma_B = M_R(x)|_{x=0_+} \sigma_R. \tag{2.87}$$

This is the reason we defined M with the harmonic fields and their spatial derivatives so that we can write the matching conditions more succinctly. We can rearrange this equation to express σ_R as

$$\sigma_R = I_{RB} \, \sigma_B \tag{2.88}$$

where $I_{RB} = M_R^{-1} M_B$. I_{RB} is the propagation matrix, it relates the coefficient matrix of one layer to the next layer. In this set up as there are only two layers, propagation matrix is also called the transfer matrix as it relates the coefficient matrix of two asymptotic layers.

2.4.4 Defining Scattering Matrix

Scattering matrices were first used by John Wheeler in 1937 [53] and have been used since then in describing many scattering problems in various fields, including optics [54, 55]. The scattering matrix relates the

incoming fields to the outgoing fields. An incoming mode as discussed before is a mode propagating towards the scatterer, the step. An outgoing mode is a mode propagating away from the step.

Physically, an incoming (outgoing) mode does not scatter into any other incoming (outgoing) mode, but only into outgoing (incoming) modes. All the incoming (outgoing) modes are linearly independent. We now introduce projector matrices to express the scattering matrix in a compact form. We use two projectors to project onto the modes of $M_{R/B}$ that move to the right (left) and to set all other modes to zero. The projectors P_{Right} and P_{Left} have the following properties: projector matrices are idempotent ($P^2 = P$), and orthogonal ($P_{\text{Left}} P_{\text{Right}} = P_{\text{Right}} P_{\text{Left}} = 0$). The sum of the projector matrices is the identity matrix ($P_{\text{Left}} + P_{\text{Right}} = \mathbb{1}$). Using the projectors we express the scattering matrix as

$$\mathcal{S}.(P_{\text{Right}}\ \sigma_B + P_{\text{Left}}\ \sigma_R) = P_{\text{Left}}\ \sigma_B + P_{\text{Right}}\ \sigma_R. \tag{2.89}$$

The projectors, P_{Right} and P_{Left}, in the above equation project onto the *right going* and *left going* mode coefficients of σ_B and σ_R, respectively. It is expressed as

$$P_{Right} = \begin{pmatrix} 1 & 0 \\ 0 & 0 \end{pmatrix}, \tag{2.90}$$

$$P_{Left} = \begin{pmatrix} 0 & 0 \\ 0 & 1 \end{pmatrix}. \tag{2.91}$$

$P_{\text{Right}}\ \sigma_B$ thus has non-zero entries only in the first row which contain the coefficients of the *right going* modes, or right movers, in region blue. $P_{\text{Left}}\ \sigma_R$ holds the *left* mover coefficients in region red. These two are all of the incoming mode coefficients for the system. Similarly, $P_{Left}\sigma_B + P_{\text{Right}}\sigma_R$ are all the outgoing mode coefficients of the system. The above equation (2.89) transforms the incoming wave coefficients into the outgoing wave coefficients.

In our above model solving equation (2.89) gives us

$$\mathcal{S} = \begin{pmatrix} T_{AA} & R_{BA} \\ R_{AB} & T_{BB} \end{pmatrix}. \tag{2.92}$$

The scattering matrix encapsulates all the information about the scattering process. All the transmission coefficients are in the diagonal position and the off-diagonal coefficients are the reflection coefficients. Here in our toy model setup the properties of the scattering matrix are quite straightforward and physical. The

scattering matrix is a unitary matrix, i.e. it transforms the incoming waves into outgoing waves while preserving the norm of the modes. As a consequence of being unitary, the transmission and reflection coefficients in every column follows the condition

$$|T|^2 + |R|^2 = 1. \tag{2.93}$$

This condition also makes physical sense as energy is conserved in the scattering process, the intensity of incident light is preserved, the same as that in outgoing light.

In the next chapter we discuss some numerical and analytical ways to calculate the scattering matrix in more complicated systems, with more than two modes in a region and in a multi-layer scattering problem. We will answer questions like, How the properties of scattering matrix changes when we include negative norm modes in our analysis? How does the event horizon kinematics manifest itself in the scattering theory picture? What is the most efficient way to calculate scattering matrices for stationary systems? How these scattering scenarios result in creating the kinematics of event horizon?

Chapter 3

Scattering Matrix

In the previous chapter we laid the foundations and the theoretical framework for our system. Here we will study in detail the scattering matrix and the algorithms used to calculate it. As discussed, the importance of the scattering matrix is that it encapsulates all the information about the system. We will build upon the toy model. Instead of having just an abrupt step we will study the scattering from a pulse with a smooth profile of change of reflective index. We will also define the mode configuration for a system with 8 modes in every layer. The number of right and left going modes will then not be same.

Staircase Approximation

There are various ways to solve the problem of scattering from a smooth profile. Although exact analytical solutions exist, typical calculations of scattering problems resort to approximations. For example, to describe a smooth scatterer analytically, the WKB or Born series approximation is frequently employed. The approximation may fail, however, if the scattering potential varies on the scale of the wavelength [56]. Thus, numerical methods are more widely applicable. Here the scattering potential is approximated by thin layers of constant potential and treated it as a multilayer scatterer. This is called the staircase approximation. In our case it will be divided into layers of constant refractive index. The setup is shown in Figure 3.1. The scattering problem is solved by calculating the scattering matrix. Figure 3.1 illustrates this for a sech^2-shaped scattering potential. The scatterer is divided into $N + 1$ layers of constant potential. In each layer, the finite set of harmonic waves is the set of 'modes'. *We assume that the modes are solutions of a dth ordered linear differential equation.* The outer, 'asymptotic' layers contain the asymptotic modes, i.e. incoming and outgoing modes. The scattering is a stationary process and the scattering potential does not depend on the time in the moving frame. Therefore, the moving frame frequency, ω, is conserved, i.e. the monochromatic

components of input states scatter into the respective monochromatic components of the output states. In each layer, we find the modes for frequency ω by solving the dispersion relation. Then we connect (match) these modes at the layer interfaces and thereby obtain global solutions for the whole system. The scattering matrix is the transformation of incoming global modes to outgoing global modes.
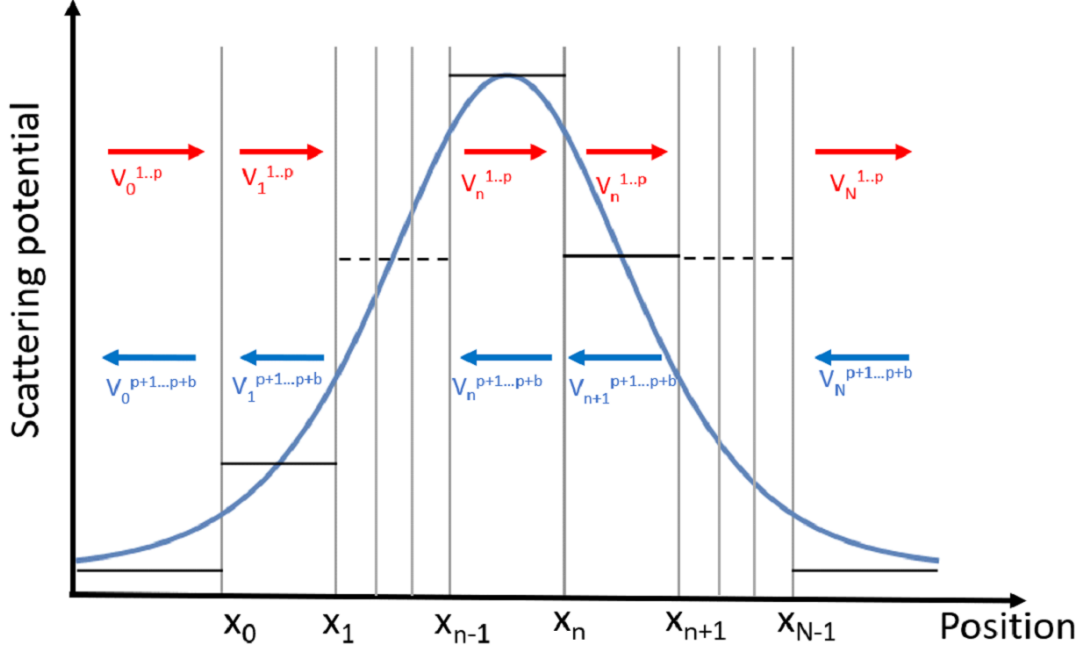

Figure 3.1: Scattering potential discretization into $N + 1$ layers and propagation of waves in a multilayer structure. $V_n^{1,2..p}$ and $V_n^{p+1,..,p+b}$ are the right and left propagating modes, respectively, in layer n.

Mode Formalism

The modes inside a layer n that share the frequency ω differ in wavenumber k and are characterized as follows: The wave solution is expressed as the harmonic fields

$$V_n^\alpha(x,t) = \begin{cases} \bar{V}_n^\alpha \ e^{i(k_n^\alpha x - \omega t)} & \text{if } x \in [x_{n-1}, x_n[\\ 0 & \text{otherwise,} \end{cases} \tag{3.1}$$

where $x_{-1} = -\infty$ and $x_N = \infty$. The upper index α ($\alpha = 1...(p+b)$) denotes the mode associated with wavenumber k_n^α. p is the number of right going modes and b is the number of left going modes with respect to the scatterer. As frequency is conserved, we will drop the $e^{i\omega t}$-term. The number of k modes depends on

the dispersion diagram. The $\bar{V}$ is a vector of dimension $p + b$, 8 in our case, and is defined as

$$\bar{V}_n^\alpha = C_\omega^\alpha \begin{pmatrix} \bar{A} \\ \bar{P}_1 \\ \bar{P}_2 \\ \bar{P}_3 \\ \bar{A}' \\ \bar{P}_1' \\ \bar{P}_2' \\ \bar{P}_3' \end{pmatrix} = C_\omega^\alpha \begin{pmatrix} c \\ \frac{i\beta_1\Omega}{1-\frac{\Omega^2}{\Omega_1^2}} \\ \frac{i\beta_2\Omega}{1-\frac{\Omega^2}{\Omega_2^2}} \\ \frac{i\beta_3\Omega}{1-\frac{\Omega^2}{\Omega_3^2}} \\ ik_n^\alpha c \\ -\frac{k_n^\alpha\beta_1\Omega}{1-\frac{\Omega^2}{\Omega_1^2}} \\ -\frac{k_n^\alpha\beta_2\Omega}{1-\frac{\Omega^2}{\Omega_2^2}} \\ -\frac{k_n^\alpha\beta_3\Omega}{1-\frac{\Omega^2}{\Omega_3^2}} \end{pmatrix}. \tag{3.2}$$

The first four components are the normalised amplitudes of the electromagnetic and the polarisation fields. The last four components are the spatial derivative of the first four. The amplitudes of the fields are the same as calculated and shown in equation (2.65) and the spatial derivative amplitude is calculated by multiplying the ik_n^α - term. We construct an 8×8 matrix with all the 8 modes of region n and define M_n as

$$M_n(x) = \begin{pmatrix} V_n^1(x) & V_n^2(x) & ... & V_n^8(x) \end{pmatrix} \tag{3.3}$$

For the single-step case n can be blue or red. Every column of M_n is an 8-dimensional vector as described in Equation (3.2). We would order the modes with respect to their group velocity in descending order. The wavenumber k may have an imaginary part. Complex modes have an envelope that can either exponentially grow or decay in x and have no defined group velocity. In order to categorize these exponentially growing and decaying modes either as a left or right going mode, we make a convention to treat exponentially growing modes as left going and vice versa.

The mode matrix M_n is layer-dependent, as the subscript n denotes. We construct a global matrix as a linear combination of local modes, M_n. We combine all the modes in all layers to construct an orthonormal [57] global solution for all x as

$$\zeta(x) = \sum_{n=0}^{N} M_n(x)\,\sigma_n. \tag{3.4}$$

The σ_n's contain the coefficients of the layer modes in the expansion of $\zeta(x)$. ζ, M_n and σ_n are $p+b$-dimensional square matrices. In our case $p + b = 8$.

Mode Propagation

The global solution of equation (3.4) is valid for all x. Because the scattering potential is finite, so is the field and its derivative across the interfaces of the staircase approximation. Therefore we write

$$\zeta(x)|_{x_{n+}} = \zeta(x)|_{x_{n-}}. \tag{3.5}$$

We rewrite the matching condition (3.5) in terms of mode matrices M_n as follows:

$$M_{n+1}(x_n)\,\sigma_{n+1} = M_n(x)|_{x_{n-}}\,\sigma_n. \tag{3.6}$$

The waves traveling within the layer pick up the phase $k_n^\alpha l_n$, where $l_n = x_n - x_{n-1}$ is the length of layer n. We introduce a diagonal 8×8 matrix κ_n, whose diagonal elements are the wavenumber of each mode:

$$\kappa_n = \begin{pmatrix} k_n^1 & 0 & 0 & 0 & 0 & 0 & 0 & 0 \\ 0 & k_n^2 & 0 & 0 & 0 & 0 & 0 & 0 \\ 0 & 0 & k_n^3 & 0 & 0 & 0 & 0 & 0 \\ 0 & 0 & 0 & k_n^4 & 0 & 0 & 0 & 0 \\ 0 & 0 & 0 & 0 & k_n^5 & 0 & 0 & 0 \\ 0 & 0 & 0 & 0 & 0 & k_n^6 & 0 & 0 \\ 0 & 0 & 0 & 0 & 0 & 0 & k_n^7 & 0 \\ 0 & 0 & 0 & 0 & 0 & 0 & 0 & k_n^8 \end{pmatrix}. \tag{3.7}$$

Hence, we define a matrix Φ_n of propagation phases as:

$$\Phi_n = e^{i\kappa_n l_n} \tag{3.8}$$

and thus:

$$M_n(x)|_{X_{n-}} = M_n(x_{n-1})\Phi_n. \tag{3.9}$$

Including the phase information in (3.6) we write

$$M_{n+1}(x_n)\,\sigma_{n+1} = M_n(x_{n-1})\,\Phi_n\,\sigma_n. \tag{3.10}$$

47

Equation (3.10) tells us how the modes are propagated through the layers. The mode amplitudes of one layer are related to the amplitudes of the adjacent layer as

$$\sigma_{n+1} = I_{n+1}\sigma_n, \tag{3.11}$$

where

$$I_{n+1} = M_{n+1}^{-1}(x_n)M_n(x_{n-1})\Phi_n. \tag{3.12}$$

The matrix I_{n+1} is called the propagation matrix and it relates the mode coefficients, or σ matrices, of layers n and $n+1$.

3.0.1 In/Out Global Modes

As in the previous chapter, we can define global in and global out modes. In a scattering problem we have incoming and outgoing fields. Local incoming modes are modes that propagate towards the scattering surface and local outgoing modes those that travel away from the scattering surface. For example, if we look at layer 0 in Figure 3.1, we see that all the right propagating modes in the asymptotic left region, $V_0^{1..p}$ in layer 0, and all the left propagating modes in layer N, $V_N^{p+1..p+b}$, will be incoming local modes. Similarly, all the left going modes in asymptotic left region, $V_0^{p+1..p+b}$, and all the right going modes in layer N, $V_N^{1..p}$, are outgoing local modes.

We define incoming and outgoing global modes. An incoming global mode is a linear combination of one defining incoming local mode and all outgoing modes. So for example, an incoming global mode, V_{IN}^1, will include local modes in every layer inside the pulse alongside with the modes in the asymptotic left and right regions, layer 0 and layer N. The defining feature of V_{IN}^1 is that the coefficient of the local incoming mode, V_0^1 is set to 1 and the coefficients of all the other incoming modes is set to 0. The coefficients of outgoing modes unknown. There are eight distinct incoming global modes which make up a complete basis to describe the system. Similarly, an outgoing global mode is defined by one of the local outgoing modes having the coefficient 1 and all the other outgoing local modes having coefficients 0. The outgoing global modes also make up a complete basis. For the regime where we have 1 right going mode and 7 left going modes, only V_0^1 will be the local incoming mode in asymptotic layer 0 and $V_N^{2..8}$ will be local incoming modes in layer

N. In this case, we write the σ matrices for global in mode as

$$
\begin{array}{c}
\begin{array}{ccccccccc}
LM \downarrow GM \rightarrow & V_{in}^1 & V_{in}^2 & V_{in}^3 & V_{in}^4 & V_{in}^1 & B_{in}^2 & B_{in}^3 & B_{in}^4
\end{array}\\
\begin{array}{c}
V_0^1 \\ V_0^2 \\ V_0^3 \\ V_0^4 \\ V_0^5 \\ V_0^6 \\ V_0^7 \\ V_0^8
\end{array}
\left(
\begin{array}{cccccccc}
1 & 0 & 0 & 0 & 0 & 0 & 0 & 0 \\
R_{12} & T_{22} & T_{32} & T_{42} & T_{52} & T_{62} & T_{72} & T_{82} \\
R_{13} & T_{23} & T_{33} & T_{43} & T_{53} & T_{63} & T_{73} & T_{83} \\
R_{14} & T_{24} & T_{34} & T_{44} & T_{54} & T_{64} & T_{74} & T_{84} \\
R_{15} & T_{25} & T_{35} & T_{45} & T_{55} & T_{65} & T_{75} & T_{85} \\
R_{16} & T_{26} & T_{36} & T_{46} & T_{56} & T_{66} & T_{76} & T_{86} \\
R_{17} & T_{27} & T_{37} & T_{47} & T_{57} & T_{67} & T_{77} & T_{87} \\
R_{18} & T_{28} & T_{38} & T_{48} & T_{58} & T_{68} & T_{78} & T_{88}
\end{array}
\right) = \sigma_0^{in}
\end{array}
\tag{3.13}
$$

$$
\begin{array}{c}
\begin{array}{ccccccccc}
LM \downarrow GM \rightarrow & V_{in}^1 & V_{in}^2 & V_{in}^3 & V_{in}^4 & V_{in}^5 & V_{in}^6 & V_{in}^7 & V_{in}^8
\end{array}\\
\begin{array}{c}
V_N^1 \\ V_N^2 \\ V_N^3 \\ V_N^4 \\ V_N^5 \\ V_N^6 \\ V_N^7 \\ V_N^8
\end{array}
\left(
\begin{array}{cccccccc}
T_{11} & R_{21} & R_{31} & R_{41} & R_{51} & R_{61} & R_{71} & R_{81} \\
0 & 1 & 0 & 0 & 0 & 0 & 0 & 0 \\
0 & 0 & 1 & 0 & 0 & 0 & 0 & 0 \\
0 & 0 & 0 & 1 & 0 & 0 & 0 & 0 \\
0 & 0 & 0 & 0 & 1 & 0 & 0 & 0 \\
0 & 0 & 0 & 0 & 0 & 1 & 0 & 0 \\
0 & 0 & 0 & 0 & 0 & 0 & 1 & 0 \\
0 & 0 & 0 & 0 & 0 & 0 & 0 & 1
\end{array}
\right) = \sigma_N^{in}
\end{array}
\tag{3.14}
$$

All the reflection and transmission coefficients are unknown. Every column of the sigma matrix is for a specific in global mode in Equations (3.13) (3.14). For example if we take the global 'in' mode V_{in}^1 ignoring all the modes within the pulse we express it as

$$
V_{in}^1 = V_0^1 + R_{12}V_0^2 + R_{13}V_0^3 + R_{14}V_0^4 + R_{15}V_0^5 + R_{16}V_0^6 + R_{17}V_0^7 + R_{18}V_0^8 + T_{11}V_N^1 \tag{3.15}
$$

The coefficient matrices σ_0^{out} and σ_N^{out} for out global modes are expressed as

$$
\begin{array}{c}
LM \downarrow GM \rightarrow \quad V_{out}^1 \quad V_{out}^2 \quad V_{out}^3 \quad V_{out}^4 \quad V_{out}^5 \quad V_{out}^6 \quad V_{out}^7 \quad V_{out}^8 \\
\begin{array}{c}
V_0^1 \\ V_0^2 \\ V_0^3 \\ V_0^4 \\ V_0^5 \\ V_0^6 \\ V_0^7 \\ V_0^8
\end{array}
\left(
\begin{array}{cccccccc}
X_{11} & X_{12} & X_{13} & X_{14} & X_{15} & X_{16} & X_{17} & X_{18} \\
0 & 1 & 0 & 0 & 0 & 0 & 0 & 0 \\
0 & 0 & 1 & 0 & 0 & 0 & 0 & 0 \\
0 & 0 & 0 & 1 & 0 & 0 & 0 & 0 \\
0 & 0 & 0 & 0 & 1 & 0 & 0 & 0 \\
0 & 0 & 0 & 0 & 0 & 1 & 0 & 0 \\
0 & 0 & 0 & 0 & 0 & 0 & 1 & 0 \\
0 & 0 & 0 & 0 & 0 & 0 & 0 & 1
\end{array}
\right) = \sigma_0^{out}
\end{array}
\qquad (3.16)
$$

$$
\begin{array}{c}
LM \downarrow GM \rightarrow \quad V_{out}^1 \quad V_{out}^2 \quad V_{out}^3 \quad V_{out}^4 \quad V_{out}^5 \quad V_{out}^6 \quad V_{out}^7 \quad V_{out}^8 \\
\begin{array}{c}
V_N^1 \\ V_N^2 \\ V_N^3 \\ V_N^4 \\ V_N^5 \\ V_N^6 \\ V_N^7 \\ V_N^8
\end{array}
\left(
\begin{array}{cccccccc}
1 & 0 & 0 & 0 & 0 & 0 & 0 & 0 \\
X_{21} & X_{22} & X_{23} & X_{24} & X_{25} & X_{26} & X_{27} & X_{28} \\
X_{31} & X_{32} & X_{33} & X_{34} & X_{35} & X_{36} & X_{37} & X_{38} \\
X_{41} & X_{42} & X_{43} & X_{44} & X_{45} & X_{46} & X_{47} & X_{48} \\
X_{51} & X_{52} & X_{53} & X_{54} & X_{55} & X_{56} & X_{57} & X_{58} \\
X_{61} & X_{62} & X_{63} & X_{64} & X_{65} & X_{66} & X_{67} & X_{68} \\
X_{71} & X_{72} & X_{73} & X_{74} & X_{75} & X_{76} & X_{77} & X_{78} \\
X_{81} & X_{82} & X_{83} & X_{84} & X_{85} & X_{86} & X_{87} & X_{88}
\end{array}
\right) = \sigma_N^{out}
\end{array}
\qquad (3.17)
$$

All the X coefficients are unknown. Here these X are not reflection or transmission coefficients but a combination of them and their inverses. As an example we can write the global out mode V_{out}^1 ignoring the modes within the pulse.

$$
V_{out}^1 = V_N^1 + X_{11}V_0^1 + X_{21}V_N^2 + X_{31}V_N^3 + X_{41}V_N^4 + X_{51}V_N^5 + X_{61}V_N^6 + X_{71}V_N^7 + X_{81}V_N^8 \qquad (3.18)
$$

In the case of 1 mode travelling towards the right and 7 to the left we define $P_{Right} = P_R$ and $P_{Left} = P_L$

as

$$P_R = \begin{pmatrix} 1 & 0 & 0 & 0 & 0 & 0 & 0 & 0 \\ 0 & 0 & 0 & 0 & 0 & 0 & 0 & 0 \\ 0 & 0 & 0 & 0 & 0 & 0 & 0 & 0 \\ 0 & 0 & 0 & 0 & 0 & 0 & 0 & 0 \\ 0 & 0 & 0 & 0 & 0 & 0 & 0 & 0 \\ 0 & 0 & 0 & 0 & 0 & 0 & 0 & 0 \\ 0 & 0 & 0 & 0 & 0 & 0 & 0 & 0 \\ 0 & 0 & 0 & 0 & 0 & 0 & 0 & 0 \end{pmatrix} \tag{3.19}$$

$$P_L = \begin{pmatrix} 0 & 0 & 0 & 0 & 0 & 0 & 0 & 0 \\ 0 & 1 & 0 & 0 & 0 & 0 & 0 & 0 \\ 0 & 0 & 1 & 0 & 0 & 0 & 0 & 0 \\ 0 & 0 & 0 & 1 & 0 & 0 & 0 & 0 \\ 0 & 0 & 0 & 0 & 1 & 0 & 0 & 0 \\ 0 & 0 & 0 & 0 & 0 & 1 & 0 & 0 \\ 0 & 0 & 0 & 0 & 0 & 0 & 1 & 0 \\ 0 & 0 & 0 & 0 & 0 & 0 & 0 & 1 \end{pmatrix} \tag{3.20}$$

3.0.2 Scattering Matrix

Even though now we have many more layers compared to the step in the toy model, the definition of the scattering matrix remains the same, i.e. it relates incoming asymptotic modes to outgoing modes. Hence the definition of the scattering matrix equation (2.89) still stands. Using σ^{in} matrices and following the equation for scattering matrix we find

$$\mathcal{S} = \begin{pmatrix} T_{11} & R_{21} & R_{31} & R_{41} & R_{51} & R_{61} & R_{71} & R_{81} \\ R_{12} & T_{22} & T_{32} & T_{42} & T_{52} & T_{62} & T_{72} & T_{82} \\ R_{13} & T_{23} & T_{33} & T_{43} & T_{53} & T_{63} & T_{73} & T_{83} \\ R_{14} & T_{24} & T_{34} & T_{44} & T_{54} & T_{64} & T_{74} & T_{84} \\ R_{15} & T_{25} & T_{35} & T_{45} & T_{55} & T_{65} & T_{75} & T_{85} \\ R_{16} & T_{26} & T_{36} & T_{46} & T_{56} & T_{66} & T_{76} & T_{86} \\ R_{17} & T_{27} & T_{37} & T_{47} & T_{57} & T_{67} & T_{77} & T_{87} \\ R_{18} & T_{28} & T_{38} & T_{48} & T_{58} & T_{68} & T_{78} & T_{88} \end{pmatrix} \tag{3.21}$$

As before, the scattering matrix is a matrix of all reflection and transmission coefficients. Though here we do not have an equal number of reflection and transmission coefficients as we had in our toy model. This is because we have broken the symmetry of left and right going modes. We have an unequal number of right and left going modes. Consequentially, using σ^{out} matrices, we have

$$\mathcal{S} = \begin{pmatrix} X_{11} & X_{12} & X_{13} & X_{14} & X_{15} & X_{16} & X_{17} & X_{18} \\ X_{21} & X_{22} & X_{23} & X_{24} & X_{25} & X_{26} & X_{27} & X_{28} \\ X_{31} & X_{32} & X_{33} & X_{34} & X_{35} & X_{36} & X_{37} & X_{38} \\ X_{41} & X_{42} & X_{43} & X_{44} & X_{45} & X_{46} & X_{47} & X_{48} \\ X_{51} & X_{52} & X_{53} & X_{54} & X_{55} & X_{56} & X_{57} & X_{58} \\ X_{61} & X_{62} & X_{63} & X_{64} & X_{65} & X_{66} & X_{67} & X_{68} \\ X_{71} & X_{72} & X_{73} & X_{74} & X_{75} & X_{76} & X_{77} & X_{78} \\ X_{81} & X_{82} & X_{83} & X_{84} & X_{85} & X_{86} & X_{87} & X_{88} \end{pmatrix}^{-1} \tag{3.22}$$

Another way to define the scattering matrix is as a transformation matrix from 'out' global modes to 'in' global modes and can be written as

$$\zeta_{in} = \zeta_{out}\mathcal{S}. \tag{3.23}$$

Here we substitute the global modes from equation (3.4) and multiply the local modes out as they are the same for a given layer. We get

$$\sigma_n^{in} = \sigma_n^{out}\mathcal{S}. \tag{3.24}$$

as this has to be true for all layers. If we include only the asymptotic layers then we can write

$$\mathcal{S} = (\sigma_{0/N}^{out})^{-1}(\sigma_{0/N}^{in})^{-1}. \tag{3.25}$$

These two expressions for the scattering matrix, (2.89) and (3.25), are similar. To come to a general equation for the scattering matrix in terms of only in/out sigma matrices we rewrite equation (3.25) as

$$(\sigma_{0/N}^{out})^{-1} = \mathcal{S}(\sigma_{0/N}^{in})^{-1} \tag{3.26}$$

We write $(\sigma_N^{in^{-1}})^{-1} = (P_R\sigma_N^{in} + P_L\sigma_N^{in})^{-1} = (P_R\sigma_N^{in} + P_L)^{-1}$. The inverse of a matrix of the form $(P_R\sigma_N^{in} + P_L)^{-1}$ will be also in the form $(P_RB + P_L)$, where B is some matrix. So $(\sigma_N^{in})^{-1} = (P_RB + P_L)$ then it has to be the case that $B = (\sigma_N^{in})^{-1}$. Hence we can write, $(\sigma_N^{in})^{-1} = (P_R\sigma_N^{in^{-1}} + P_L)$. From the matching

condition we can write

$$(\prod_{n=1}^{N} I_n)^{-1} = T_N^{-1} = \sigma_0^{in}(\sigma_N^{in})^{-1}. \tag{3.27}$$

We can rewrite (3.27) as

$$(\prod_{n=1}^{N} I_n)^{-1} = T_N^{-1} = (P1 + P2\sigma_0^{in})(P1(\sigma^{in_N} + P2))^{-1}. \tag{3.28}$$

We multiply P_R from the left side in (3.28) and we get

$$P_R T_N^{-1} = P_R \sigma_N^{in^{-1}}. \tag{3.29}$$

Adding P_L on both sides of (3.29) we get

$$P_R T_N^{-1} + P_L = (\sigma_N^{in})^{-1}. \tag{3.30}$$

Similarly we find the inverse of σ_N^{out} to be

$$P_L T_N^{-1} + P_R = (\sigma_N^{out})^{-1}. \tag{3.31}$$

Finally, putting all that together, the scattering matrix will then look like

$$\mathcal{S}(P_L\sigma_R^{in} + P_R\sigma_L^{in}) = (P_L\sigma_L^{in} + P_R\sigma_R^{in}). \tag{3.32}$$

3.1 Quantum vacuum emission

As in equation (2.72) 'in' and 'out' global modes supply two different complete bases in which to decompose our fields,

$$V = \int_0^{\infty} d\omega \left(\sum_{\alpha \in P} V_{in}^{\alpha} \hat{a}_{in}^{\alpha} + \sum_{\tilde{\alpha} \in N} V_{in}^{\tilde{\alpha}} \hat{a}_{in}^{\dagger\tilde{\alpha}} \right) + H.c. \tag{3.33}$$

$$= \int_0^{\infty} d\omega \left(\sum_{\alpha \in P} V_{out}^{\alpha} \hat{a}_{out}^{\alpha} + \sum_{\tilde{\alpha} \in N} V_{out}^{\tilde{\alpha}} \hat{a}_{out}^{\dagger\tilde{\alpha}} \right) + H.c. \tag{3.34}$$

Here we have not taken the limit to be from $-\infty$ to ∞ but from 0 to ∞ for the moving-frame frequency, ω. For a given frequency, ω, we sum over all the modes. The first term is the sum over all positive norm modes, that is what $\alpha \in P$ means, i.e. all the modes which have positive norm. Similarly the second term is the

53

sum over all the negative norm modes. The scattering matrix is a transformation matrix between these two complete bases. For example, we can write V_{in}^1 in terms of out global modes by using the scattering matrix coefficients as

$$V_{in}^1 = T_{11}V_{out}^1 + R_{12}V_{out}^2 + R_{13}V_{out}^3 + R_{14}V_{out}^4 + R_{15}V_{out}^5 + R_{16}V_{out}^6 + R_{17}V_{out}^7 + R_{18}V_{out}^8. \qquad (3.35)$$

The coefficients of the out modes are the same as the coefficient of their defining local mode in equation (3.15). Following the example of equations (3.33), (3.34), we write

$$V = \int d\omega (V_{in}\hat{A}_{in} + H.c) = \int d\omega (V_{out}\hat{A}_{out} + H.c), \qquad (3.36)$$

where $V_{in/out}$ is a row vector

$$\zeta_{in} = V_{in/out} = \begin{pmatrix} V_{in/out}^1 & V_{in/out}^2 & V_{in/out}^3 & V_{in/out}^4 & V_{in/out}^5 & V_{in/out}^6 & V_{in/out}^6 & V_{in/out}^7 & V_{in/out}^8 \end{pmatrix} \qquad (3.37)$$

and $\hat{A}^{in/out}$ contains all the annihilation and creation operators. For example if we have 5 positive and 3 negative norm modes ordered such that all the positive norm modes come first followed by negative norm modes we get

$$\hat{A}_{in/out} = \begin{pmatrix} \hat{a}_{in/out}^1 \\ \hat{a}_{in/out}^2 \\ \hat{a}_{in/out}^3 \\ \hat{a}_{in/out}^4 \\ \hat{a}_{in/out}^5 \\ \hat{a}_{in/out}^{\dagger 6} \\ \hat{a}_{in/out}^{\dagger 7} \\ \hat{a}_{in/out}^{\dagger 8} \end{pmatrix}. \qquad (3.38)$$

From the definition of the scattering matrix and equation (3.36) we arrive at

$$V_{in}\hat{A}_{in} = V_{out}\hat{A}_{out}, \qquad (3.39)$$

$$V_{out}\mathcal{S}\hat{A}in = V_{out}\hat{A}_{out}, \qquad (3.40)$$

$$\mathcal{S}\hat{A}_{in} = \hat{A}_{out}. \qquad (3.41)$$

Equation (3.41) shows that the scattering matrix is a Bogoliubov transformation [58]. It transforms the creation and annihilation of 'in' modes to 'out' modes. We can answer now how global in vacuum mode, $|0_{in}\rangle$, scatters into out modes. The global in vacuum mode is defined as

$$\hat{a}_{in}^{\alpha} |0_{in}\rangle = 0. \tag{3.42}$$

To calculate the emission from this vacuum in the mode V_{out}^1 we calculate the expectation value of the number operator, $\hat{N}_{out}^1 = \hat{a}_{out}^{\dagger 1} \hat{a}_{out}^1$. The expectation value is

$$\langle 0_{in}| \hat{N}_{out}^1 |0_{in}\rangle = \langle 0_{in}| \hat{a}_{out}^{\dagger 1} \hat{a}_{out}^1 |0_{in}\rangle. \tag{3.43}$$

We express $\hat{a}_{out}^1$ in terms of in operators as

$$\hat{a}_{out}^1 = \mathcal{S}_{11}\hat{a}_{in}^1 + \mathcal{S}_{12}\hat{a}_{in}^2 + \mathcal{S}_{13}\hat{a}_{in}^3 + \mathcal{S}_{14}\hat{a}_{in}^4 + \mathcal{S}_{15}\hat{a}_{in}^5 + \mathcal{S}_{16}\hat{a}_{in}^{\dagger 6} + \mathcal{S}_{17}\hat{a}_{in}^{\dagger 7} + \mathcal{S}_{18}\hat{a}_{in}^{\dagger 8} \tag{3.44}$$

Here $\mathcal{S}_{ij}$ is the component at i^{th} row and j^{th} column of the scattering matrix. Here we have assumed that the modes are ordered such that the first five modes are positive and the last three are negative norm modes. All the annihilation operators acting on the vacuum state result in zero. As the modes are orthogonal, it follows

$$\langle 1_{in}^{\alpha} | 1_{in}^{\tilde{\alpha}} \rangle = \delta_{\alpha\tilde{\alpha}}. \tag{3.45}$$

So the only terms survives to contribute are the coefficients of negative norm modes giving

$$\langle 0_{in}| \hat{N}_{out}^1 |0_{in}\rangle = |\mathcal{S}_{16}|^2 + |\mathcal{S}_{17}|^2 + |\mathcal{S}_{18}|^2. \tag{3.46}$$

We generalise this and say that the emission flux for every positive out mode is the sum of absolute squares of its respective negative norm modes. For a positive mode, α, we have

$$\langle 0_{in}| \hat{N}_{out}^{\alpha} |0_{in}\rangle = \sum_{\beta \in N} |\mathcal{S}_{\alpha\beta}|^2. \tag{3.47}$$

Similarly to other optical systems, Bogoliubov transformation dictates generation of quantum vacuum emission. Similar to a Bogoliubov transformation matrix, the scattering matrix has certain properties. The scattering matrix properties are discussed in the future sections.

3.2 Possible Mode Configurations

As we have discussed the dispersion relation in the last chapter, here we study possible solutions. We model bulk fused silica with three resonances [59, 60]. We set the central wavelength of the pulse to $800nm$. The group velocity of the pulse is calculated from Equation (2.46). The group velocity of the pulse of a central wavelength, $\lambda_p = 800$nm is $v_p = 0.66712 \times c$. The moving frame dispersion diagram is shown in Figure 3.2. Here we show only the positive optical branch of the dispersion diagram. The red curve is the dispersion
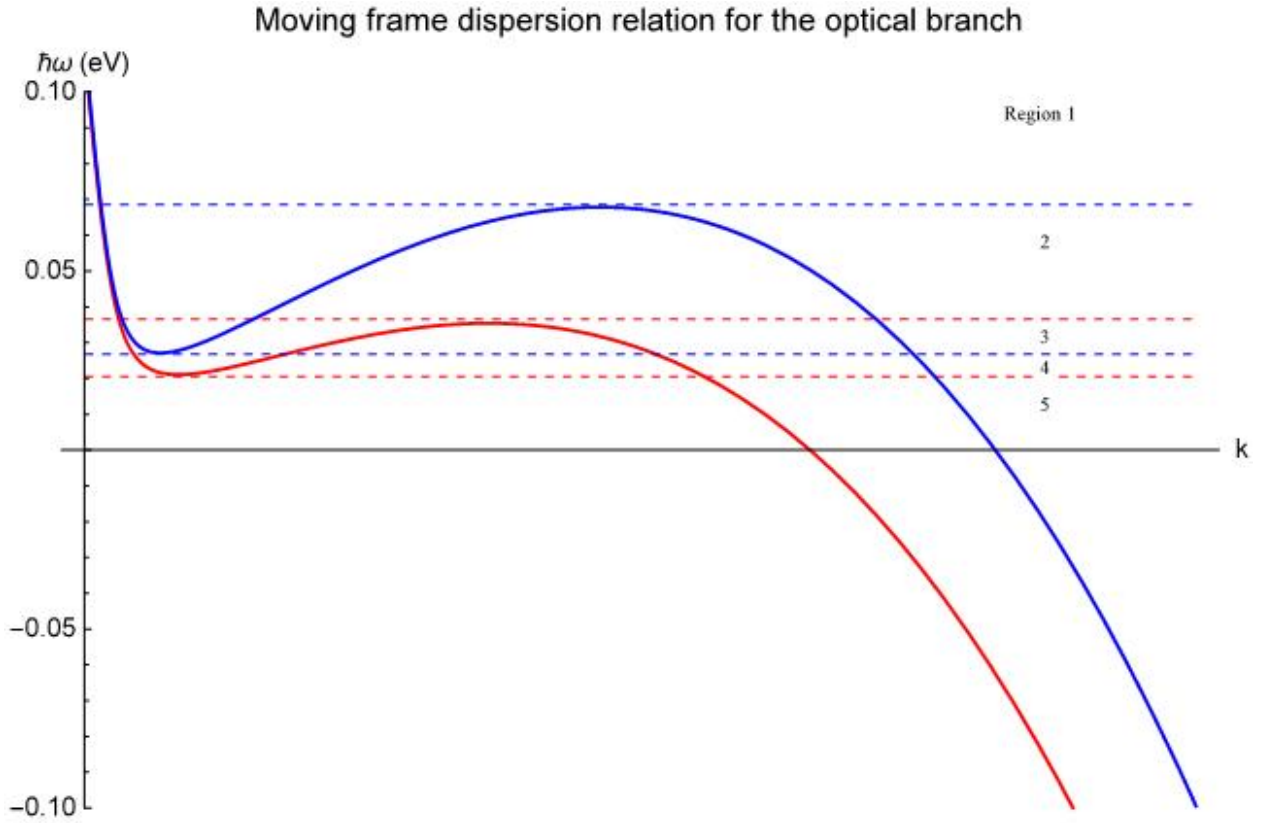
Figure 3.2: Moving frame dispersion diagram is plotted here, $\hbar\omega$ is the y axis and wavenumber, k, is the x axis. The curves are not to scale and are exaggerated for descriptive purpose. Only the positive optical branch is shown in the diagram. Solid blue curve is the dispersion diagram for the medium outside and the solid red curve is for inside the pulse. The energy range is divided into 5 regions as shown in the figure. Blue dotted and red dotted lines show the turning points for the curves respectively.

diagram inside the pulse. Here we have chosen the height and the velocity of the pulse so that we can show all the possible scenarios. The blue and red dashed lines shows the turning points of the blue and red branches respectively. The $\omega_{\min}$ and $\omega_{\max}$ are frequencies depicted as the lower and upper blue dashed lines. It signifies the turning point frequencies. There are 5 possible scenarios depending on the frequency chosen to solve the dispersion relation. If we choose the frequency so that it lies in either region 1, $\omega > \omega_{\max}$, or 5, $\omega < \omega_{\min}$, we have 1 optical mode both inside and 1 optical mode outside the pulse. In total we would

have 6 real modes everywhere and 2 complex modes. In this case there would be 6 in and out global modes and 2 in-physical modes. The in-physical modes would not scatter into any real modes and vice versa, this means that the scattering matrix will be a block matrix.

In region 2 we have the configuration shown in Figure 3.3. The pulse is modelled as top-hat pulse. In total we have three layers. Layers 0 and 3 are the asymptotic layers. At the back of the pulse, in layer 0, in Figure
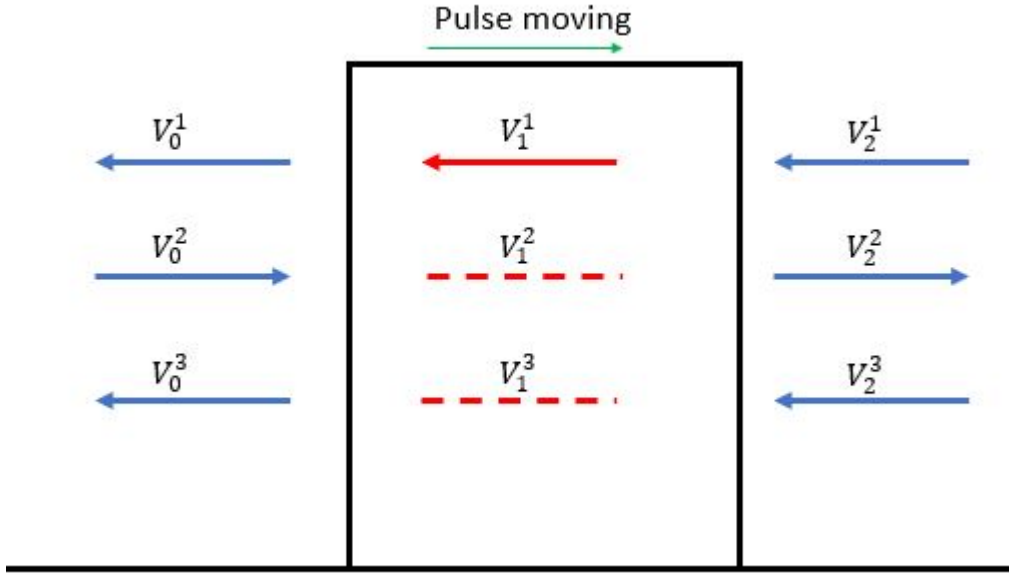

Figure 3.3: The mode configuration in region 2 is shown in the figure. The pulse is travelling towards the right. The modes are numbered as they intersect with a horizontal line in region 2 from left to right. Outside the pulse we have three real optical modes. Inside the pulse we have only one real and two complex optical modes.

3.3 modes cannot escape. Modes can travel either way outside of the pulse but only one way inside the pulse. This makes the leading edge of the pulse, between layer 1 and 2, an analogous black hole event horizon as modes can enter the pulse but can never escape from inside it. Similarly the back end of the pulse, between layer 0 and 1, is an analogous white hole as modes can only escape from the horizon but can never enter it. For Region 3 the mode configuration is shown in figure 3.4, here we have all real modes everywhere and no horizon physics play a role in this configuration.

For Region 4 the configuration is shown in Figure 3.5. Here all the modes are real inside the pulse and 2 complex modes outside the pulse. This configuration results in a block matrix because the there are two in-physical global modes as in case 1 and 5. The back end of the pulse is analogous to a black hole event horizon where the inside of the event horizon is the asymptotic layer 0. The front end of the pulse is analogous to white hole event horizon. The escaping modes from both the event horizons are trapped inside the cavity.
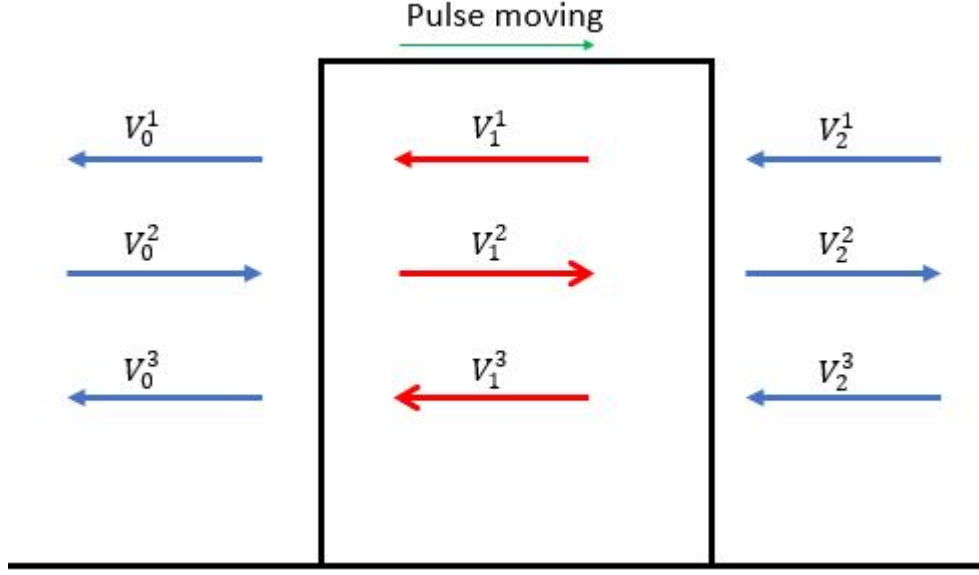
Figure 3.4: The mode configuration in Region 3 is shown in the figure. The pulse is travelling towards the right. The modes are numbered as they intersect with a horizontal line in region 3 from left to right. Outside the pulse we have three real optical modes. Inside the pulse we have three real optical modes.

This configuration is a black hole laser. The pulse acts like a cavity and could amplify the modes in theory

if the modes resonate inside the cavity.

In further calculations we will select the frequency such that we will be in one of these 5 mode configurations.

For a top-hat pulse or a step, we can select the pulse height and the speed of the pulse so that region 3 or 4

might not even exist since by increasing the pulse height we can lower the red dispersion curve.

3.3 Algorithms to calculate scattering matrix

As we have seen, the scattering matrix describes the scattering system completely. We need to calculate it. Calculating it analytically is not possible for our system because of its complexity. Solving the wave equation (2.24) numerically is also not possible as it is an ill-conditioned problem. We shall talk about this in detail in the proceeding section. We will solve the dispersion relation for a given frequency for every layer to get the possible modes. Enforcing the matching conditions, we will arrive at the scattering matrix through different algorithms.

3.3.1 T-Matrix algorithm

T-matrix algorithm is a straightforward, non-recursive method that allows us to find the transmission and reflection coefficients of waves from a scattering structure. In the T-matrix algorithm, the set of modes is
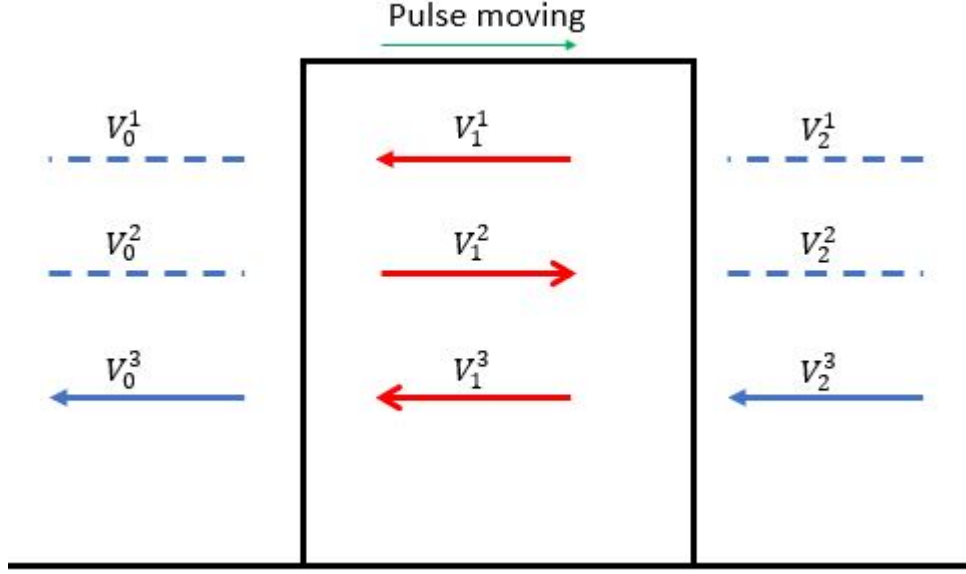
Figure 3.5: The mode configuration in region 4 is shown in the figure. The pulse is travelling towards the right. The modes are numbered as they intersect with a horizontal line in region 3 from left to right. Outside the pulse we have one real optical mode. Inside the pulse we have three real optical modes.

propagated through the 'layers' of the staircase approximation and then connected to the next layer using the matching conditions at the interface. Eventually this relates the asymptotic modes, thus determining the scattering coefficients for the entire system. However, in the presence of evanescent modes in the intermediate layers, the T-matrix algorithm can cause numerical instability [61]. The propagation matrices I_n defined in equation (3.12) transform the mode coefficients of layer 0, σ_0, into the mode coefficients of layer N, σ_N:

$$\sigma_N = \prod_{k=0}^{k=N-1} I_{N-k}\sigma_0 = T_N\sigma_0. \tag{3.48}$$

The transfer matrix T_N is the product of the propagation matrices. Substituting (3.48) into equation (2.89) we arrive at:

$$\mathcal{S}(P_R\sigma_0 + P_L T_N\sigma_0) = (P_L\sigma_0 + P_R T_N\sigma_0), \tag{3.49}$$

$$\mathcal{S} = (P_L + P_R T_N)(P_R + P_L T_N)^{-1}. \tag{3.50}$$

σ_0 and $P_R + P_L T_N$ are square and invertible matrices. This allows us to simplify equation (3.49) to (3.50). This formula gives a straightforward way to calculate the scattering matrix.

Since its introduction in 1965 [62], the T-matrix algorithm has been studied and modified extensively [63].

59

In the presence of evanescent modes, however, it becomes numerically unstable. As the evanescent waves propagate through the layers, the corresponding mode coefficients grow or decay exponentially. This causes the propagation matrices I_n in (3.48) to have a high condition number. Numerical operations, such as matrix inversion and products of these matrices will lead to numerical precision loss, i.e. the problem is ill-conditioned and becomes numerically unstable.

To demonstrate this, we employ the T-matrix algorithm and calculate the transfer matrix [1]. The algorithm is shown in Figure 3.6. The first two stages of the algorithm, yellow and green boxes, are common to all algorithm that we discuss in order to calculate the scattering matrix.

---

[1]We use the technical computing software Mathematica 11.2 from Wolfram Research.
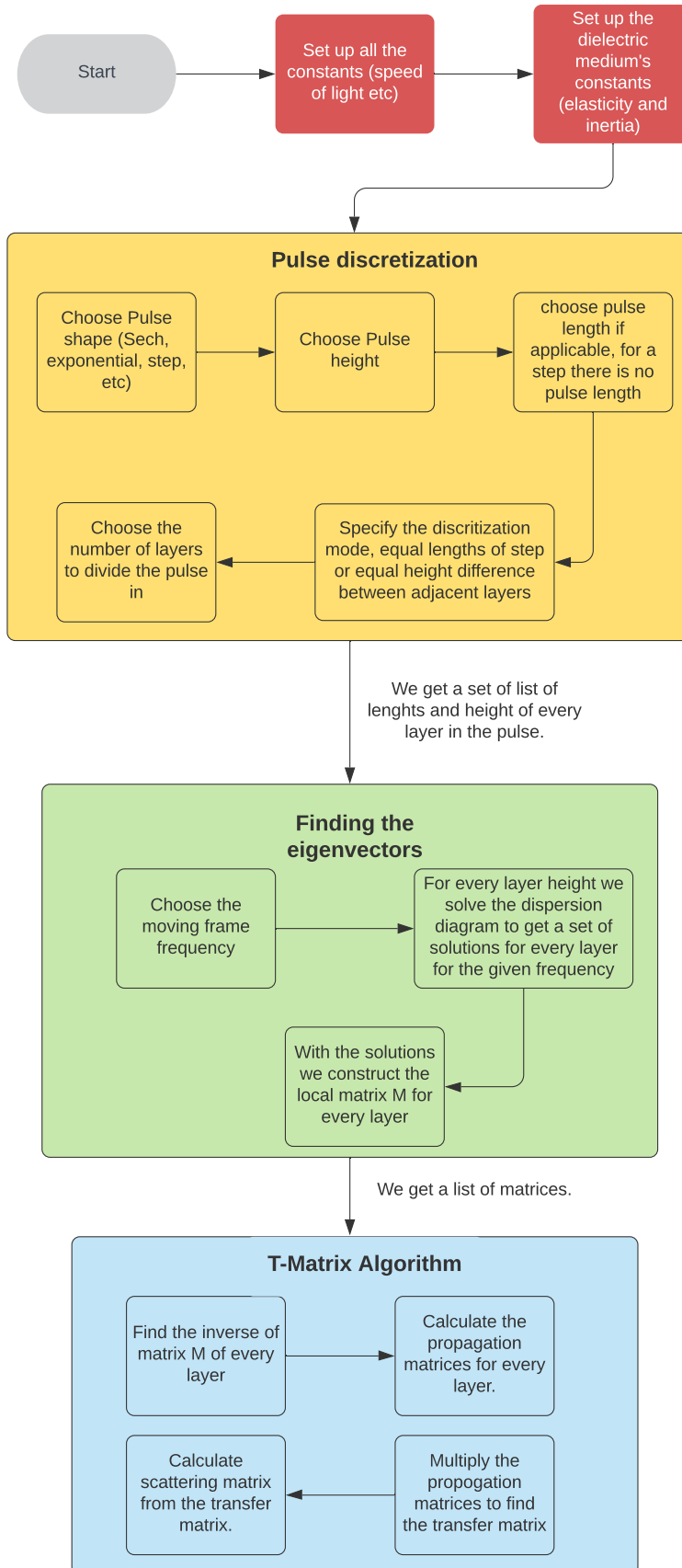
Figure 3.6: This shows the three stages in finding the scattering matrix. First stage, yellow, is about pulse discretization. The inputs are the pulse properties, like shape, height and length, and discretisation properties, number of layers and mode. The output is a set of lists of discretised layer lengths and layer heights .The second stage, green, is about finding the eigen-solutions. The input is a list of layer heights, moving frame frequency, ω and the dispersion relation for the medium. The output is a list of matrices of local modes for every layer, M_n. The third stage, blue, is where the T-matrix algorithm is employed. We calculate the propagation matrix, I_n, for every layer to multiply them out to calculate the transfer matrix.

Precision Problem

Precision in numerics is the number of decimal digits of a number which are significant for computations. Modern computers operate on either 32-bit or 64-bit. We operate on a 64-bit microchip. In numerical computation 1 bit is used for the sign of the number, 11 for the exponent and 52 for significant digits. The base is 2 so 2^{-52} is around 10^{-16}. This gives around 16 significant digits and is called the *Machine precision*. Most programming languages work in *Machine Precision*. Though *Mathematica* can carry out arbitrary-precision calculations as well. The user can specify the precision of the input number. So for example if we set the precision of an input number 0.6 to 20 we get 0.59999999999999997780. This is because computers work in base-2 not in base-10. So round-off errors happen in almost all numerical computations. Exact calculations happen when only integers are involved and no floating-point numbers are present. Some numerical calculations can cause the result to loose more precision than just the rounding errors. These numerical processes are unstable processes.

The computation of the scattering matrix from the transfer matrix done in machine precision of 16 digits fails with an error of insufficient precision. This forces our hand to use high precision numbers to calculate the scattering matrix by the T-matrix algorithm. In *Mathematica* one can perform arbitrary precision calculation. So we can specify an arbitrary precision for a number and the calculation will be carried out with that precision. We discretise the pulse into equal layer lengths and calculate transfer matrices from layer 0 to layer $k \leq N$. Figure 3.7 shows the precision of the resultant transfer matrices as k changes from 1 to N for a starting precision of 920 digits. The blue and green curves compare the loss of precision in 5-fs and 10-fs sech^2 pulses. Both pulses have been divided into 4000 layers over their length. The precision falls by as much as one digit every two layers, resulting quickly in a complete loss of precision and no result is obtained. The shorter pulse consists of shorter layers, resulting in a slower loss of precision per step. Blue and red curves are both for 5-fs pulses discretized into 4000 and 8000 layers, respectively. Doubling the number of layers (of half the length) again reduces the precision loss per layer. We see that the blue curve reaches zero around the 3000th layer, at 75% of total pulse length. For the red curve the precision falls to zero at the 5500th layer, at only 69% of the pulse length. Thus fewer longer layers seem slightly less affected by the instability, although a fine layering is required for convergence. Every time a numerical calculation is done, like finding an inverse of a matrix or multiplying out the matrix, precision drops. This is more evident especially when dealing with arbitrarily high-precision numbers. *Mathematica* overestimates the precision loss while doing arbitrarily precision calculations. While working out the potential effect of unknown digits in arbitrarily-precision numbers, it assumes by default that these digits are completely independent in different numbers [64]. The precision loss seen in Figure 3.7 is due to this overestimation of error. This overstates

62

the numerical instability of the T-matrix algorithm but shows why one needs to have high precision to begin with to get an accurate result for the transfer matrix.
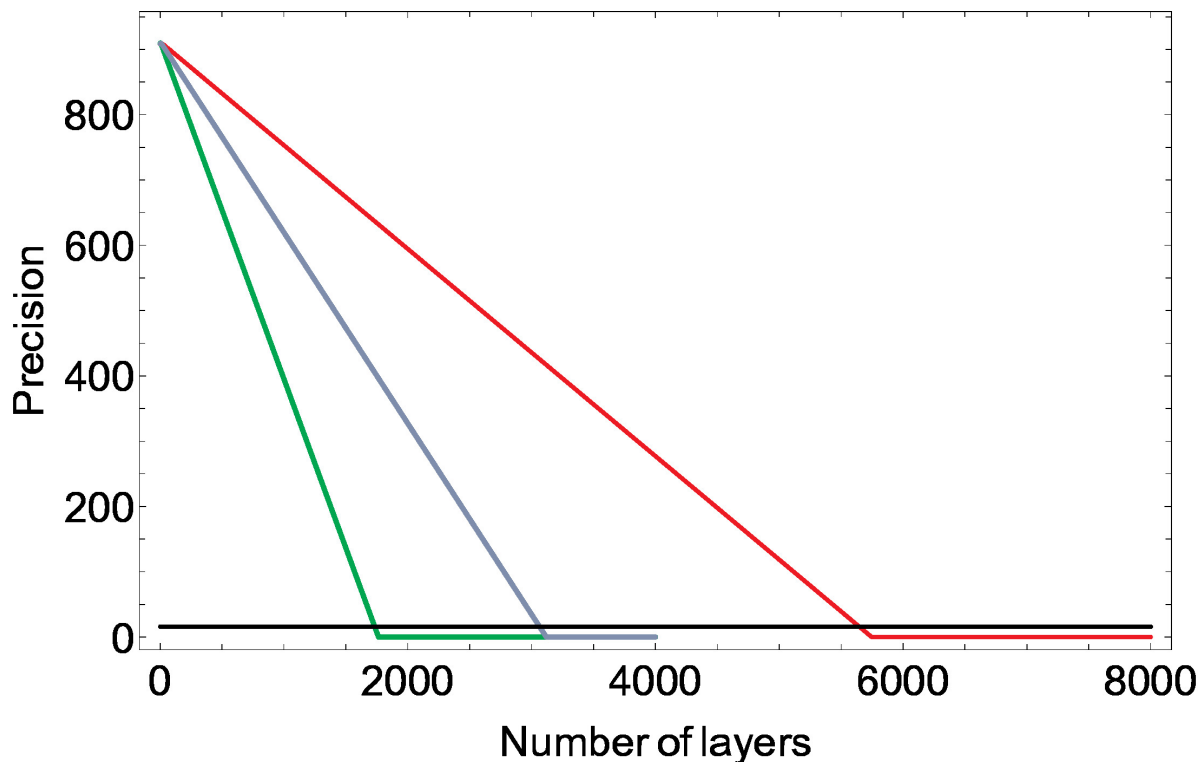

Figure 3.7: Precision loss in the T-matrix algorithm as a function of the number of layers traversed. The scatterer is a sech^2 pulse of 10-fs duration (green curve) and 5-fs (blue and red curve). For the blue and green curve the pulse is discretized into 4000 layers and the red curve is for a 5-fs pulse discretized into 8000 layers. Starting precision is 920 digits. The black line marks the machine precision at 16.

For a staircase approximation, a large number of layers is required, in particular with a large pulse duration. Hence, a high starting precision is required resulting in a long computation time. The disadvantage of using an arbitrary precision input is the huge amount of time it takes for computation. The advantage is that the answer you get is guaranteed to be precise. Setting the precision of numbers makes *Mathematica* keep track of the precision throughout the computation. This is not possible with *Machine Precision* numbers. So even a number with three digits of precision is considered more precise than a machine-precision number since *Mathematica* is able to track its precision using significance arithmetic [65]. When using *Machine Precision* one has to employ some other analytical, numerical checks to find out the precision and accuracy of the results.

Condition Number of a matrix

The condition number of a matrix is defined with respect to its norm, $\|\boldsymbol{\cdot}\|$. It is a measure of perturbations of the eigenvalues. Given a linear equation

$$Ax = b, \tag{3.51}$$

the condition matrix of A will dictate the ratio of change in x with respect to change in b. With det $A \neq 0$ and a perturbation of b by k, A by F and $(x + y)$ satisfies

$$(A + F)(x + y) = (b + k), A(I + A^{-1}F)y = k - Fx. \tag{3.52}$$

I is an Identity matrix. The magnitude of perturbation in solution is expressed as $\frac{h(y)}{h(x)}$ where h is any vector norm compatible with the matrix norm $\|A\|$. We can simplify this to write y as

$$y = (I + A^{-1}F)^{-1}A^{-1}k - (I + A^{-1}F)^{-1}A^{-1}Fx, \tag{3.53}$$

As F is a small perturbation we assume $\delta = \left\|A^{-1}\right\|\|F\| < 1$ and $\|I\| = 1$. We use the Schwarz's inequality and write $\left\|A^{-1}F\right\| \leq \left\|A^{-1}\right\|\|F\|$. We approximate equation (3.53) into [66]

$$h(y) \leq \frac{\left\|A^{-1}\right\|}{1 - \delta}h(k) + \frac{\delta}{1 - \delta}h(x), \tag{3.54}$$

To get to our desired ratio $\frac{h(y)}{h(x)}$ we note from equation (3.51) that $h(b) \leq \|A\|h(x)$. So we get

$$\frac{h(y)}{h(x)} \leq \frac{\|A\|\left\|A^{-1}\right\|}{1 - \delta}\frac{h(k)}{h(b)} + \frac{\delta}{1 - \delta}. \tag{3.55}$$

Here we can see that the ratio of the error is directly proportional to $\|A\|\left\|A^{-1}\right\|$. This is called the condition number of matrix A and is defined as $\kappa(A) = \|A\|\left\|A^{-1}\right\|$. For a square matrix and an euclidean norm defined as $\|A\| = \sqrt{\sum_{ij}|a_{ij}|^2}$ we express the condition number as

$$\kappa(A) = \frac{w_{max}(A)}{w_{min}(A)}. \tag{3.56}$$

$w_{max}(A)$ and $w_{min}(A)$ are maximal and minimal singular values of the matrix A. The condition number of a resultant matrix $C = AB$ follows $\kappa(C) \leq \kappa(A)\kappa(B)$. This means that the condition number of the resultant matrix can be lower than that of the input matrices. If the condition number is close to 1, the linear equation is a well-conditioned problem. If the condition number is high then the problem is ill-conditioned.

Ill-conditioned matrices result in huge numerical imprecision when calculating inverses or solving linear equations [67]. These can make an algorithm numerically unstable. The reason the T-matrix algorithm fails to compute at machine precision is because the transfer matrix has a high condition number in some cases. For the case when the scattering profile is a step, the T-matrix algorithm is stable. It works well with negligible precision loss of 1 or 2 digits. This loss is due to the round off errors. As we include more layers, the phase matrix, ϕ, comes into the calculation. We can see from Equation (3.7) that the phase matrix is a diagonal matrix. For the case where all the modes are real in all the layers, i.e. all the wave-numbers are real numbers, the T-matrix algorithm works well. Complex solutions come in pairs, so when the modes turn complex inside the layers we get at least two complex modes which are complex conjugate of each other. The diagonal term $\exp(ikl)$ grows exponentially for one of the complex k modes and it exponentially decays for the other. This makes the condition number of the phase matrix high. In turn the condition number of the propagation matrix becomes high. Multiplying the propagation matrices together further increases the condition number of the resultant transfer matrix. In Figure 3.8 we can see the rise in the condition number of the transfer matrix as soon as there are evanescent modes inside the layers as marked for the blue curve by the red dashed line. As soon as the modes turn real the condition number remains mostly the same. The magnitude of the rise of condition number depends on the pulse height and in turn on the magnitude of the imaginary part of the complex modes. When the imaginary part of the complex modes are bigger, the modes grow and decay faster. This makes the condition number of the transfer matrix high. We see that the condition number rises to a very big number. This is a clear indication that most numerical computations with such matrices will be highly unstable. We calculated the condition number by setting an arbitrarily high precision to the matrices to get an accurate result. We attempt to track the imprecision and inaccuracy in inverting these matrices. We invert the transfer matrices as we include more layers and note the inaccuracy by calculating the mean error. Error is expressed as δ_n and is calculated as $\delta_n = \mathbf{I}_8 - T_n^{-1}T_n$.

$$\bar{\delta}_n = \frac{\|\delta_n\|_1}{64}. \tag{3.57}$$

We divide it by 64 because δ_n is 8×8 matrix and has 64 elements. The mean error is plotted in Figure 3.9. We can see from Figure 3.9 that as we include the layers where evanescent modes exist the error in the inverse matrix increases rapidly. The rise in error is an indication that the number of significant figures in the inverse matrix of T_n is decreasing and *Mathematica* just fills numbers to keep it at *Machine Precision*. The error is also loosely related to the condition number of the matrix. The condition number gives a bound on how inaccurate the results can be, as in (3.55). Though the actual error depends on the specific algorithm used to find the inverse matrix. This shows that the T-matrix algorithm is numerically unstable
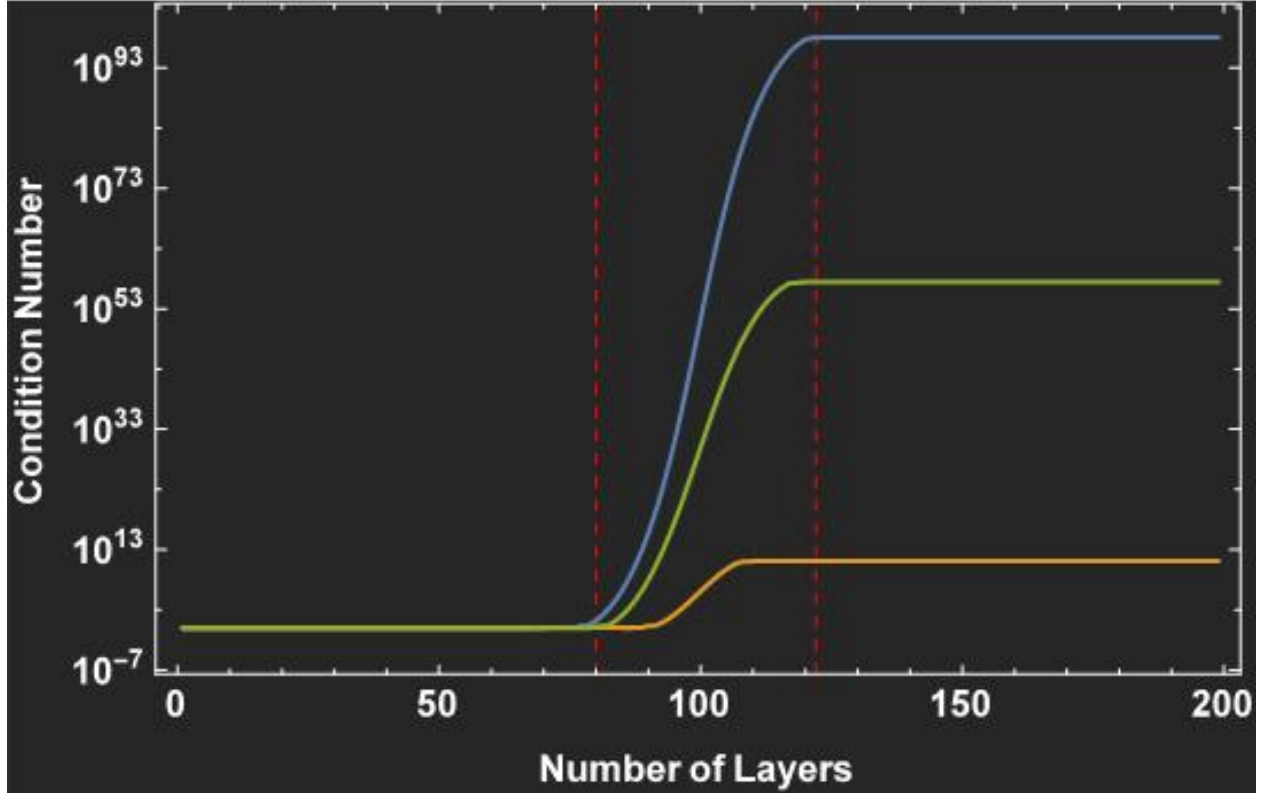
Figure 3.8: Condition number of transfer matrix is plotted on a log scale as we calculate it through the layers. All three curves are for a $10 - fs\ Sech^2$ pulse. The height of the the pulses are $\epsilon = 0.1$, blue curve, $\epsilon = 0.05$, green curve and $\epsilon = 0.01$ for the yellow curve. The red dotted line is a mark for the blue curve calculation. It marks the layer in between which evanescent modes exist.

in the presence of evanescent modes.

3.3.2 S-Matrix Algorithm

The S-matrix algorithm was invented to circumvent the numerical instability problem [68,69]. Subsequently, other algorithms and variants were proposed [70–72]; L. Li presents a comparison of the work in [73]. Here, we discuss a variant of the S-matrix algorithm which is fast and unconditionally stable, i.e. algorithm 2a in [73]. Though we generalise the algorithm to include negative norm modes and inequal number of right and left going modes. As we have seen, that T- Matrix algorithm requires calculation of the inverse of high condition number matrix, and we introduce the S-matrix algorithm to circumvent this. The S-matrix algorithm is such an alternative algorithm. It avoids to calculate the transfer matrix T_N and instead uses intermediate scattering matrices $\mathcal{S}_n$ describing the scattering from layer 0 to layer n, treating layer n as the asymptotic layer. $\mathcal{S}_{n+1}$ is recursively calculated using the propagation matrix I_{n+1} until $\mathcal{S}_N$ is reached.
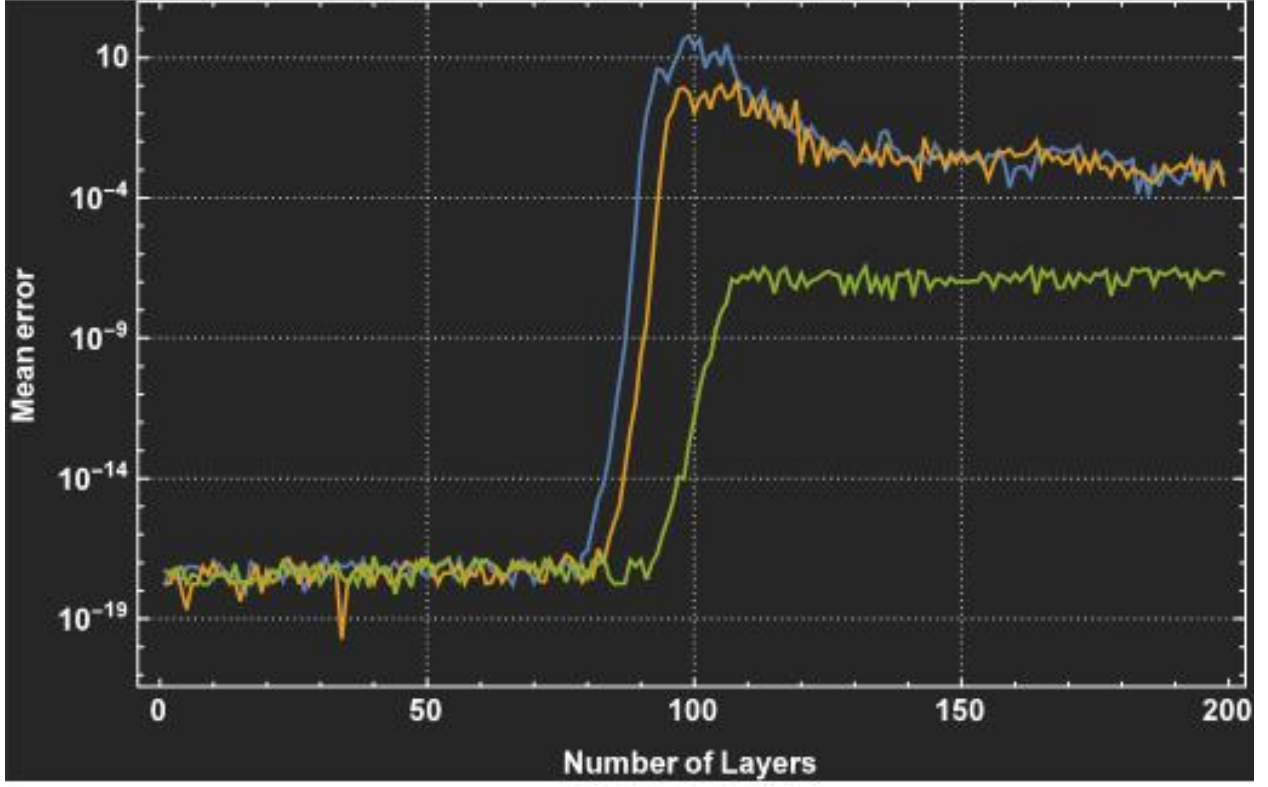
Figure 3.9: Mean error is plotted against number of layers in a log scale. The colour of the curves correspond to the same properties of the pulse as before. The calculation is done in Machine Precision.

From Equation (2.89) we write the equation for $\mathcal{S}_{n+1}$:

$$\mathcal{S}_{n+1}(P_R\sigma_0 + P_L\sigma_{n+1}) = P_L\sigma_0 + P_R\sigma_{n+1}. \tag{3.58}$$

Using (2.89) we express the mode coefficient matrices σ_0 and σ_n as

$$P_R\,\sigma_0 = P_R\,(P_R\,\sigma_0 + P_L\,\sigma_n), \tag{3.59}$$

$$P_L\,\sigma_0 = P_L\,S_n\,(P_R\,\sigma_0 + P_L\,\sigma_n), \tag{3.60}$$

$$P_R\,\sigma_n = P_R\,S_n\,(P_R\,\sigma_0 + P_L\,\sigma_n), \tag{3.61}$$

$$P_L\,\sigma_n = P_L\,(P_R\,\sigma_0 + P_L\,\sigma_n). \tag{3.62}$$

We first insert σ_{n+1} from (3.11) into (3.58). Then we insert the projections (3.59),(3.60),(3.61) and (3.62) in (3.58) to obtain the recursion for S_{n+1}:

$$\mathcal{S}_{n+1} = \big(P_L \, \mathcal{S}_n + P_R \, I_{n+1}(P_R \, \mathcal{S}_n + P_L)\big)$$
$$\big(P_R + P_L \, I_{n+1}(P_R \, \mathcal{S}_n + P_L)\big)^{-1}. \tag{3.63}$$

The recursion starts with $\mathcal{S}_0 = \mathbb{1}$. We apply the recursion until we reach the scattering matrix $\mathcal{S}_N$ relating the asymptotic layers. The numerical instability is avoided here by separating right and left going modes by P_R and P_L, and in turn exponentially growing and decaying complex modes, into different blocks of matrices. This keeps low the condition number of the matrices that are to be inverted, which stabilizes the process, and allows us to work in machine precision. As a result, the duration of the computation of the scattering matrix is drastically reduced.

3.3.3 Riccati matrix equation for the scattering matrix

Although the S-matrix algorithm solves the numerical instability, it still relies on the staircase approximation of the scatterer. We look for an algorithm that is both numerically stable and converges faster than the staircase approximation for an arbitrarily shaped pulse.

We modify the S-matrix method and restate it as a differential equation for the scattering matrix. The scattering matrix $\mathcal{S}$ is expressed as a continuous function of x, $\mathcal{S}(x)$, with $\mathcal{S}_n = \mathcal{S}(x_n)$. Accordingly, we write $\mathcal{S}_{n+1} = \mathcal{S}(x_n + l_n)$. We Taylor-expand the scattering matrix, $\mathcal{S}(x)$:

$$\mathcal{S}(x + \Delta) \approx \mathcal{S}(x) + \Delta \frac{d\mathcal{S}(x)}{dx} \tag{3.64}$$

Similarly, we re-interpret the propagation matrix I, the mode matrix M and the phase matrices κ and Φ as continuous functions. By the definition of the propagation matrix, (3.12), we expand

$$I(x + \Delta) \quad = \quad M^{-1}(x)M(x - \Delta)\Phi(x) \tag{3.65}$$

$$\approx \quad \big(\mathbb{1} - \Delta M^{-1} M'(x)\big)\big(\mathbb{1} + \Delta \, i\kappa(x)\big) \tag{3.66}$$

$$\approx \quad \mathbb{1} + \Delta\big(i\kappa(x) - M^{-1}M'(x)\big), \tag{3.67}$$

Here, the prime denotes the derivative with respect to x. In the limit of $\Delta \to 0$, the propagation matrix $I(x) \to \mathbb{1}$. This reflects the continuity of the fields. We substitute (3.67) and (3.64) into the continuous

version of (3.63) to get a generalized differential equation for the scattering matrix

$$\mathcal{S}'(x) = \Big(P_R - \mathcal{S}(x) P_L \Big) \Big(i\kappa(x) - M^{-1}(x) M'(x) \Big)$$
$$\Big(P_R \, \mathcal{S}(x) + P_L \Big). \tag{3.68}$$

This Riccati equation is an explicit first order coupled differential equation of dimension 8 and with non-constant coefficient matrix $\tau(x) = i\kappa(x) - M^{-1}(x) M'(x)$. It describes the stationary scattering from a scattering potential reaching from $-\infty$ to x and its evolution with x. Note that the only key assumption is that the scattering is stationary. Equation (3.68) can be solved analytically for a few cases including a sech^2-pulse in quadratic dispersion [74].

For most scattering potentials and dispersion relations, the equation has to be solved numerically. The local functions $\kappa(x)$ and $M(x)$ are found from the potential and the dispersion relation, determining the modes present at x. The differential equation can be solved using the simple Euler method. However, numerical methods such as the Runge-Kutta method offer a higher convergence order. This method is therefore stable and converges fast.

For a physical understanding and mathematical simplicity we can break up equation (3.68) into four coupled equations. First we write $\mathcal{S}$ as a block matrix:

$$\mathcal{S} = \begin{pmatrix} \mathcal{S}_{11} & \mathcal{S}_{12} \\ \mathcal{S}_{21} & \mathcal{S}_{22} \end{pmatrix}. \tag{3.69}$$

Here S_{11} and S_{22} block matrices contain all the transmission coefficients and S_{12} and S_{21} contain all the reflection coefficients. Here $\mathcal{S}_{ij}$ is the part of $\mathcal{S}$ that remains after projection to the i, j -subspace, where $1 \leftrightarrow R$ and $2 \leftrightarrow L$. For example, $\mathcal{S}_{11}$ is a p-dimensional square matrix describing the scattering amongst all right moving modes. It is explicitly written as

$$S_{11} = P_R S P_R = P_1 S P_1, \tag{3.70}$$

$$S_{12} = P_R S P_L = P_1 S P_2. \tag{3.71}$$

Next, we find the differential equations of the four blocks $\mathcal{S}_{ij}(x)$:

$$\mathcal{S}'_{12}(x) = \tau_{12}(x) - \mathcal{S}_{12}(x) \tau_{21}(x) \mathcal{S}_{12}(x)$$
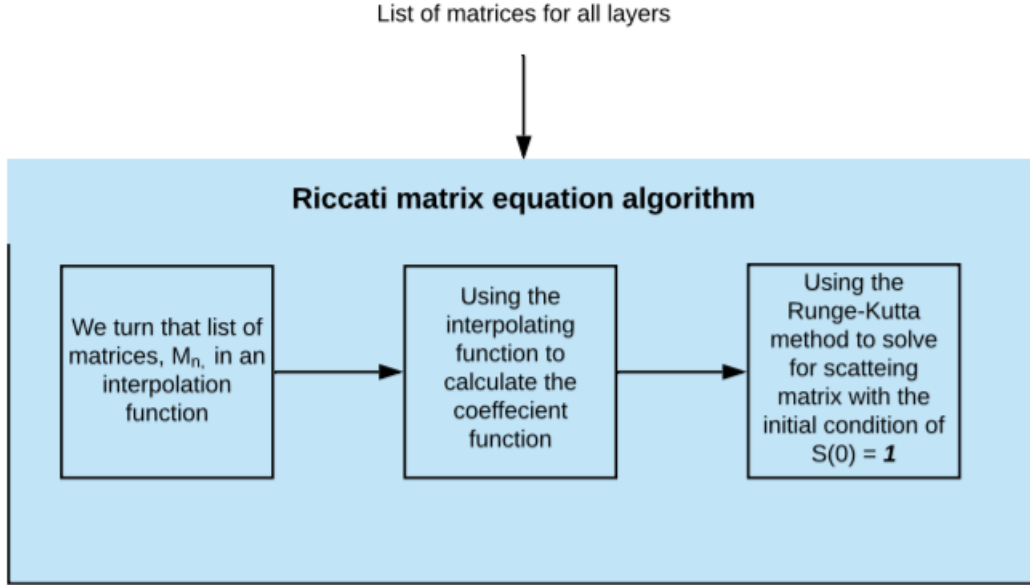$$- \mathcal{S}_{12}(x) \tau_{22}(x) + \tau_{11}(x) \mathcal{S}_{12}(x) \tag{3.72}$$

69

Figure 3.10: The steps involved in calculating the scattering matrix in the Riccati matrix algorithm. The input is a list of matrices, M_n, alongside the layer lengths for all layers in the pulse from the yellow and green steps in Figure 3.6. The coefficient matrix function, $\tau(x)$, is calculated in the intermediary step and then a numerical method, like Runge-Kutta method, is used to solve the differential equation.

$$\mathcal{S}'_{11}(x) = \tau_{11}(x)\mathcal{S}_{11}(x) - \mathcal{S}_{12}(x)\tau_{21}(x)\mathcal{S}_{11}(x) \tag{3.73}$$

$$\mathcal{S}'_{22}(x) = -\mathcal{S}_{22}(x)\tau_{21}(x)\mathcal{S}_{12}(x) - \mathcal{S}_{22}(x)\tau_{22}(x) \tag{3.74}$$

$$\mathcal{S}'_{21}(x) = -\mathcal{S}_{22}(x)\tau_{21}(x)\mathcal{S}_{11}(x) \tag{3.75}$$

One can solve equation (3.72) for S_{12} first as it decouples. The solution is inserted in (3.73) and (3.74) to calculate $\mathcal{S}_{11}$ and $\mathcal{S}_{22}$, which in turn is used in equation (3.75) to calculate $\mathcal{S}_{21}$. Note that this decoupling is independent of the coefficient matrix $\tau(x)$.

Cases where one can derive $\tau(x)$ analytically from the wave equation are an ideal place for the use of this algorithm. In our case, we have no analytical form for $\tau(x)$, we numerically calculate it. Figure 3.10 shows the algorithm as it is applied in our flow.

Properties of scattering matrix

The scattering matrix consists of reflection and transmission coefficients. As we have used orthonormal modes, in many cases the scattering matrix will be unitary. The unitarity of the scattering matrix signifies

the conservation of the energy at a scatterer. It can be expressed as

$$\mathcal{S}g\mathcal{S}^\dagger = g. \tag{3.76}$$

Here g is the 'metric' of the basis set of modes and can be chosen as $g = \mathbb{1}$, i.e. the scattering is passive. g is the dot product of pairs of basis vectors. In the last chapter, in the simple setup toy model, the scattering matrix was a unitary transformation. In some scattering problems, however, the scatterer amplifies or de-amplifies the wave field. For example, this may be caused by a movement of the scatterer and excitation of negative norm modes. The metric in this case is no longer all positive, but g is a diagonal matrix of ± 1. Fields that are amplified correspond to $+1$ and the conjugate fields to -1. The scattering matrices are then 'quasi-unitary' matrices and they represent the Bogoliubov transformations in quantum mechanics. Inserting (3.49) in (3.76), we get

$$(P_L + P_R T)(P_R + P_L T)^{-1} g (P_R + P_L T)^{-1\dagger}(P_L + P_R T)^\dagger = g. \tag{3.77}$$

We can invert and rearrange the equation to get

$$(P_R + P_L T)^\dagger g (P_R + P_L T) = (P_L + P_R T)^\dagger g (P_L + P_R T). \tag{3.78}$$

Noting that $(P_R + P_L T)^\dagger = T^\dagger P_L + P_R$ we write

$$P_R g + T^\dagger P_L g P_L T = P_R g + T^\dagger P_L g P_L T. \tag{3.79}$$

We rearrange the equation to obtain a condition for the transfer matrix $T_N = T(x)$

$$T^\dagger(x)(P_R - P_L)\, g\, T(x) = (P_R - P_L)\, g. \tag{3.80}$$

The scattering matrix relates the asymptotic incoming modes to the asymptotic outgoing modes, whereas the transfer matrix relates the right asymptotic fields to the left asymptotic fields. This difference is what changes the metric in (3.80) from g to $(P_R - P_L)\, g$. The new metric balances the energy flow, if a field is going right then it is either balanced by a conjugate field going right or a field going left and vice versa. The conservation of energy is represented as the quasi unitarity of the transfer matrix. In most problems the transfer matrix is first calculated before the scattering matrix, so Equation (3.80) allows us to check the correctness of the transfer matrix early on in the calculation. One can understand this as the conservation

of norm in space, i.e., the norm is conserved throughout the scattering process. If a positive norm mode is going right then it has to be balanced by a positive norm mode going left or a negative norm mode going right. This balance of norm flow is captured in the Equation (3.80).

The quasi-unitarity of the scattering matrix may be affected by numerical errors. Thus it may indicate numerical errors independently of the actual numerical result.

3.3.4 Differential equation for the scattering matrix

In this section we assess the numerical convergence and stability of the Riccati matrix equation by calculating the global mean error. The numerical calculation is carried out with double precision. We use an explicit single-step method to solve equations (3.72)-(3.75), the explicit fourth order Runge-Kutta method[1] [75] and the sixth order Runge-Kutta method [76]. Other methods of lower order include the Euler, modified Euler and the Haun method [67]. We define the global error δ as the difference between the exact solution and the numerical solution of the differential equation. If the analytic exact solution is not available, the error δ can be approximated by [67]

$$\delta(x, h) = \tilde{\mathcal{S}}(x; \frac{h}{2}) - \mathcal{S}(x) \approx \frac{\tilde{\mathcal{S}}(x; h) - \tilde{\mathcal{S}}(x; \frac{h}{2})}{2^q - 1}. \tag{3.81}$$

$\tilde{\mathcal{S}}(x; h)$ is the numerical solution obtained by the single step method using step size h and q is the order of the numerical method. For the Runge-Kutta method the order is $q = 4$ or $q = 6$ dpending on which numerical process we use. The numerical solution for the Riccati equation has $8^2 = 64$ scattering coefficients. We define a mean error $\bar{\delta}$ as follows:

$$\bar{\delta} = \frac{\|\delta(x, h)\|_1}{64}, \tag{3.82}$$

where $\| \cdot \|_1$ is the $1-$norm of $\delta(x, h)$. In our case we have 8 modes in each layer and hence 64 scattering coefficients. We choose 1-fs, 10-fs and 20-fs sech^2-shaped pulses. We use a constant step size and vary the number of steps across the pulse length while calculating the scattering matrix. In Figure 3.11 the global error is shown as a function of the number of steps used. The figure shows that the mean error decreases as h^p, where p is the order of the method. As the error approaches $10^{-12} - 10^{-13}$, we see that it deviates from the h^{-p} curve, because the error reaches machine precision. This effect is most clearly seen for the brown curve, i.e the 1 fs pulse solution solved by the sixth order Runge-Kutta method. Here, as the error falls below 10^{-13}, increasing the number of steps does not reduce the global error. Thus the number of steps may be chosen for the required accuracy level for the solution. The correctness of the solution is tested by verifying the quasi-unitarity (3.76) of the scattering matrix, i.e. calculating $\mathcal{S}^\dagger g \mathcal{S}$ and comparing to g.
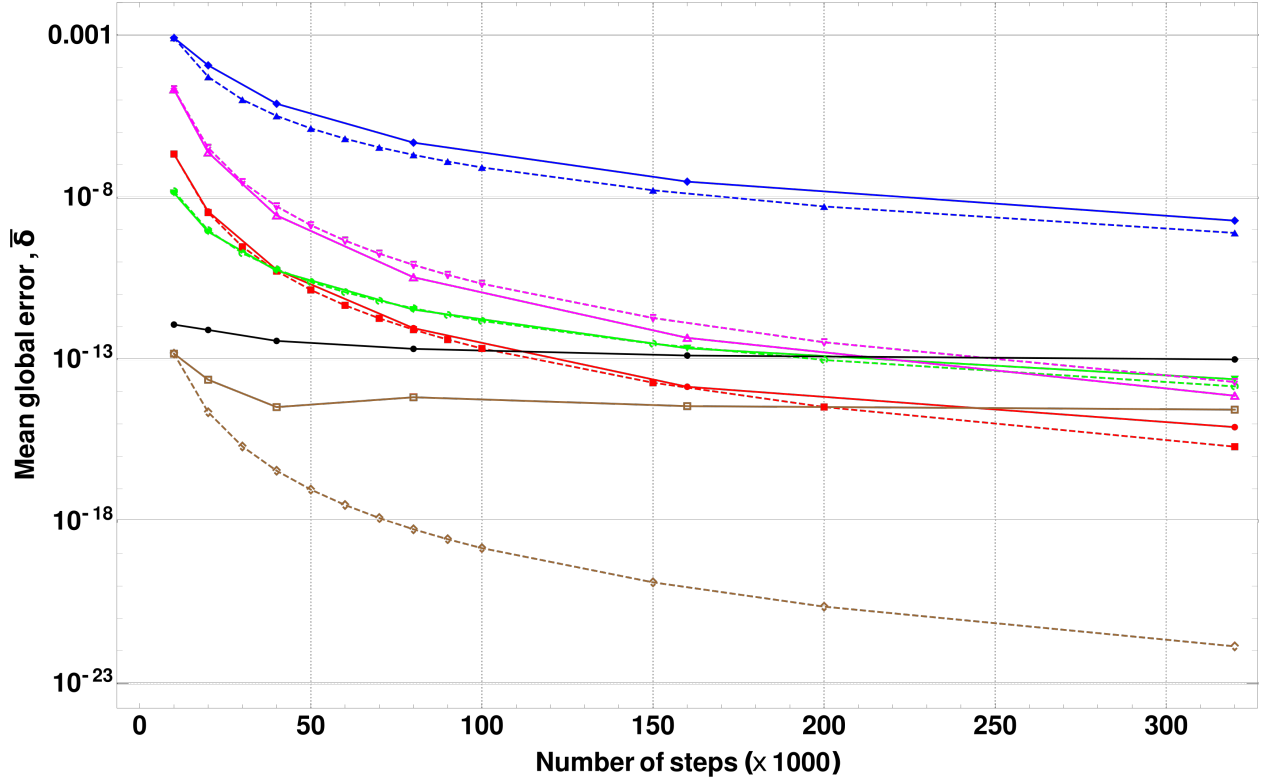
Figure 3.11: Mean global error $\bar{\delta}$ in solving the Riccati differential equation numerically as we increase the number of steps the explicit Runge-Kutta (RK) method uses. The blue and the green curve is the error for a classical fourth order RK method for $10fs$ and 1 fs pulses, respectively. The blue and green dashed lines shows the scaling of N^{-4}. Pink, red and brown curves show the error for 20, 10 and 1 fs pulses, respectively, solved by a 6th order RK method. The dashed curve shows the scaling of N^{-6}. The black curve shows the correctness of the solution for a $10fs$ pulse calculated by a sixth order RK method.

Similar to (3.81) and (3.82), we can define a mean deviation. The black curve in Figure 3.11 shows how the mean deviation varies as we increase the number of steps. It stays around a mean deviation on the order of $10^{-11} - 10^{-12}$. The mean error here is limited by the error in inverting the scattering matrix in machine precision. The reasons for this is as discussed in the precision loss section. Any numerical computation will have round off errors and as the condition number of the scattering matrix is more than 1 the errors will be more than just round off errors. The small size of the deviation confirms that quasi-unitarity is fulfilled in the scattering matrix solution of the differential equation. This also gives us a limit on the accuracy of our solutions to follow when done in machine precision.

Remarks

We have shown a new concise formula connecting T-matrix to S-matrix and have generalised both the T and S-matrix algorithms to describe scattering from a moving scatterer. The numerical stability of the S-matrix algorithm is demonstrated and we have successfully calculated a scattering matrix through the new Riccati

matrix equation. We have demonstrated the fast convergence of the solutions through the Runge-Kutta method. We demonstrated the numerical stability of the S-matrix algorithm compared to the T-matrix algorithm, which we formulated in a compact way (Equation (3.49)). We presented a novel differential equation for the scattering matrix.

Here we have all three possible ways to calculate the scattering matrix. Depending on the scattering problem we can choose the appropriate algorithm. For a step, the T-matrix algorithm is best suited as it is quite stable. For a top-hat pulse or for a pulse which is not smooth and has layers, can be solved by the S-matrix algorithm. For a smooth pulse we can solve it either by the S-matrix algorithm or by the Riccati matrix equation. We have also shown that the staircase approximation does lead to convergence as we increase the number of steps.

Chapter 4

Numerical Results

4.1 Numerical results in Literature

Many scattering simulations have been solved and presented in optics but only a handful in optical analogue horizon scattering. Scattering among positive norm modes, i.e. the blue and red shift and resonant radiation from an optical pulse, has been studied in detail, both experimentally and numerically [39,46]. However, the scattering to negative modes with a focus on Hawking modes has not been produced numerically in detail. The first numerical study was done in 1996 by Jacobson et all [77]. Here they wanted to investigate the effect that nonlinear dispersion plays in the spectrum of the Hawking mode in an analogue fluid system. They modeled the horizon as a tanh velocity profile. The dispersion relation was modeled as one of vacuum for lower frequencies and then a deviation of second order for higher frequencies. This model was studied in detail in 2009 by Parentani et all [78]. Here they concluded that the Hawking flux depends on the curvature of the velocity profile at the point where the horizon is formed, the asymptotic regions of the scattering and the curvature of the transition from the ramp to the asymptotic layers. Though this numerical study was done for fluids and for a much simpler dispersion relation we shall show the same features in our results. In optics we have the flux produced from a step [52, 79] and for a few optical soliton pulses [80]. The results for the optical pulses were produced by using integral methods in the Fourier space developed by Robertson [81,82]. However, these methods were not numerically optimised and resulted in quite an increase of computation time when complex modes were present, as stated in the papers, and no methods were available for efficiently producing numerical results for various scattering profiles. This is why we see that results were either produced via WKB or some other approximations for smooth curves or if a robust method was used it was computationally heavy and restricted us to very simple scattering profiles like a step. Even

in the 2016 paper [80] with the numerical results for the optical pulse we see the flux for only one pulse of 2 fs and the dispersion diagram does not include all the branches.

In this chapter we use the methods discussed in the previous chapter to produce fluxes for various steps, ramps and pulses for a full Sellmeier dispersion relation which includes all eight branches.

4.2   Results

Here we will show and discuss the scattering from various scattering surfaces. The flux of photons per time is evaluated by summing over the absolute square of the partner scattering coefficients as discussed in the previous chapter. We have 5 positive and 3 negative modes and they are arranged in an ascending order according to the real part of their frequency. The photon flux for a positive mode is the sum of the absolute square of the scattering elements of all the negative modes for that positive mode, and similarly for the flux of a negative mode i,e

$$I_{\alpha \in P/N}^{\omega} = \sum_{\alpha' \in N/P} |S_{\alpha \alpha'}^{\omega}|^2. \tag{4.1}$$

This is dimensionless measure of the photon flux. We calculate the flux for different moving frequencies, ω. We vary the frequency from $0.5\omega_{min}$ to $1.1\omega_{max}$. Here $\omega_{min/max}$ are as described in Section 3.2. This captures all the possible dynamics, i.e. all 5 cases. There are two parameters that describe the top hat pulse, i.e. the pulse length, T_p, and the height of the pulse, intensity of the pulse, denoted by ϵ. This is a quantitative way to show how much the dispersion relation is affected by the pulse. The relation between ϵ and the change in refractive index is shown in Equation (2.78).

We start by showing the flux of all eighth modes for a step of height, $\epsilon = 4 \times 10^{(-3)}$. This corresponds to a refractive index increase of, $\delta n \approx 1.5 \times 10^{(-3)}$. The step is travelling towards the right with a speed of $v = 0.68158 \times c$. The setup is shown in Figure 4.1. We assume without loss of generality that the step interface is at $x = 0$.

We choose this step height so that we can see all 5 scenarios. We also name our modes so that we can refer to them easily. From the Figure 2.1 we see that there are 8 branches in total from the top to bottom we call these branches, upper upper (UU), upper (U), optical (O), lower (L), negative lower (NL), negative optical (NO), negative upper (NU) and negative upper upper(NUU) branch. The pulse velocity and the frequency we choose gives no solutions in the upper upper(UU) or negative upper upper(NUU) branches. In descending order according to the lab frequency, the possible modes are upper (U), upper optical (UO), middle optical (MO), optical (O), lower (L), negative lower (NL), negative optical (NO) and negative upper (NU) mode. Here we find 3 modes in the positive optical (O) branch, though as we have seen in section 3.2

76

that two of these modes can turn complex. MO mode is the only one that travels towards the right in the moving frame. Every other mode travels towards the left. Figure 4.2 shows the flux for all eight modes. The dashed curves are flux for negative norm modes and blue, pink and black curves are the optical modes.

- Before the first vertical red dotted line is scenario 5 where both regions, inside the step and outside the step, have 6 real modes and 2 complex modes. We see 6 curves before the first red dotted line, as MO and O modes do not exist in that scenario.

- In between the first red and first blue dotted line we have scenario 4 where we have 8 real modes inside the step, $x < 0$, and 6 real modes outside the step, $x > 0$. Here the step is an analogue white hole horizon. The inside of the step, $x < 0$, is the outside of the white hole event horizon, as there are modes that can travel both ways. The outside of the step, $x > 0$, is the inside of the event horizon as modes can only travel towards the step. We can see that in this case the flux increases for the escaping mode. The negative mode partner is the NO mode and is correlated closely with the optical(O) mode .

- In between the first blue dashed vertical line and the second red dashed vertical line we have Scenario 3 where we have all real solutions in both the regions. Here the flux generated is not due to horizon physics. It is generated just because of dispersion and the mixing of negative and positive norm modes.

- In between the second red dashed line and second blue line we have Scenario 2. Here the step is an analogue black hole event horizon. $x < 0$ is the inside of the event horizon as modes can travel only one way, i.e. away from the step, $x > 0$ is the outside of the event horizon as modes can travel both way and the only escaping mode is the MO mode, the black curve. Outside the step, $x > 0$, there are 8 real modes, 1 escaping the step and the other 7 incoming towards the step. Inside the step we have 6 real modes and all of them are travelling away from the step. Here, as in scenario 4, we can see the escape mode peaking and the negative optical norm mode, black dotted curve, being closely correlated with the escaping mode.

- After the last blue dotted line we are in Scenario 1 with 2 complex modes in both regions. The MO mode does not exist and we only get the O mode. The flux decreases as we go away from the horizon cases.

This is a left step as the step rises to the left. The flux of a right step is just calculated by the inverse of the scattering matrix for the left step, as the in modes become out and vice versa when we reverse the side of the step. The flux for the right step is shown in Figure 4.4 .
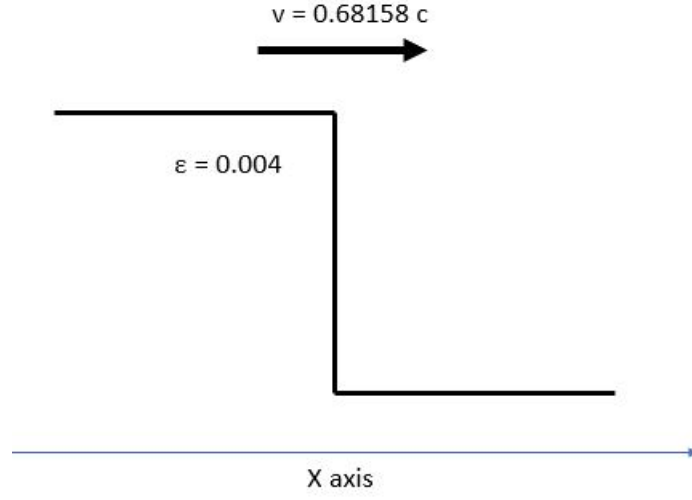
77

Figure 4.1: Shows the step used as a scatterer. ϵ is the step height and v is the speed of the step.
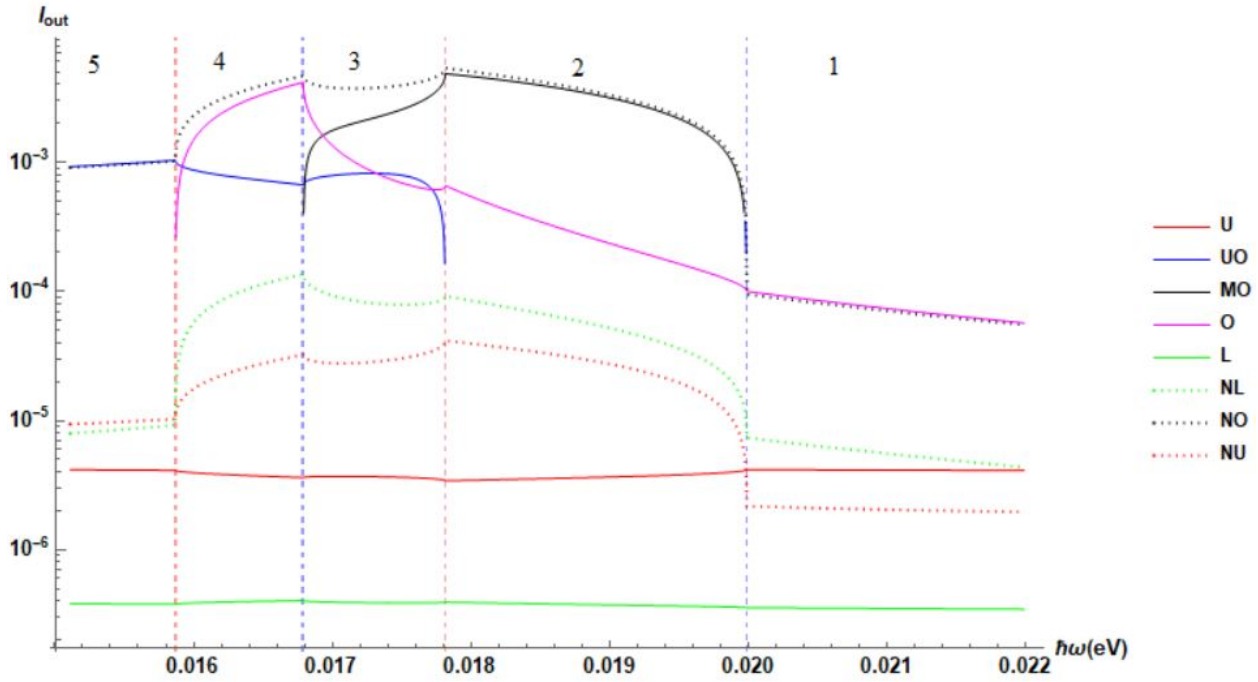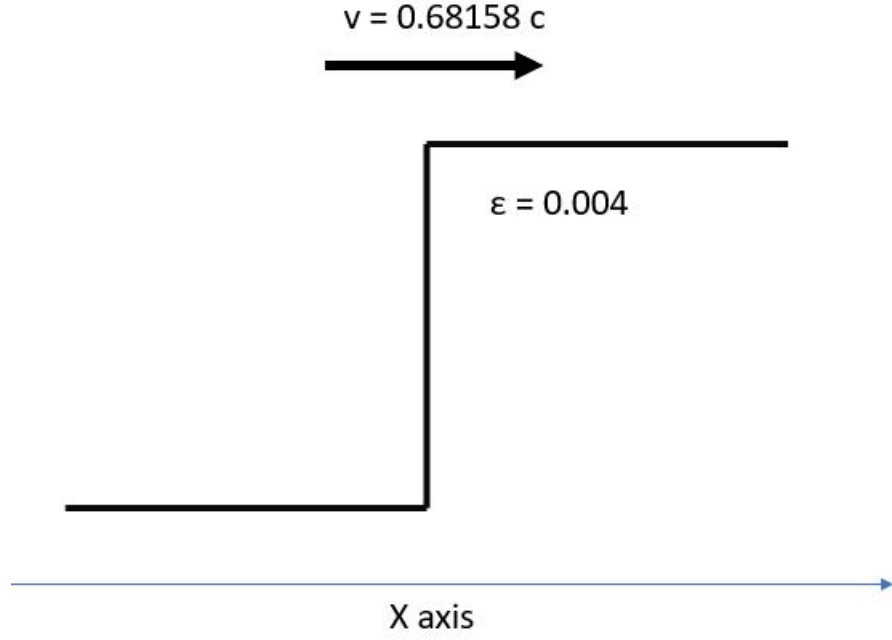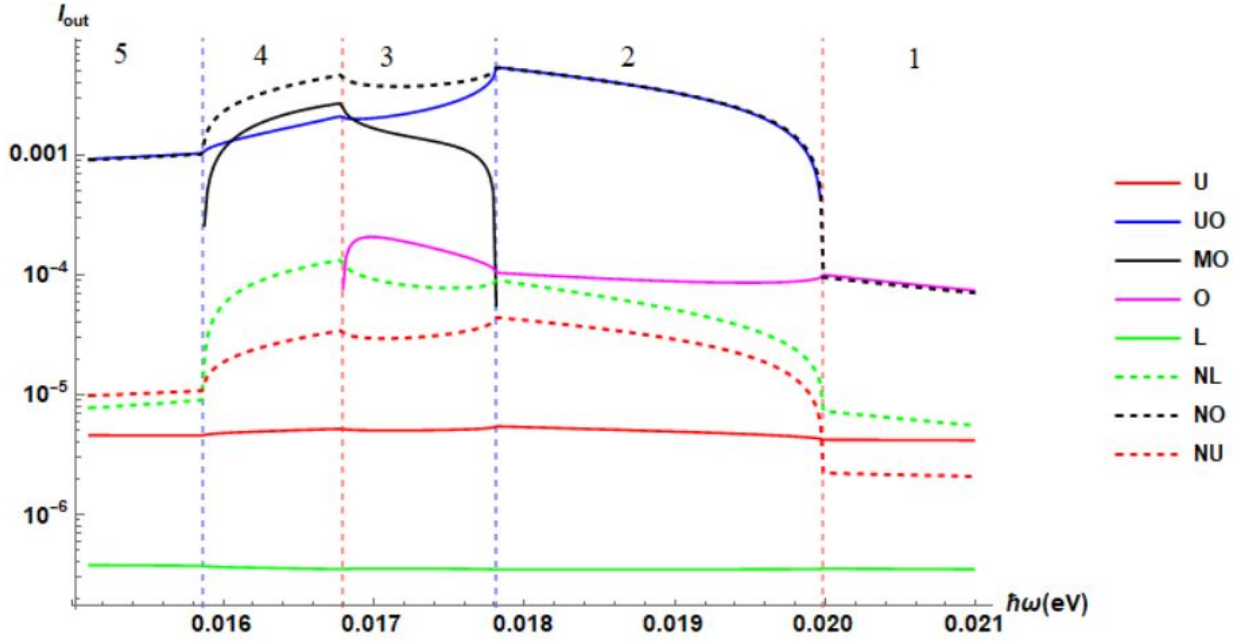

Figure 4.2: The flux for all eight modes for a left step of height of $\epsilon = 4 \times 10^{-3}$. The step is travelling at a speed of $v = 0.681588 \times c$, group velocity for a pulse with central wavelength of 800 nm. The vertical blue dotted lines are the $\hbar\omega_{\text{min}}$ and $\hbar\omega_{\text{max}}$, i.e are the turning points of the optical branch of the medium. The red dotted lines are $\hbar\omega'_{\text{min}}$ and $\hbar\omega'_{\text{max}}$ are the turning points of the optical branch in the step.

Figure 4.3: Shows the step used as a scatterer. ϵ is the step height and v is the speed of the step.

Figure 4.4: The flux for all eight modes for a right step of height of $\epsilon = 4 \times 10^{-3}$. The step is travelling at a speed of $v = 0.681588 \times c$, group velocity for a pulse with central wavelength of 800 nm. The vertical blue dotted lines are the $\hbar\omega_{\text{min}}$ and $\hbar\omega_{\text{max}}$, i.e are the turning points of the optical branch of the medium. The red dotted lines are $\hbar\omega'_{\text{min}}$ and $\hbar\omega'_{\text{max}}$ are the turning points of the optical branch in the step.

- Scenario 5 (before the first red dotted vertical line) In this region we approximately similar flux to that from a left step.

- Scenario 4 (in between the first red dotted and first blue vertical line). Here we have 8 real modes inside the step and 2 complex modes outside of the step. The MO mode exists inside the step and the UO mode is one of the outgoing modes outside the step. The step is analogous to a black hole event horizon where the outside of the horizon is $x > 0$, inside the step, and the inside of the horizon is $x < 0$, outside of the step. The escaping mode here is the MO mode. Here you can see that the shape of the black curve in Figure 4.4 is the inverse of the shape of the black curve in 4.2. Similarly the shape of the UO mode, blue curve in Figure 4.4, is inversion of the shape of O mode, pink curve in Figure 4.2.

- Scenario 3 is the situation where there is no horizon physics and we get 8 real solutions.

- Scenario 2 - Here we have 8 real solutions outside the step, $x < 0$, and 2 complex solutions inside the pulse, $x > 0$. The step is a white hole horizon where the outside of the horizon is outside the step, $x < 0$ and the inside of the horizon is inside the step, $x > 0$. The UO mode is one of outgoing modes from the white hole horizon in $x < 0$ and its flux is maximised in this scenario.

- Scenario 1 - It is similar to 4.2.

We see that the left step is better suited as it depicts the black hole event horizon case for a longer window in the frequency regime. The way flux depends on the step height is depicted in Figure 4.5 .

- Here we have plotted the flux of the escaping mode, MO, and negative optical mode, NO, at $\hbar\omega = 0.018$ eV. It shows that as refractive index increases so does the flux of the escaping mode. The kink occurs when the refractive index is high enough to make complex modes come into existence inside the step. The horizon forms.

- As we increase the step height we see that the MO mode's flux rises less steeply than that of the O mode and the NO mode gets more correlated with the O mode.

- As the height increases the mode's wavelength and frequency change. The NO and O mode's lab wavenumber and frequency decrease and and their fluxes become more similar to each other and hence is phase-matched more easily. The MO mode is at the right of the step and its wavenumber and frequency do not change with the step height.

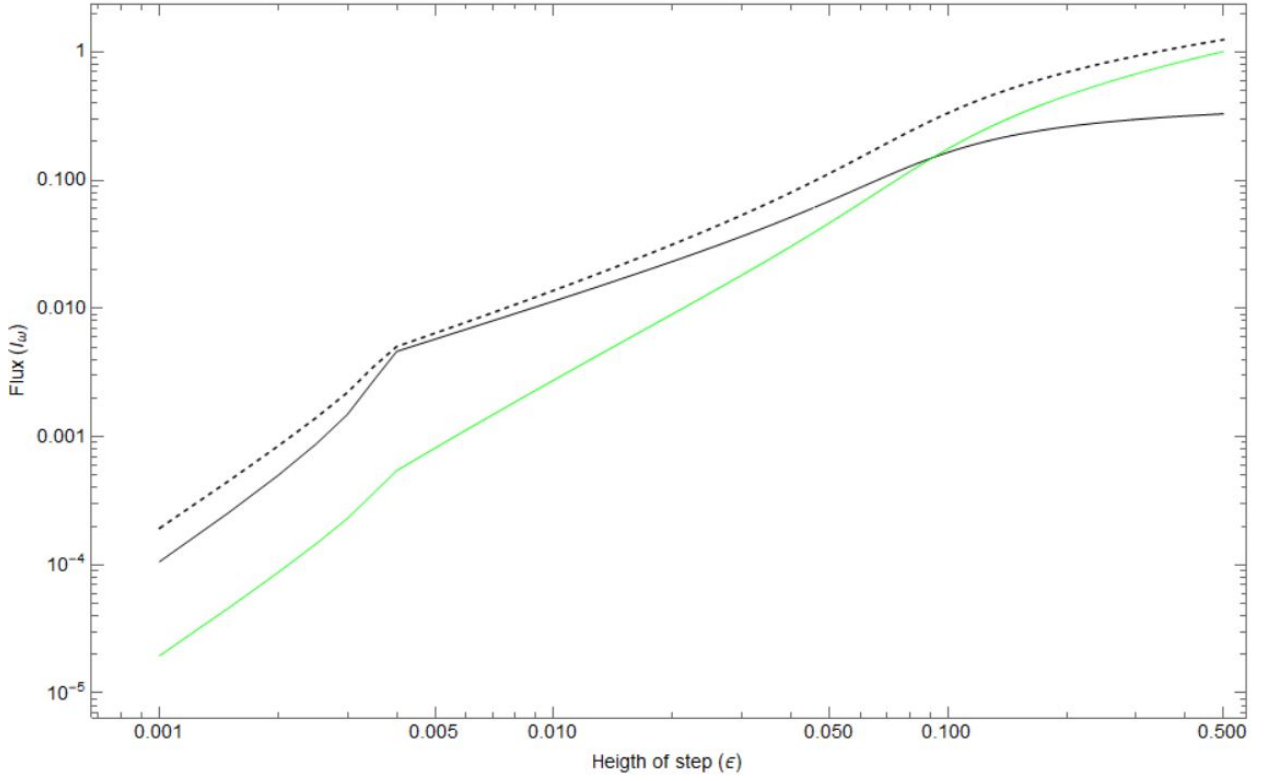- This kink in the MO flux will become more amplified in the next section when we study ramps.

Figure 4.5: This Log-Log plot of the flux of the MO (black curve), NO (black dotted curve) and O (green curve) verses the increase in refractive index for the left step. The frequency is $\hbar\omega = 0.018$ eV.

Here we have shown the result of scattering from a step and how the flux changes with height of the step. Results of the step scattering have been discussed in detail in [83].

4.2.1 Ramp as a scatterer

One of the things which have not been studied in the literature is how the flux is affected if we have a smooth step as a scatterer. With our new algorithms we can study the scattering from smooth surfaces. We model the smooth step, ramp, as an exponential function. This is shown in Figure 4.6.
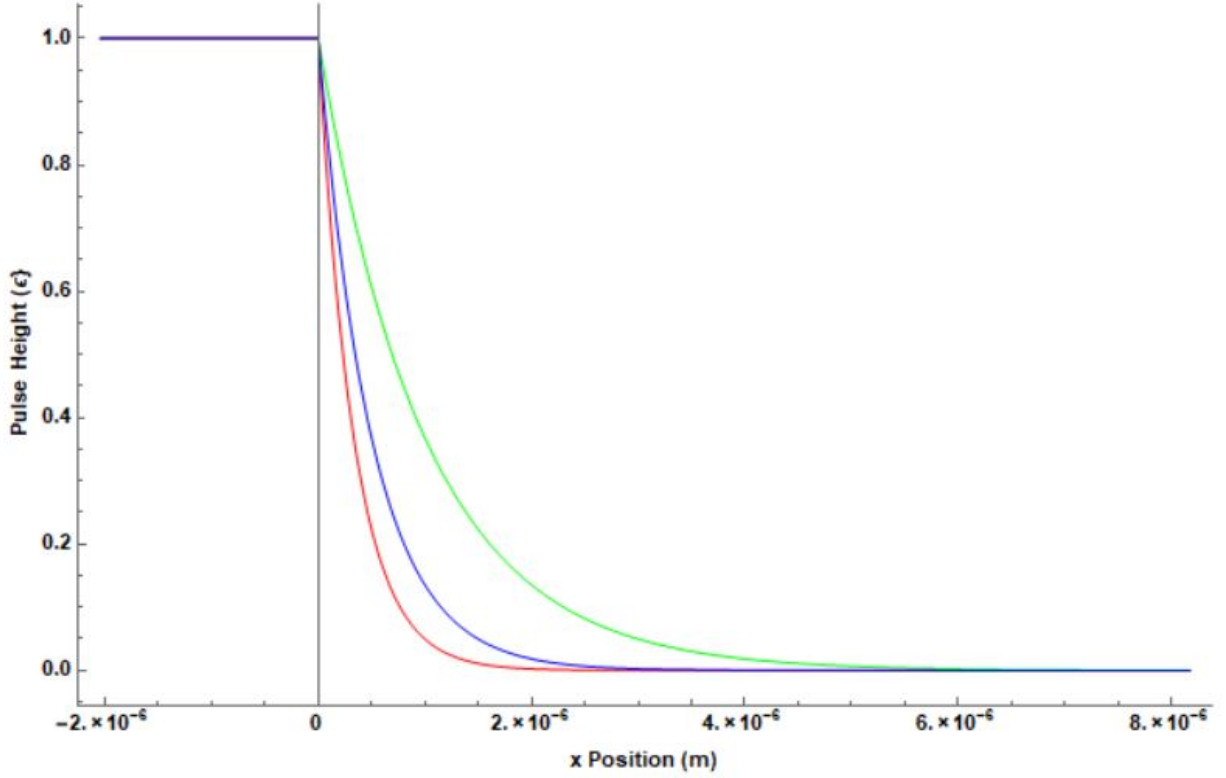
Figure 4.6: Smooth step profiles. They all have same step height , $\epsilon = 4 \times 10^{-3}$, for $x > 0$ the pulse profile is described by $\epsilon_{max} \exp[-px]$, where p is different for all three curves, green curve has $p = 10^6 \mathrm{m}^{-1}$, blue has $p = 2 \times 10^6 \mathrm{m}^{-1}$ and red has $p = 3 \times 10^6 \mathrm{m}^{-1}$

We model a smooth step as an exponential function , $\epsilon(x) = \epsilon_{max} \exp[-px]$, where p is a quantitative measure of how quickly the step rises to its height. The transition from the ramp to the asymptotic region is a sharp one at the top of the ramp and a smooth exponential one at the bottom of the ramp. To solve the scattering problem we employ the staircase approximation. As the exponential function is infinitely long we start to discretize the ramp when the height is sufficient for the off diagonals of the scattering matrix to become larger than $\approx 10^{-15}$. We plot the mode flux of the green ramp in Figure 4.6. The ramp with the least gradient in Figure 4.6. The flux is shown in Figure 4.7. Here the fluxes of all 8 modes are plotted. The first big difference between the step and the ramp is the magnitude of the flux. The peak of the flux drops from around 10^{-2} to 10^{-5}. The second big difference is that the kinks disappear in our ramp's flux curves as compared to the step's flux. The shape of the MO mode, the escaping mode in the black hole event horizon analogue case, maintains its shape. The shapes of the UO curve and O curves are also somewhat preserved though it is changed much more than the MO curve. Every mode's flux is radically decreased except for that of the L mode. This is because the scattering in the L mode is not affected in this frequency window. In a ramp, scattering is 'softened' because the modes do not change as drastically as in the case of a

discontinuous step. Modes change slowly throughout the ramp and this slow change in matching conditions across the layers makes the scattering coefficients small.
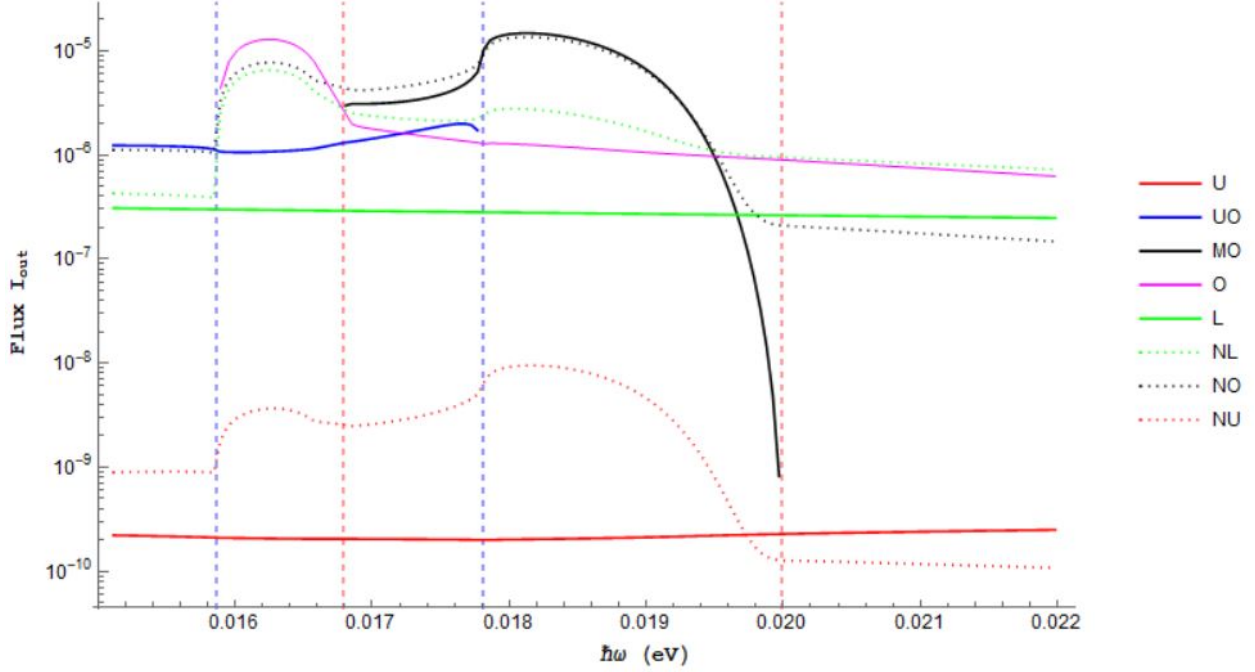

Figure 4.7: Flux of 8 modes plotted in a Log curve for the green ramp of height $\epsilon = 4 \times 10^{-3}$ and $p = 10^6$ m^{-1} traveling at a speed of $v = 0.681588c$. The vertical blue dotted lines are the $\hbar\omega_{\min}$ and $\hbar\omega_{\max}$, i.e are the turning points of the optical branch of the medium. The red dotted lines are $\hbar\omega'_{\min}$ and $\hbar\omega'_{\max}$ are the turning points of the optical branch in the step.

As we increase the gradient of the ramp, make it steeper, we expect the flux to increase to that of a step. We show this by focusing on the flux of the MO mode in the black hole event horizon regime. We plot the flux of the MO mode for $\hbar\omega = 0.018$ eV for different gradients. The flux is shown in Figure 4.8. We see that as we increase the gradient of the ramp, p, the flux increases. The flux saturates to that of a step as the ramp becomes more steep. This is a good result as it confirms what we expect and it gives us more trust in our calculations apart from the correctness check we do by calculating $\mathcal{S}g\mathcal{S}^\dagger = g$.

For the next plot we keep the gradient constant and change the height of the ramp and plot the modes' fluxes. We plot it for a temporal width of $T_0 = 5$ fs. The gradient is calculated as $p = \frac{1}{T_0 \times V_g}$. Figure 4.9 shows the flux.

- There is a sudden jump in the flux right after the horizon is formed. This jump in the flux is in the escaping mode, MO, which is correlated with NO mode and a bit with NL and NU mode. This jump is due to the horizon physics.

- As we increase the height of the ramp further flux of the MO mode drops and flux of the O mode
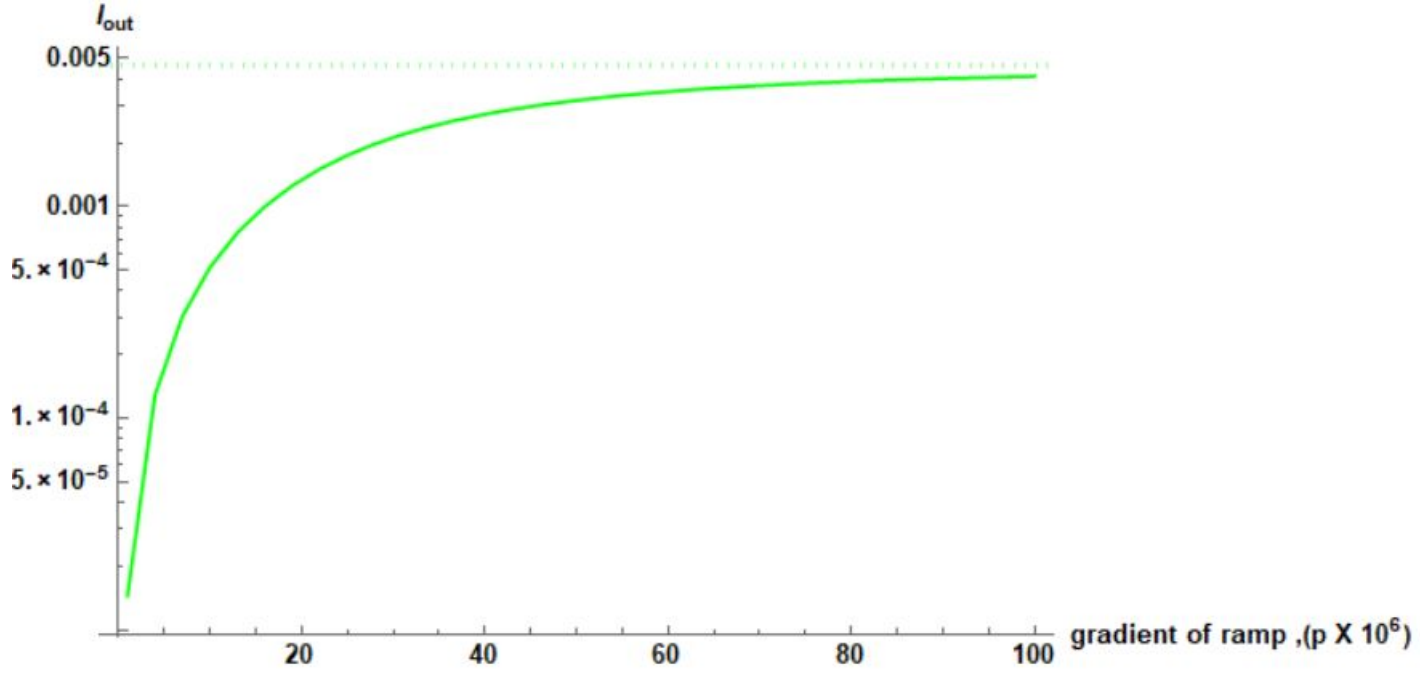
Figure 4.8: Flux of the MO mode at frequency, $\hbar\omega = 0.018$ eV for a ramp of height $\epsilon = 4 \times 10^{(-3)}$, is plotted against the gradient of the ramp, p. The green dotted line is the flux for a step of the same height.
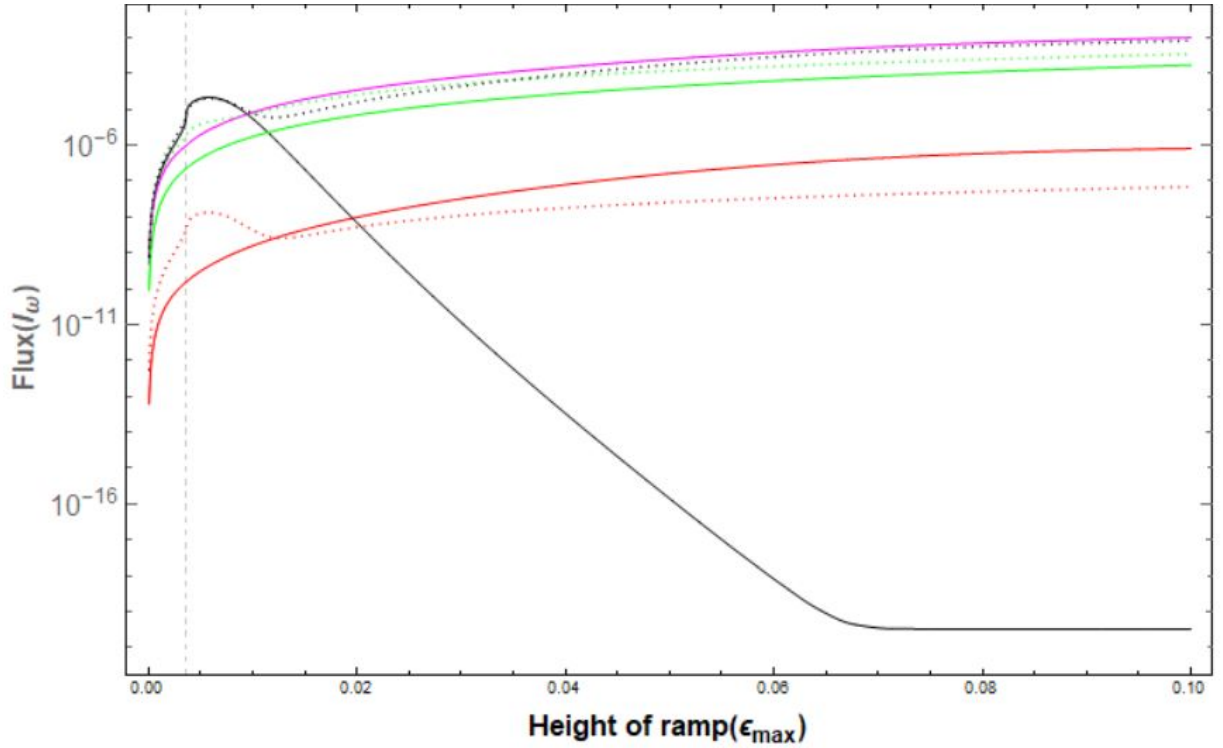

Figure 4.9: Flux of all 8 modes against the ramp height for an exponential ramp of temporal width of 5 fs, $p = 9.8 \times 10^5$. The black is for MO mode, red is for U, pink is for O, green is for L. The dashed lines are for negative norm modes, red is for NU, green is for NL and black is for NO. The gray dashed line on the x axis is the height at which the horizon is formed.
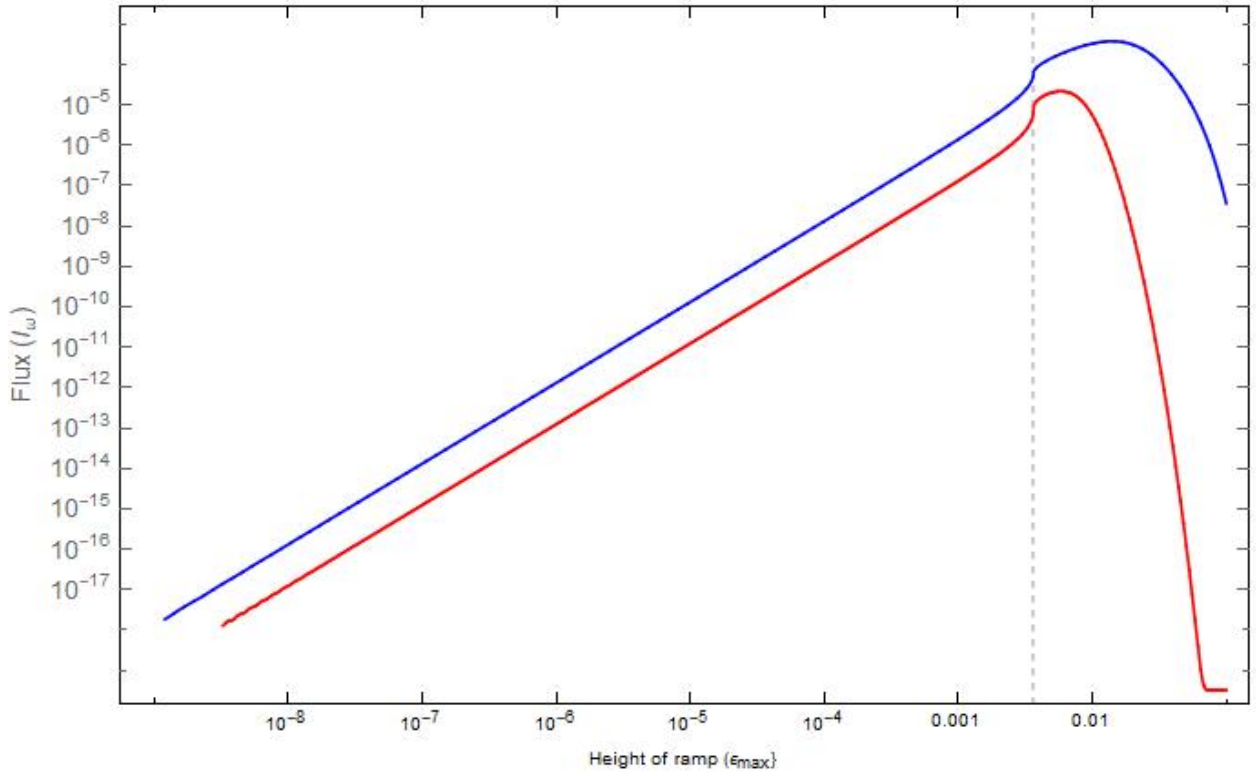
Figure 4.10: Flux of the MO mode against the height of the ramp for two gradients, red curve is for 5 fs ramp and blue is for 1.5 fs ramp. The dashed grey line is at the step height where the horizon is formed.

rises along with that of the L mode. The NO mode is correlated more with the O and L mode. This is similar to what we see for the step in Figure 4.5. The drop in the MO mode is significant and it becomes numerically zero to machine precision for higher ramp heights.

- The MO mode is the only right going mode and as we increase the step height its lab frequency and wavenumber mismatches with the modes on the other side of the ramp. Similarly, the complex mode's imaginary part grows and thus diminishes rapidly, less of the MO mode is tunnelled through the ramp and scatters less into other modes.

This decrease in the MO mode can be studied further. It is an effect due to the dispersion relation and is not due to the horizon physics. We plot the flux of the escaping mode, MO, for a steeper ramp in Figure 4.10.

- Both the curves have similar shapes. The flux for the steeper ramp has higher flux for the same height of the ramp. The blue curve shows the horizon effect for a longer window. The complex waves have to travel less of a distance and hence are damped much less, which results in more scattering of the MO mode.

- Due to the steep fall in the MO flux as we increase the step height, we encounter scenarios with higher flux for a ramp with a lower gradient and lower height. For example a ramp of height 0.004 with gradient of $p = 9.8 \times 10^5$ has a higher flux compared to a ramp of height of 0.1 with gradient of $p = 3.2 \times 10^6$.

Temperature of the Radiation

From the flux we can calculate the brightness temperature of this radiation. We assume that the flux is part of a thermal radiation where the flux density is related to the temperature as

$$I_\omega^{\text{Out}} = \frac{1}{e^{\frac{\hbar\omega}{k_B T_\omega}} - 1}. \tag{4.2}$$

Here k_B is the Boltzmann constant and T_ω is the temperature for that frequency. We can rearrange Equation (4.2) to make temperature the subject of the equation and write

$$k_B T_\omega = \frac{\hbar\omega}{\ln\left(\frac{1}{I_\omega^{\text{Out}}} + 1\right)}. \tag{4.3}$$

We plot how the temperature changes for different ramp heights as we change the gradient. We plot it for 6 different step heights. The temperature is plotted in Figure 4.11.

- All the curves reach the temperature of the step, of the same height as the ramp, as the steepness of the the ramp is increased.

- Ramps with lower heights can have higher temperature for a certain gradient. A prominent example is the green curve higher than all the curves at $p = 10^6$. This is true for all the curves. This is why we see the crossing of the curves in the figure. The horizon is at a point where the real modes turn complex inside the ramp, this happens at $\epsilon = 0.0036$ for frequency $\hbar\omega = 0.018$ eV.

- This result gives us an insight on how the flux can be maximised for a pulse. We can maximise the temperature of the flux with less intense pulses if the length of the pulse can be manipulated.
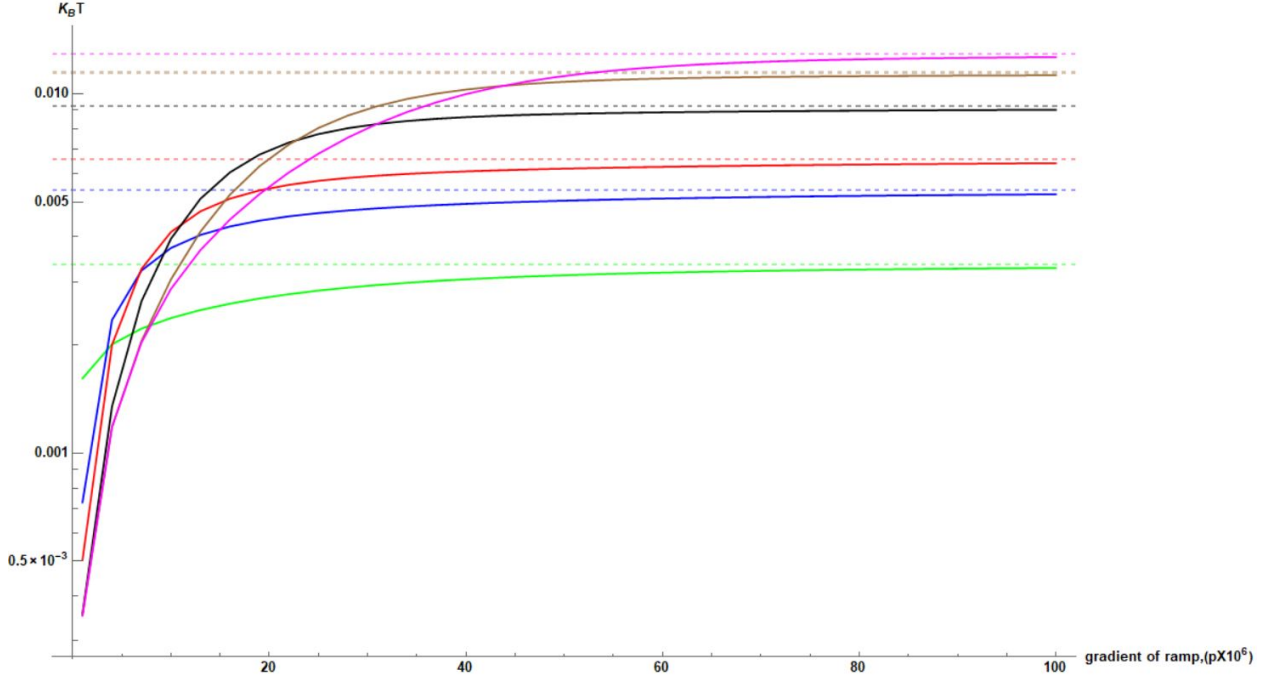
86

Figure 4.11: Log plot of temperature of the MO mode against the gradient of the ramp for 6 different ramp heights. The frequency is $\hbar\omega = 0.018$ eV. Green curve is for ramp height, $\epsilon = 0.004$, blue curve is for $\epsilon = 0.03$, red curve is for $\epsilon = 0.05$, black curve is for $\epsilon = 0.1$, brown curve is for $\epsilon = 0.2$ and pink curve is for $\epsilon = 0.5$. The dotted lines are the corresponding temperature for the step heights.

^{2} ramp

Here we investigate the role of the curvature of the scatterer in the emission process along with the effect of the dispersion relation. We model the ramp now with as half a ^{2} pulse. The equation of the ramp is

$$\epsilon(x) = \begin{cases} \epsilon_{\text{max}}, & \text{for } x \leq 0 \\ \epsilon_{\text{max}} \, ^2\left(\frac{x}{T_0 V_g}\right), & \text{for } 0 < x \end{cases} \qquad (4.4)$$

The gradient of the ramp, p, is $p = \frac{1}{T_0 V_g}$. As before, we can see how the temperature depends on the gradient of the ramp. Figure 4.13 shows the temperature as we vary the temporal width of the ramp for various heights of the ramp for the frequency, $\hbar\omega = 0.018$ eV. The temperature is for the escaping mode, MO.

- The temperature drops as we increase the temporal width. For a 5 fs ramp the temperature drops to very low value. This shows the temperature of a ramp is very sensitive to temporal width.

- The way the temperature falls with respect to temporal width depends on the height of the pulse and the curvature at the turning point. We see that we might get lower temperature for 5 fs ramp for a
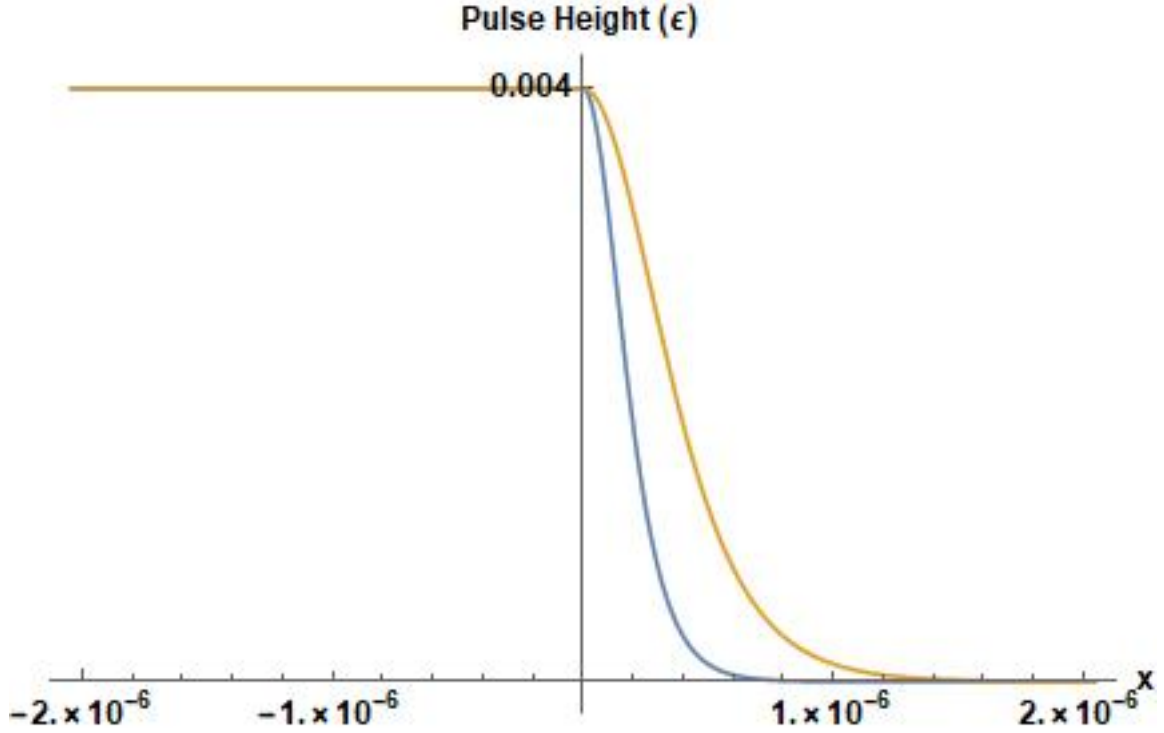
87

Figure 4.12: ^{2} ramps depicted. The yellow curve is for $T_0 = 2$ fs and blue curve is for $T_0 = 1$ fs. Group velocity, $V_g = 0.68158c$, speed of a pulse centred at $\lambda = 800$ nm. The height of the ramp, $\epsilon_{max} = 0.004$.

higher ramp than a lower ramp.

- This behaviour is similar to Figure 4.9. The Flux of the MO mode as we increase height of the ramp drops down and this is what we see here as well.

Sigmoid Ramp

We model the ramp as a sigmoid curve. It is defined as

$$\epsilon(x) = \epsilon_{max}\frac{1}{1 + e^{px}}. \tag{4.5}$$

Here p is a measure of the gradient of the curve. The curves are plotted in Figure 4.14.

Similar to Figure 4.11, we plot the temperature of the MO mode versus the gradient of the ramp. Figure 4.15 shows the temperature of the MO mode versus ϵ. The lowest gradient for which the temperature is plotted is $p = 5 \times 10^6$. We could not go to lower gradient as that presented a computational challenge. As we decrease the gradient, p, the length of the ramp increases and we require larger number of steps to compute the scattering matrix, increasing the computational time. Hence, the crossing of the curves are not recorded here as we saw them in Figures 4.11 and 4.13.
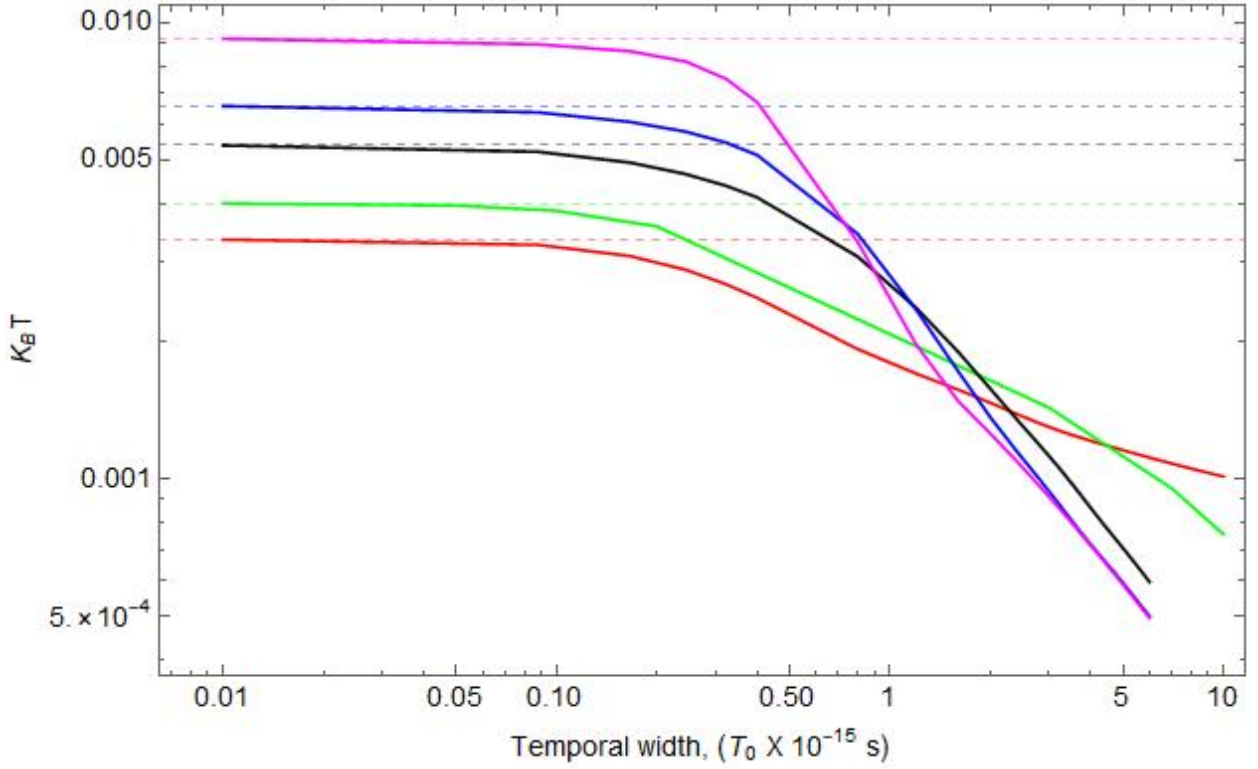
88

Figure 4.13: The temperature of the MO mode is plotted for various ramps of different heights as we vary the temporal width of the ramp in a log-log graph. The red curve is for $\epsilon_{max} = 0.004$, green is for 0.01, black is for 0.03, blue is for 0.05 and magenta is for 0.1. The dotted lines are temperature of the respective step height.

We compare the fluxes of all three types of ramps by plotting the escaping mode, MO mode, flux for a ramp of height, $\epsilon_{max} = 0.004$. Figure 4.16 shows the flux as we vary the gradient of the ramp. The frequency is, $\hbar\omega = 0.018$ eV at which the flux is calculated.

- The difference between the there ramps is how they transform to the asymptotic regions. The exponential ramp transforms most abruptly at the top of the ramp, [2] ramp transforms smoothly and quickly and the sigmoid ramp transforms very slowly and smoothly to the asymptotic region.

- Ramps that slowly transform to the asymptotic region have a lower flux and ramps that make a sudden change to the asymptotic layer give a higher flux.

Studying the ramps we have found that the curvature at the turning point plays the most important role along with the ramp height.

Until now we have studied only infinitely long steps or ramps where we have only one horizon case. When the scatterer is a pulse we have two edges, unlike a step. We will study how a pulse affects the spectrum.
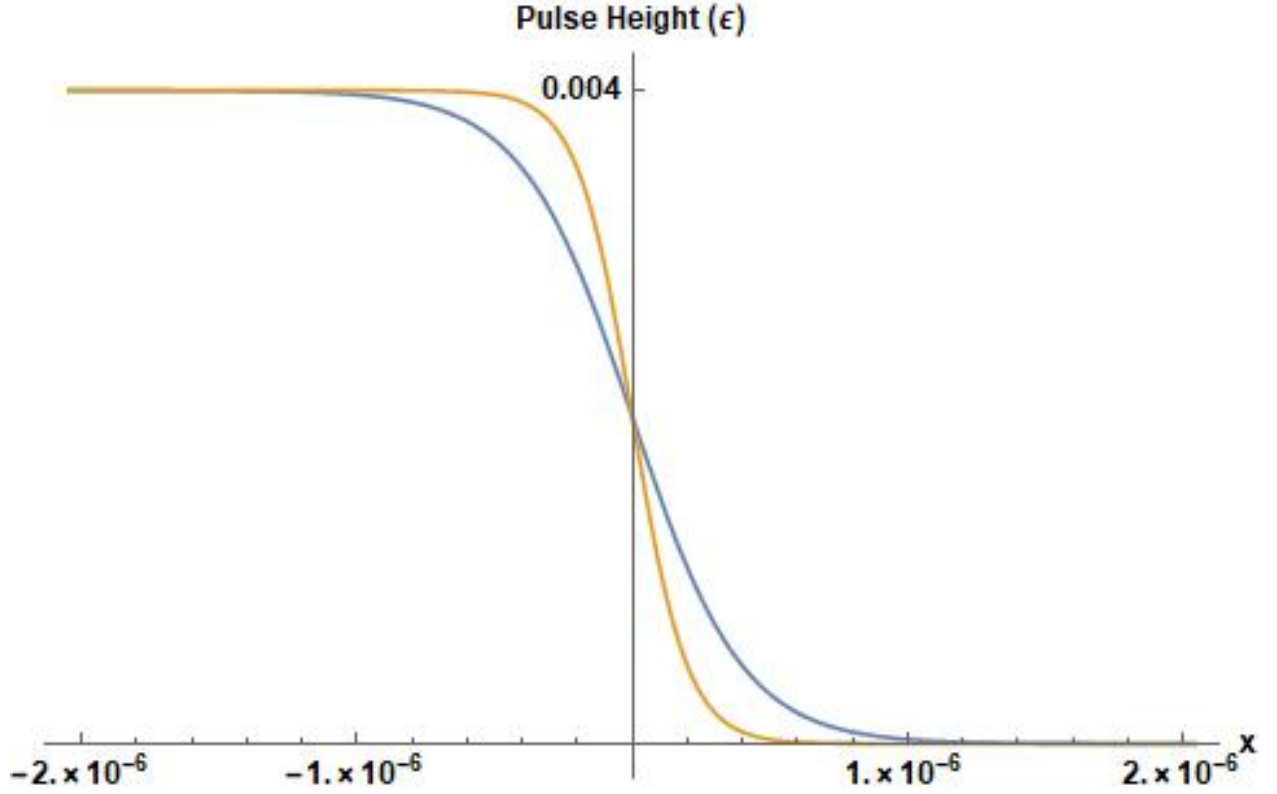
89

Figure 4.14: Plot of two sigmoid ramps. The blue curve has the gradient of $p = 5 \times 10^6$ and yellow curve has $p = 10^7$. Both the curves have the height of $\epsilon_{max} = 0.004$.

4.2.2 Top Hat Pulse

The simplest pulse we can study is the top hat pulse. In a top hat pulse we will have only three layers. The top hat pulse has an extra parameter, the pulse length, T_0. No numerical study has been previously done on scattering from a top hat pulse. The spatial width, L_0, of a pulse is calculated as

$$L_0 = V_g T_0. \tag{4.6}$$

V_g is the group velocity of the pulse and T_0 is the temporal width of the pulse. We plot the flux of a top-hat pulse of the same height as the step we analysed, $\epsilon = 4 \times 10^{-3}$, and temporal width of $T_0 = 2$ fs. The group velocity is the same as before of the step and the ramp, $v = 0.681588 \times c$. Figure 4.17 shows the flux for the top hat pulse.

- The asymptotic regions are identical in the case of a top hat pulse. The flux curves do not have a kink at the transition from scenario 3 to scenario 2.

- The escaping mode MO,black curve, and the optical UO mode, blue curve are more or less constant
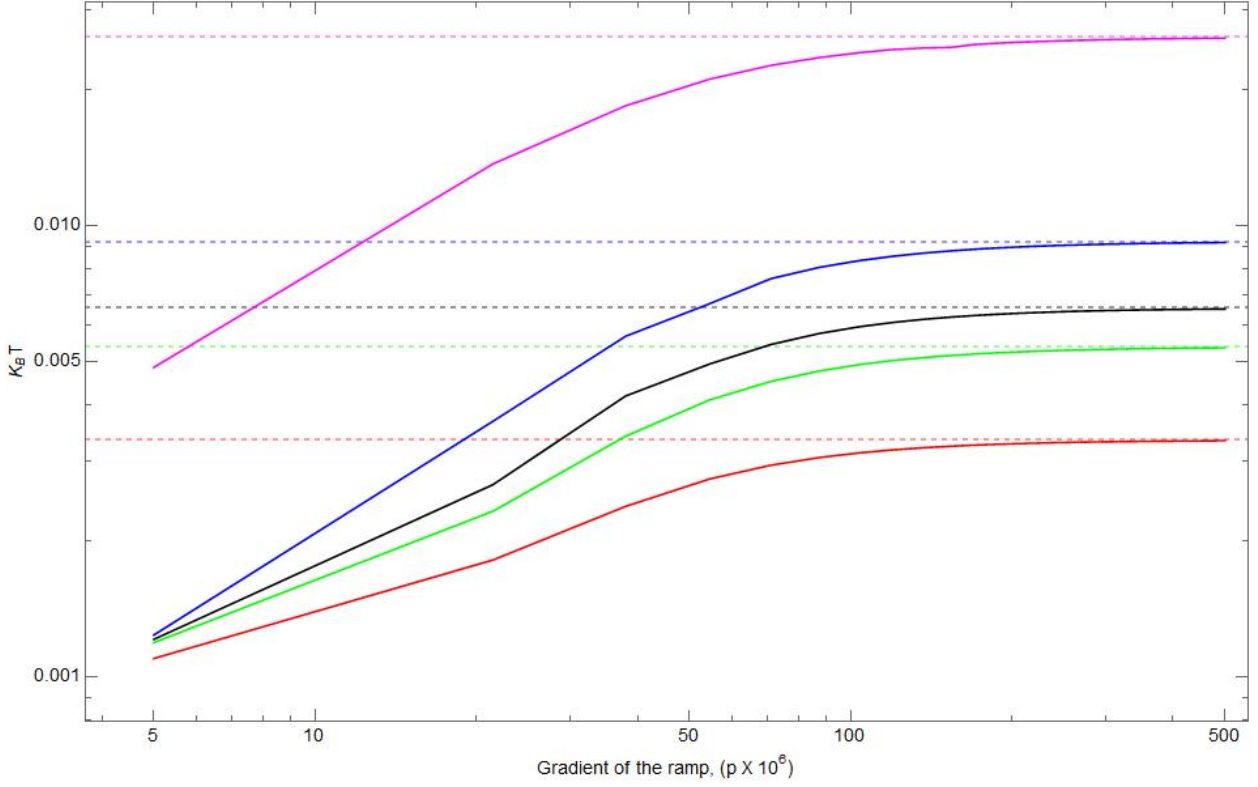
90

Figure 4.15: Five temperature curves for MO mode are plotted for different ramp heights. The red curve is for $\epsilon_{max} = 0.004$, green is for $\epsilon_{max} = 0.03$, black is for $\epsilon_{max} = 0.05$, blue is for $\epsilon_{max} = 0.1$ and pink is for $\epsilon_{max} = 0.5$.

throughout horizon window (scenario 2) .

- The modes that cease to exist in scenario 1, MO and UO mode, do dip as in the case of a step and the ramp.

The flux fluctuates with the top hat pulse length. We can see that in a plot of the flux with respect to pulse length's. Figure 4.18 shows the fluctuation in flux for the optical modes as we change the temporal pulse width from 0.2 fs to 10 fs for the frequency, $\hbar\omega = 0.018$ eV. At this frequency we are in scenario 2, as shown in Figure 3.3. We have 8 real solutions outside the pulse and 6 real inside the top hat pulse. MO and UO are complex modes inside the top hat pulse at this frequency.

- The mode fluxes fluctuate with their own unique frequency as a function of the temporal width.

- We see that the fluctuations of the MO and UO modes decay away for increase in T_0 but the fluctuations of O mode does not. MO and UO mode are complex inside the top hat pulse and as we increase the pulse length the tunneling effect of the complex modes decay away. The optical mode, O , exists in the top hat pulse and the phase it acquires as it travels inside the top hat layer causes the fluctuations.
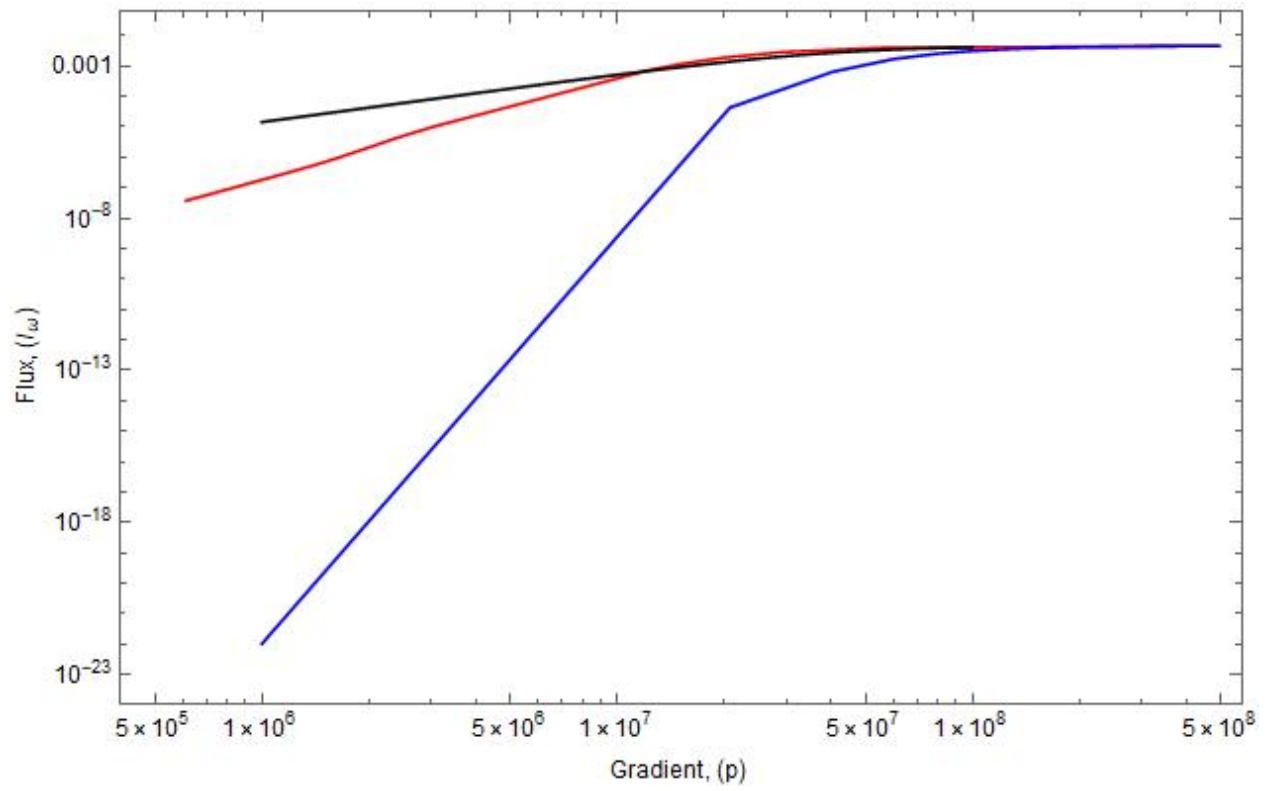
91

Figure 4.16: Flux of the escaping mode, MO for three different kinds of ramp of same height, $\epsilon = 0.004$. Blue is for the Sigmoid ramp, Red is for the *Sech* ramp and black is for the exponential ramp.
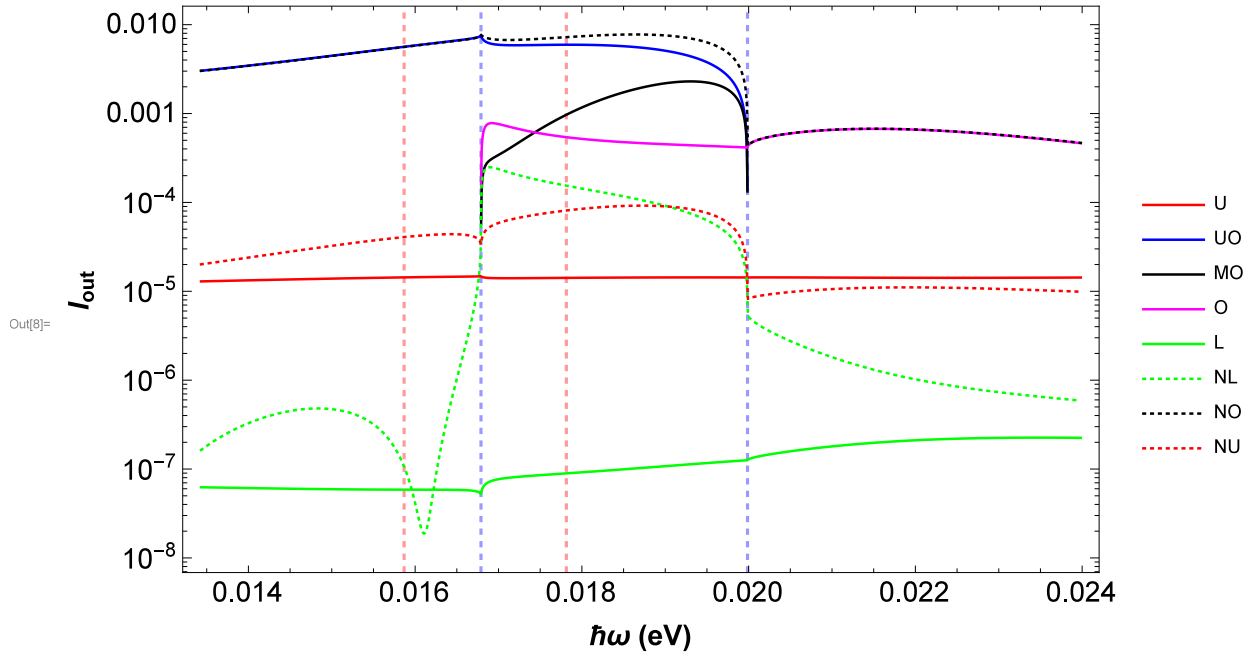
Figure 4.17: Flux spectrum for a top hat pulse of height $\epsilon = 4 \times 10^{-3}$ and pulse length of $T_0 = 2fs$. The vertical red dotted lines are the $\hbar\omega_{min}$ and $\hbar\omega_{max}$, i.e are the turning points of the optical branch of the medium. The blue dotted lines are $\hbar\omega'_{min}$ and $\hbar\omega'_{max}$ are the turning points of the optical branch in the top hat pulse. All the curves are labelled as, Red for Upper mode, Blue for Upper optical mode, Black for middle optical mode, Magenta for Lower optical mode, Green for lower mode, Green dashed line for negative mode, Black dashed line is for negative optical mode and red dashed line is for negative upper mode.
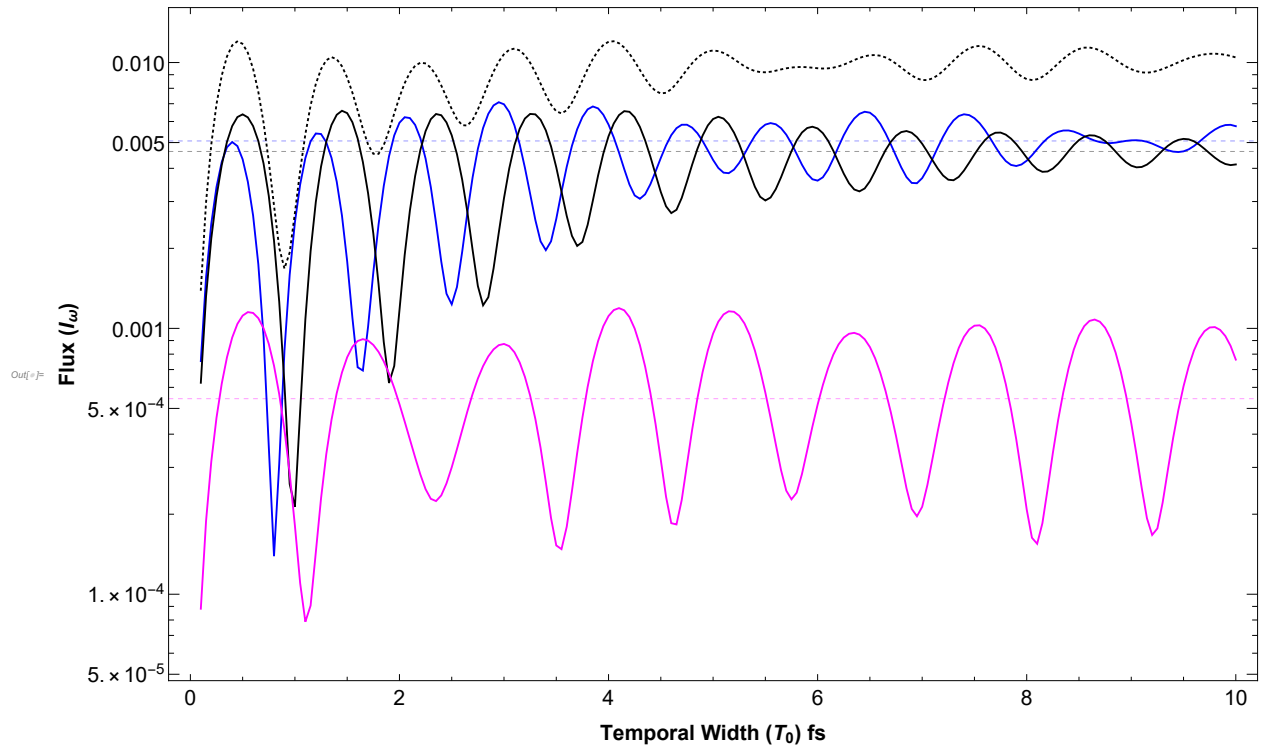
Figure 4.18: Flux for optical modes against the temporal width of the top hat pulse. Blue is for UO mode, Black is for MO mode, pink is for O mode and black dotted curve is for the NO mode. The dashed lines are the flux for a step of the same height as the top hat pulse. Calculated for a fixed frequency, $\hbar\omega = 0.018eV$ and pulse height $\epsilon = 0.004$.

- The fluctuations in the NO mode are correlated with all the three optical modes.

- The flux periodically fluctuates around the step's flux. The top hat pulse creates more flux than a step at certain temporal widths. This is where the fluxes for a certain frequency constructively interfere inside the pulse.

The flux's response to the change in temporal width is not easy to predict. We can trace the dependence of pulse width back to the transfer matrix

$$T_{topHat} = M_3^{-1} M_2 \phi_2 M_2^{-1} M_1 \tag{4.7}$$

$$= T_{stepL} \phi_2 T_{stepL}^{-1} \tag{4.8}$$

Here T_{stepL} is the transfer matrix of the left step as shown in figure 4.1. The phase matrix, ϕ_2 is defined as in equation (3.8). Every element of the transfer matrix is a linear combination of all the exponential in ϕ matrix,

$$T_{ij} = \sum_{h=0}^{h=8} (T_{stepL}^{-1})_{ih} (T_{stepL})_{hk} \exp^{(iK^h l)} . \tag{4.9}$$

Following the T-matrix algorithm (3.49) we can see that inverting the transfer matrix will result in a complicated dependence on the exponential terms. In a simple model we can see that the scattering matrix elements will have a geometric series of the exponential terms as shown in Appendix . We can see that every scattering matrix coefficient is very complex combination of exponential components and there does not seem to be a straightforward analytical way to know the effect of changing the pulse widths will have on the scattering coefficients.

We can plot a similar figure as 4.5 for the height of the top hat for the same frequency. The escaping mode's flux is plotted as we increase the height of the step in figure 4.19.

- The flux for optical modes fluctuate this is because the wavenumber inside the pulse changes changing the phase pick up and hence changing the scattering coefficients.

- The effect of the turning point, gray dashed line, is not very evident as the dispersion relation of the asymptotic layers do not change.

- MO mode is the only mode which do not fluctuate periodically or its fluctuation is quite dampened as we increase the pulse height.
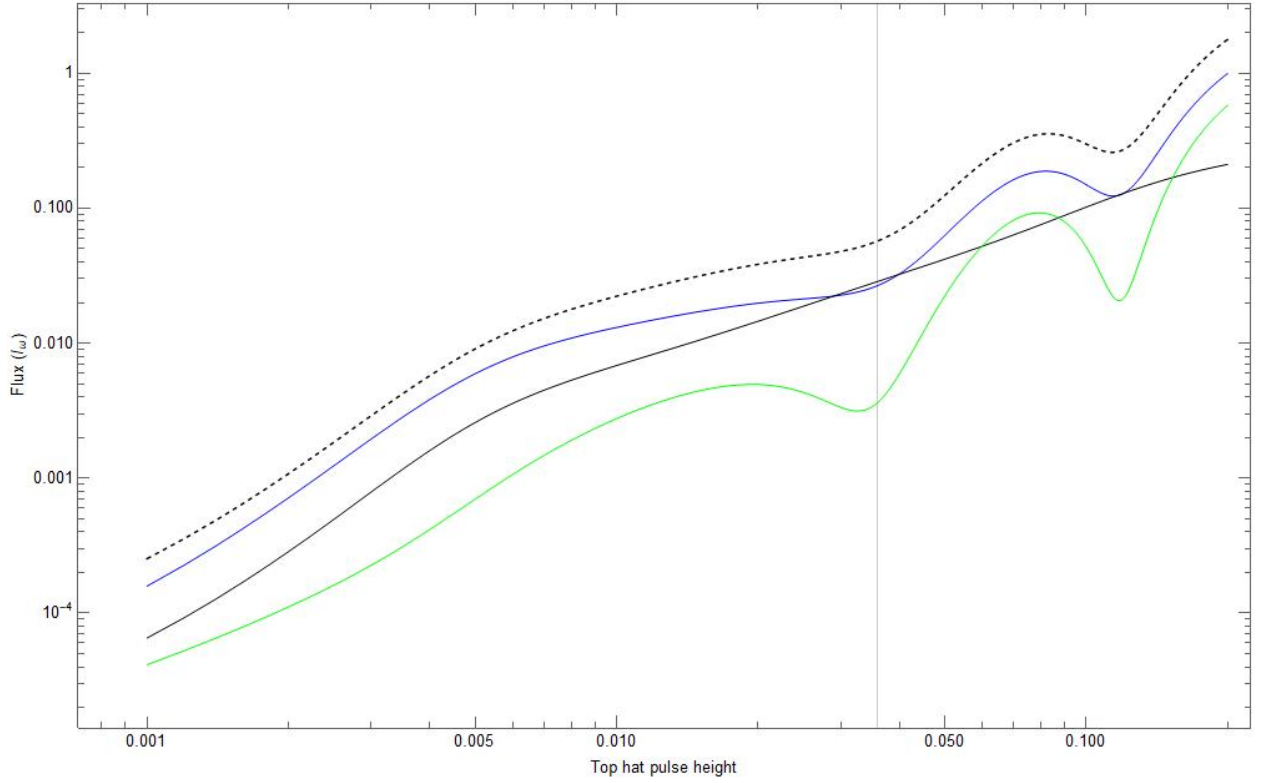
Figure 4.19: Log plot of the flux of the optical modes for top hat pulse, $T_0 = 3fs$. The black curve is for MO mode, blue curve is for UO mode, Green is for O mode and black dashed curve is for NO mode. The height of the pulse is on the x axis. The gray vertical line is height of the pule where we get complex modes inside the pulse. After the vertical line we have the horizon case.

4.2.3 $Sech^2$ Pulse

$Sech^2$ pulses are important to study as optical solitons have the same shape. In literature [39] it is believed that $Sech^2$ pulses with shortest and highest intensity will produce the most flux though no numerical study has been done in detail. We will plot the flux of various pulse sizes and intensity to find out what optimises the flux.

We plot the temperature of the escaping mode as we change the temporal width of a pulse for different height of the pulse. Figure 4.20 shows the plot.

- The shapes of all the curves are similar. They have a distinct feature of rising to a maximum temperature and then dropping to numerical zero.

- The temperature rises in the start because for a zero length pulse we will get zero flux so for the very short window at small pulse lengths the temperature rises initially.

- After reaching the peak the gradient of the pulse play a more important role and as we increase the temporal width the flux exponentially decreases as the gradient of the pulse decreases.
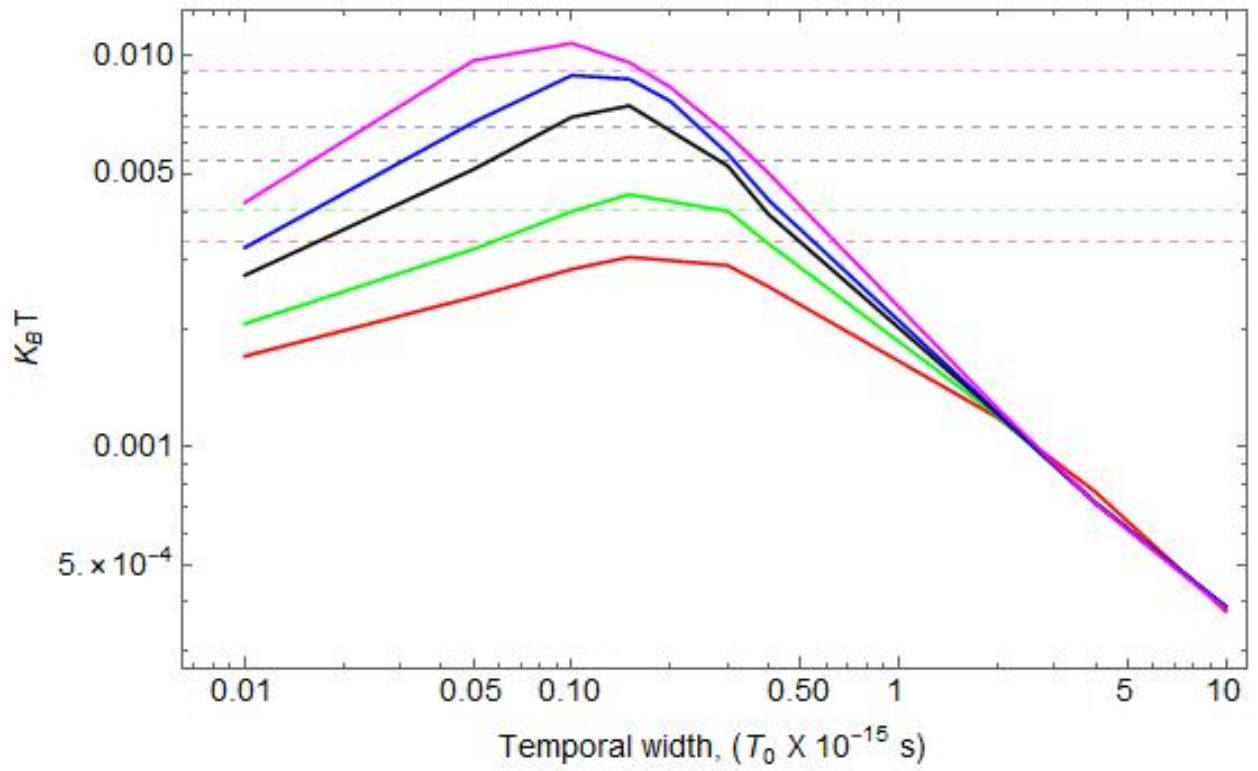
96

Figure 4.20: Log-log plot of temperature vs the temporal widths of the $Sech^2$ pulse. The red curve is for $\epsilon_{max} = 0.004$, green is for $\epsilon_{max} = 0.01$, black is for $\epsilon_{max} = 0.03$, blue is for $\epsilon_{max} = 0.05$ and pink is for $\epsilon_{max} = 0.1$.
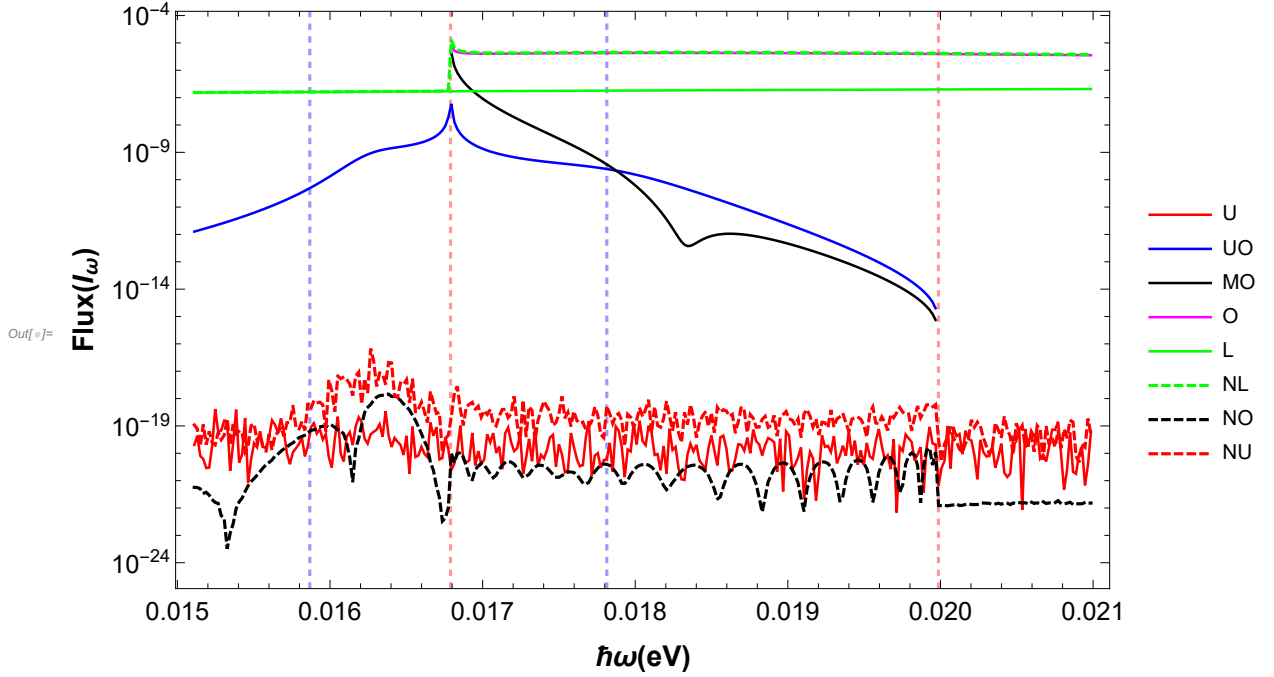
Figure 4.21: Flux spectrum(I_ω) vs $\hbar\omega$ for a $sech^2$ pulse of height $\epsilon = 4 \times 10^{-3}$ and pulse length of $T_p = 2fs$. Blue dashed lines ω'_{min} and ω'_{max}. Red Dashed lines are ω^{min} and ω_{max}. All the curves are labelled as, Red for Upper mode, Blue for Upper optical mode, Black for middle optical mode, Magenta for Lower optical mode, Green for lower mode, Green dashed line for negative mode, Black dashed line is for negative optical mode and red dashed line is for negative upper mode.

- The peak of the temperature changes for different heights of the pulse. Higher the pulse the more shifted is the peak towards lower pulse lengths,

- Most of the curves' peak exceed the temperature of the step of the same height. This is similar to the top hat pulse. The modes must constructively interfere inside the pulse to give a higher flux.

We plot the flux spectrum against frequency for $Sech^2$ pulses of two different temporal widths. Figure 4.21 shows the flux for $2fs$ pulse and figure 4.22 shows the flux for $4fs$ pulse. We see that the flux is very low and close to the numerical zero. The red curve in the figures just shows the numerical noise as the flux is so low for upper (U) and NU curve. The MO curve is also very low and hardly changes across the frequency.

These results show that it is very unlikely to get a measurable flux from a pulse with a temporal width greater than $2fs$. A soliton of a fixed temporal width of more than $2fs$ will produce very little flux. A higher-order soliton where the pulse goes through a pulse compression means that the pulse can become shorter than $2fs$ and higher order effects can make the pulse asymmetric [84]. The ultra short pulses and the steepness of the asymmetric pulse will increase the flux as seen in the above results.
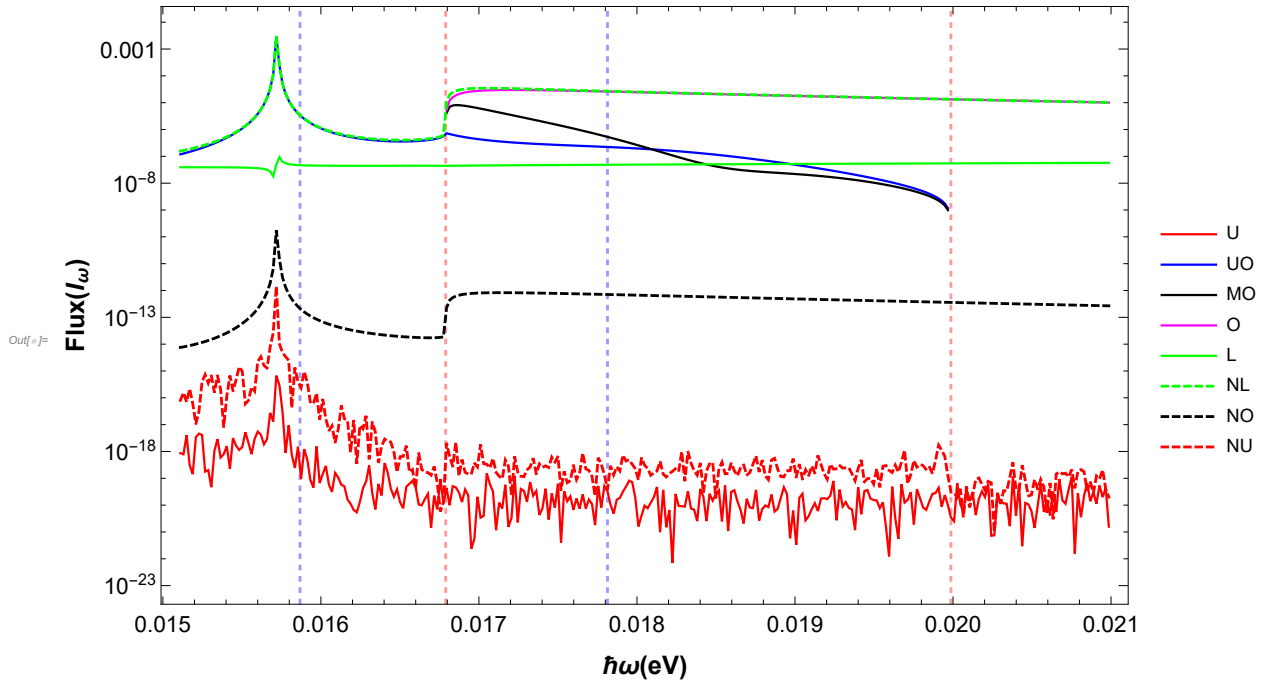
Figure 4.22: Flux spectrum(I_ω) vs $\hbar\omega$ for a $sech^2$ pulse of height $\epsilon = 4 \times 10^{-3}$ and pulse length of $T_p = 4fs$. Blue dashed lines ω'_{min} and ω'_{max}. Red Dashed lines are ω^{min} and ω_{max}. All the curves are labelled as, Red for Upper mode, Blue for Upper optical mode, Black for middle optical mode, Magenta for Lower optical mode, Green for lower mode, Green dashed line for negative mode, Black dashed line is for negative optical mode and red dashed line is for negative upper mode.

Conclusion

In this thesis we have shown a new concise formula connecting T-matrix to S-matrix and have generalised both the T and S-matrix algorithms to describe scattering from a moving scatterer. The numerical stability of S-matrix algorithm is demonstrated and we have successfully calculated a scattering matrix through the new Riccati matrix equation. We have demonstrated the fast convergence of the solutions through the Runge-Kutta method. We demonstrated the numerical stability of the S-matrix algorithm compared to the T-matrix algorithm, which we formulated in a compact way. We presented a novel differential equation for the scattering matrix. We analyzed its convergence and the stability of the solutions and show that they are well behaved. Increasing the number of steps, we can increase the desired precision level. An advantage of using the differential equation rather than directly the staircase approximation is that established efficient numerical methods with a high order of convergence can be used. We also presented the recursive S-Matrix formula in a compact formalism by using projector matrices. We also generalised the T-matrix and the S-matrix formulations to allow uneven number of right and left going modes.

We used these numerical methods to study the scattering from various profiles, steps, ramps and pulses. We have shown how the fluxes for all the modes vary as frequency changes. The effect of steepness and shape of the the profile on the flux is also studied. This in-depth study of profiles has not been done in this optical system where all eight branches of dispersion are included in the calculation. We study the effect of both analogue black hole and white hole horizon working together. The top hat pulse shows this effect alongside with the effect of the length of the pulse. The study of ramps isolates the effects of steepness and the shape of the ramp. We plot the brightness temperature of the flux of the escaping mode as we change the steepness for three different ramp shapes. We also see the full spectrum flux for a $Sech^2$ pulse and see that it falls off as we increase the temporal width of the pulse.

For future work, more numerical results can be generated for other mediums. We have calculated for bulk silica, one can model a silica fiber with a Sellmeier model and attain resonant frequencies and elasticity. This might give results more closely matched with the experiments as the experiments are done with a silica fiber [39]. Another thing one can do is to generate a look-up table with solutions for various frequencies so that the quadratic equations do not need to be solved to find the solutions and the calculation can be done much faster. The whole algorithm can be made even faster by using the star product for scattering matrix [85]. However, the star product is not generalised yet for dealing with scattering matrices with uneven number of right and left going modes. If we have a generalised formula for the star product then we can calculate the scattering matrix of a symmetric pulse by just calculating the scattering matrix of a ramp.

The insights from the results are good but there are still many interesting aspects which would require

more observations. Even for a top hat pulse we have seen some resonances peaks which are not explained completely. The brightness temperature plots versus the height of the ramps need to be explained further as to why the temperature drops as we keep on increasing the ramp height. Other asymmetric pulses can be modelled as well.

This thesis opens up doors on to numerically solving scattering problems in optics or acoustics and the application in analogue Hawking radiation shows the power of the methods developed. The results themselves are novel and have not been published elsewhere. This gives us the insight and places us in a better position to understand experimental results. It also helps in designing better experiments.

Bibliography

[1] A.Einstein, "The foundation of the general theory of relativity," *Annalen der Physik*, vol. 49, 1916.

[2] K. Schwarzschild, "On the gravitational field of a point mass in einstein's theory," *Proceedings of the Prussian Academy of Sciences*, vol. 424, 1916.

[3] J. R. Oppenheimer and H. Snyder, "On continued gravitational contraction," *Physical Review*, vol. 455, pp. 56–61, 1939.

[4] N. D. Birrell and P. C. W. Davies, *Quantum fields in curved space*, vol. 7. Cambridge university press, 1984.

[5] P. Painlevé, "La gravitation dans la mécanique de newton et dans la mécanique d'einstein," pp. 873–887, 1921.

[6] A. Gullstrand, *"allgemeine lösung des statischen einkörperproblems in der einsteinschen gravitationstheorie,"* 1922.

[7] *A. J. Hamilton and J. P. Lisle, "The river model of black holes,"* American Journal of Physics, *pp. 519–532, 2008.*

[8] *S. W. Hawking, "Black hole explosions?,"* Nature, *vol. 248, no. 5443, pp. 30–31, 1974.*

[9] *T. Jacobson, "Black-hole evaporation and ultrashort distances,"* Phys. Rev. D, *vol. 44, pp. 1731–1739, Sep 1991.*

[10] *R. Brout, S. Massar, R. Parentani, and P. Spindel, "Hawking radiation without trans-planckian frequencies,"* Phys. Rev. D, *vol. 52, pp. 4559–4568, Oct 1995.*

[11] *W. G. Unruh, "Experimental black-hole evaporation?,"* Phys. Rev. Lett., *vol. 46, pp. 1351–1353, May 1981.*

[12] W. G. Unruh, "Sonic analogue of black holes and the effects of high frequencies on black hole evaporation," Phys. Rev. D, vol. 51, pp. 2827–2838, Mar 1995.

[13] G. E. Volovik, "Simulation of a panlevé-gullstrand black hole in a thin 3he-a film," vol. 69, no. 9, pp. 705–713, 1999.

[14] T. A. Jacobson and G. E. Volovik, "Event horizons and ergoregions in ^{3}He," Phys. Rev. D, vol. 58, p. 064021, Aug 1998.

[15] L. J. Garay, J. R. Anglin, J. I. Cirac, and P. Zoller, "Sonic analog of gravitational black holes in bose-einstein condensates," Phys. Rev. Lett., vol. 85, pp. 4643–4647, Nov 2000.

[16] L. J. Garay, J. R. Anglin, J. I. Cirac, and P. Zoller, "Sonic black holes in dilute bose-einstein condensates," Phys. Rev. A, vol. 63, p. 023611, Jan 2001.

[17] C. Barceló, S. Liberati, and M. Visser, "Towards the observation of hawking radiation in bose-einstein condensates," International Journal of Modern Physics A, vol. 18, no. 21, pp. 3735–3745, 2003.

[18] R. Schützhold, "Detection scheme for acoustic quantum radiation in bose-einstein condensates," Phys. Rev. Lett., vol. 97, p. 190405, Nov 2006.

[19] R. Balbinot, A. Fabbri, S. Fagnocchi, A. Recati, and I. Carusotto, "Nonlocal density correlations as a signature of hawking radiation from acoustic black holes," Physical Review A, vol. 78, no. 2, 2008.

[20] I. Carusotto, S. Fagnocchi, A. Recati, R. Balbinot, and A. Fabbri, "Numerical observation of hawking radiation from acoustic black holes in atomic bose–einstein condensates," New Journal of Physics, vol. 10, p. 103001, oct 2008.

[21] B. Horstmann, B. Reznik, S. Fagnocchi, and J. I. Cirac, "Hawking radiation from an acoustic black hole on an ion ring," Physical Review Letters, vol. 104, no. 25, 2010.

[22] J. Steinhauer, "Observation of self-amplifying hawking radiation in an analogue black-hole laser," Nature Physics, vol. 10, no. 11, pp. 864–869, 2014.

[23] M. Tettamanti, S. L. Cacciatori, A. Parola, and I. Carusotto, "Numerical study of a recent black-hole lasing experiment," vol. 114, no. 6, p. 60011, 2016.

[24] J. Steinhauer, "Observation of quantum hawking radiation and its entanglement in an analogue black hole," Nature Physics, vol. 12, pp. 959 EP –, Aug 2016. Article.

[25] U. Leonhardt, "Questioning the recent observation of quantum hawking radiation," Annalen der Physik, vol. 530, no. 5, p. 1700114, 2018.

[26] R. Schützhold and W. G. Unruh, "Gravity wave analogues of black holes," Phys. Rev. D, vol. 66, p. 044019, Aug 2002.

[27] G. Rousseaux, C. Mathis, P. Maïssa, T. G. Philbin, and U. Leonhardt, "Observation of negative-frequency waves in a water tank: a classical analogue to the hawking effect?," New Journal of Physics, vol. 10, p. 053015, may 2008.

[28] S. Weinfurtner, E. W. Tedford, M. C. J. Penrice, W. G. Unruh, and G. A. Lawrence, "Measurement of stimulated hawking emission in an analogue system," Phys. Rev. Lett., vol. 106, p. 021302, Jan 2011.

[29] L.-P. Euvé, F. Michel, R. Parentani, T. G. Philbin, and G. Rousseaux, "Observation of noise correlated by the hawking effect in a water tank," Phys. Rev. Lett., vol. 117, p. 121301, Sep 2016.

[30] U. Leonhardt and P. Piwnicki, "Optics of nonuniformly moving media," Phys. Rev. A, vol. 60, pp. 4301–4312, Dec 1999.

[31] U. Leonhardt, "Space-time geometry of quantum dielectrics," Phys. Rev. A, vol. 62, p. 012111, Jun 2000.

[32] U. Leonhardt and P. Piwnicki, "Relativistic effects of light in moving media with extremely low group velocity," Phys. Rev. Lett., vol. 84, pp. 822–825, Jan 2000.

[33] M. Visser, "Comment on "relativistic effects of light in moving media with extremely low group velocity"," Physical Review Letters, vol. 85, no. 24, pp. 5252–5252, 2000.

[34] U. Leonhardt and P. Piwnicki, "Leonhardt and piwnicki reply:," Physical Review Letters, vol. 85, no. 24, pp. 5253–5253, 2000.

[35] "Lettre de m. fresnel 'a m. arago, sur l'influence du mouvement terrestre dansquelques ph enom'enes d'opteque," Annales de Chimie et de Physique, vol. 9, pp. 57–66, 1818.

[36] "Sur les hypothèses relatives à l'éther lumineux et sur une expérience qui paraît démontrer que le mouvement des corps change la vitesse avec laquelle la lumière se propage dans leur intérieur [on the hypotheses relating to the luminous æther, and an experiment which appears to demonstrate that the motion of bodies alters the velocity with which light propagates itself in their interior]," Comptes Rendus de l'Acad emie des Sciences de Paris, vol. XXXIII, p. 349–355, 1851.

[37] M. Novello, S. P. Bergliaffa, J. Salim, V. A. D. Lorenci, and R. Klippert, "Analogue black holes in flowing dielectrics," Classical and Quantum Gravity, vol. 20, pp. 859–871, feb 2003.

[38] V. A. De Lorenci, R. Klippert, and Y. N. Obukhov, "Optical black holes in moving dielectrics," Physical Review D, vol. 68, no. 6, 2003.

[39] T. G. Philbin, C. Kuklewicz, S. Robertson, S. Hill, F. König, and U. Leonhardt, "Fiber-optical analog of the event horizon," Science, vol. 319, no. 5868, pp. 1367–1370, 2008.

[40] J. Macher and R. Parentani, "Black/white hole radiation from dispersive theories," Physical Review D, vol. 79, no. 12, 2009.

[41] F. Belgiorno, S. L. Cacciatori, G. Ortenzi, V. G. Sala, and D. Faccio, "Quantum radiation from superluminal refractive-index perturbations," Physical Review Letters, vol. 104, no. 14, 2010.

[42] F. Belgiorno, S. L. Cacciatori, M. Clerici, V. Gorini, G. Ortenzi, L. Rizzi, E. Rubino, V. G. Sala, and D. Faccio, "Hawking radiation from ultrashort laser pulse filaments," Phys. Rev. Lett., vol. 105, p. 203901, Nov 2010.

[43] E. Rubino, F. Belgiorno, S. L. Cacciatori, M. Clerici, V. Gorini, G. Ortenzi, L. Rizzi, V. G. Sala, M. Kolesik, and D. Faccio, "Experimental evidence of analogue hawking radiation from ultrashort laser pulse filaments," New Journal of Physics, vol. 13, p. 085005, aug 2011.

[44] R. Schützhold and W. G. Unruh, "Comment on "hawking radiation from ultrashort laser pulse filaments"," Phys. Rev. Lett., vol. 107, p. 149401, Sep 2011.

[45] W. G. Unruh and R. Schützhold, "Hawking radiation from "phase horizons" in laser filaments?," Phys. Rev. D, vol. 86, p. 064006, Sep 2012.

[46] A. Choudhary and F. König, "Efficient frequency shifting of dispersive waves at solitons," Opt. Express, vol. 20, pp. 5538–5546, Feb 2012.

[47] E. Rubino, J. McLenaghan, S. C. Kehr, F. Belgiorno, D. Townsend, S. Rohr, C. E. Kuklewicz, U. Leonhardt, F. König, and D. Faccio, "Negative-frequency resonant radiation," Phys. Rev. Lett., vol. 108, p. 253901, Jun 2012.

[48] N. Akhmediev and M. Karlsson, "Cherenkov radiation emitted by solitons in optical fibers," Phys. Rev. A, vol. 51, pp. 2602–2607, Mar 1995.

[49] J. McLenaghan and F. Koenig, "Few-cycle fiber pulse compression and evolution of negative resonant radiation," NEW JOURNAL OF PHYSICS, vol. 16, JUN 10 2014.

[50] J. Drori, Y. Rosenberg, D. Bermudez, Y. Silberberg, and U. Leonhardt, "Observation of stimulated hawking radiation in an optical analogue," Phys. Rev. Lett., vol. 122, p. 010404, Jan 2019.

[51] J. J. Hopfield, "Theory of the contribution of excitons to the complex dielectric constant of crystals," Phys. Rev., vol. 112, pp. 1555–1567, Dec 1958.

[52] S. Finazzi and I. Carusotto, "Quantum vacuum emission in a nonlinear optical medium illuminated by a strong laser pulse," Phys. Rev. A, vol. 87, p. 023803, Feb 2013.

[53] J. A. Wheeler, "On the mathematical description of light nuclei by the method of resonating group structure," Phys. Rev., vol. 52, pp. 1107–1122, Dec 1937.

[54] W. C. Chew, Integral Equations. IEEE, 1995.

[55] N. P. K. Cotter, T. W. Preist, and J. R. Sambles, "Scattering-matrix approach to multilayer diffraction," J. Opt. Soc. Am. A, vol. 12, pp. 1097–1103, May 1995.

[56] L. D. Landau and E. M. Lifshitz, vol. 3. Oxford : Butterworth-Heinemann, 1977.

[57] U. Leonhardt, Essential Quantum Optics: From Quantum Measurements to Black Holes. Cambridge University Press, 2010.

[58] U. Leonhardt, Essential Quantum Optics: From Quantum Measurements to Black Holes. Cambridge University Press, 2010.

[59] I. H. Malitson, "Interspecimen comparison of the refractive index of fused silica∗,†," J. Opt. Soc. Am., vol. 55, pp. 1205–1209, Oct 1965.

[60] C. Tan, "Determination of refractive index of silica glass for infrared wavelengths by ir spectroscopy," Journal of Non-Crystalline Solids, vol. 223, no. 1, pp. 158 – 163, 1998.

[61] E. Becker, "L. m. brekhovskikh, waves in layered media (applied mathematics and mechanics, vol. 6). translated from the russian. new york/london 1960. academic press," ZAMM - Journal of Applied Mathematics and Mechanics / Zeitschrift für Angewandte Mathematik und Mechanik, vol. 42, no. 3, pp. 129–129, 1962.

[62] P. C. Waterman, "Matrix formulation of electromagnetic scattering," Proceedings of the IEEE, vol. 53, pp. 805–812, Aug 1965.

[63] "T-matrix theory of electromagnetic scattering by partciles and its applications: a comprehensive reference database," *Journal of Quantitative Spectroscopy and Radiative Transfer*, *vol. 88, no. 1, pp. 357 – 406, 2004. Photopolarimetry in remote sensing.*

[64] *S. Wolfram,* The Mathematica Book. *Wolfram Media, Incorporated, 5 ed., 2003.*

[65] *P. Wellin,* Numerics, *p. 251–308. Cambridge University Press, 2013.*

[66] *P. Lancaster,* Theory of Matrices. *Academic Press, 1969.*

[67] *R. B. Josef Stoer, vol. 12. Springer-Verlag New York, 2002.*

[68] *D. Y. K. Ko and J. C. Inkson, "Matrix method for tunneling in heterostructures: Resonant tunneling in multilayer systems,"* Phys. Rev. B, *vol. 38, pp. 9945–9951, Nov 1988.*

[69] *D. Y. K. Ko and J. R. Sambles, "Scattering matrix method for propagation of radiation in stratified media: attenuated total reflection studies of liquid crystals,"* J. Opt. Soc. Am. A, *vol. 5, pp. 1863–1866, Nov 1988.*

[70] *D. M. Pai and K. A. Awada, "Analysis of dielectric gratings of arbitrary profiles and thicknesses,"* J. Opt. Soc. Am. A, *vol. 8, pp. 755–762, May 1991.*

[71] *L. Li, "Multilayer modal method for diffraction gratings of arbitrary profile, depth, and permittivity: addendum,"* J. Opt. Soc. Am. A, *vol. 11, pp. 1685–1685, May 1994.*

[72] *N. Chateau and J.-P. Hugonin, "Algorithm for the rigorous coupled-wave analysis of grating diffraction,"* J. Opt. Soc. Am. A, *vol. 11, pp. 1321–1331, Apr 1994.*

[73] *L. Li, "Formulation and comparison of two recursive matrix algorithms for modeling layered diffraction gratings,"* J. Opt. Soc. Am. A, *vol. 13, pp. 1024–1035, May 1996.*

[74] *A. Choudhary and F. König, "Efficient frequency shifting of dispersive waves at solitons,"* Opt. Express, *vol. 20, pp. 5538–5546, Feb 2012.*

[75] *C. Runge, "Ueber die numerische auflösung von differentialgleichungen,"* Math. Ann., *vol. 46, pp. 167–178, June 1895.*

[76] *H. A. Luther, "An explicit sixth-order runge-kutta formula,"* Math. Comp., *vol. 22, pp. 434–436, 1968.*

[77] *S. Corley and T. Jacobson, "Hawking spectrum and high frequency dispersion,"* Phys. Rev. D, *vol. 54, pp. 1568–1586, Jul 1996.*

[78] J. Macher and R. Parentani, "Black-hole radiation in bose-einstein condensates," Phys. Rev. A, *vol. 80, p. 043601, Oct 2009.*

[79] M. Jacquet and F. König, "Quantum vacuum emission from a refractive-index front," Phys. Rev. A, *vol. 92, p. 023851, Aug 2015.*

[80] D. Bermudez and U. Leonhardt, "Hawking spectrum for a fiber-optical analog of the event horizon," Phys. Rev. A, *vol. 93, p. 053820, May 2016.*

[81] S. Robertson and U. Leonhardt, "Integral method for the calculation of hawking radiation in dispersive media. i. symmetric asymptotics," Phys. Rev. E, *vol. 90, p. 053302, Nov 2014.*

[82] S. Robertson, "Integral method for the calculation of hawking radiation in dispersive media. ii. asymmetric asymptotics," Phys. Rev. E, *vol. 90, p. 053303, Nov 2014.*

[83] M. Jacquet, Negative Frequency at the Horizon: Theoretical Study and Experimental Realisation of Analogue Gravity Physics in Dispersive Optical Media. *Springer Theses, Springer International Publishing, 2018.*

[84] G. P. Agrawal, "Chapter 6 - optical pulse compression," in Nonlinear Fiber Optics (Second Edition) (G. P. Agrawal, ed.), Optics and Photonics, pp. 201 – 237, Boston: Academic Press, second edition ed., 1995.

[85] R. Rumpf, "Improved formulation of scattering matrices for semi-analytical methods that is consistent with convention," Progress In Electromagnetics Research B, *vol. 35, pp. 241–261, 08 2011.*